FINITE NUMERICAL MODELLING OF STRESS DEFLECTIONS AROUND SALT DIAPIRS IN THE GULF OF MEXICO

Cowan R. Nokes

University of Adelaide, 2011

Honours Thesis

THE UNIVERSITY OF ADELAIDE
AUSTRALIA

TRaX
Centre for Tectonics Resources and Exploration

S3 Stress
Structure
Seismic

ASP
Australian School of Petroleum

Abstract

This research is focused on the Northern Gulf of Mexico Mississippi Fan Delta. Deltas have a maximum horizontal stress margin parallel (extensional stress regime) at the delta top and a margin normal maximum horizontal stress (compressional stress regime) at the delta toe (King et al., 2010). The area of the delta with intrusive salt diapirs has significantly deflected maximum horizontal stresses around the salt diapirs. This is due to the contrasting geomechanical rock properties between the salt and the deltaic sediments (Zhang, 1994). A 3D seismic survey of the area with vertical salt diapirs was provided by Western Geoco. The seismic data was interpreted for the top salt-sediment contact and diapir related deformation of the sedimentary overburden. The interpretation identified six salt diapirs: four piercing by active diapirism and two piercing by reactive diapirism. 2D finite numerical models were built from representative sections of each salt diapir to predict the principal stress deflections within the sedimentary overburden adjacent the salt. The models of the reactive diapirs deflected the maximum principal stress parallel to the salt-sediment contact of the salt diapirs. The models of the active diapirs deflected the maximum principal stress normal to the salt-sediment contact of the salt diapirs. The stress orientations allowed for borehole stability diagrams to be produced for the stress orientation above the diapir crests, over the diapir flank and over the base salt for each diapiric style.

Contents

1. Introduction
2. Background
3. Seismic Interpretation of Salt Diapirs in The Gulf of Mexico Method
4. Seismic Interpretation of Salt Diapirs in The Gulf of Mexico Results
5. Finite Numerical Modelling of Salt Diapirs Method
6. Finite Numerical Modelling of Salt Diapirs Results
7. Discussion
8. Implications
9. Acknowledgements
10. References
11. Table Captions
12. Figure Captions
13. Tables
14. Figures

1.0 Introduction

The three principal stresses (σ_1, σ_2 and σ_3) have significant implications on borehole stability yet there is little academic understanding at present of the variability of the stress orientation around salt diapirs. Wells drilled in unstable directions can blow out costing hundreds of millions of dollars in down time, lost expenditure as well as associated damages. Previous studies have demonstrated that the orientations and magnitudes of present-day stresses are critical to borehole stability, water flooding, fracture stimulation and fault reactivation (Heffer and Lean, 1993; Barton et al., 1998; Nelson et al., 2005; Tingay et al., 2009; King et al., 2010a). Boreholes are most stable when drilled in a direction that subjects the well to the least stress anisotropy (Heffer and Lean, 1993). This project will attempt to construct 2D models of the stress orientations around the salt diapirs in the Gulf of Mexico. The salt diapirs used in the modelling are interpreted from the Ship Shoal 3D seismic data cube provided by Western Geoco. These models will reinforce the concept that the maximum horizontal stress is rotated by the presence of a salt diapir. The research will predict the stress orientations around salt diapers in the Gulf of Mexico to determine the most stable drilling direction adjacent to salt diapirs.

2.0 Background

2.1 The Gulf of Mexico Geological Setting

The Gulf of Mexico is located offshore from the southern United States of America, to the east of Mexico and west of Cuba (Figure 2.1a). Water depths range from several metres deep around the coasts to over 2000 m in the central parts of the Gulf. The stratigraphy of the Gulf of Mexico is dominated by several thick Upper Jurassic to Pleistocene delta systems that overlay the Louann Salt (Peel et al., 1995; Trudgill et al., 1999; Figure 2.2b). The oil and gas have been thermally generated from Paleogene and Mesozoic source beds. Some of these hydrocarbons have migrated laterally and vertically into reservoirs and then into traps created by the Louann Salt fed diapirs (Figure 2.2; Morley et al., 2010).

2.2 Mechanics of Salt Movement

Salt has unique mechanical properties, under geologic time and conditions, it deforms viscoelastically as a fluid with negligible yield strength (Hudec and Jackson, 2007). At very high strain rates salt fractures (Hudec and Jackson, 2007). Dry salt deforms by dislocation creep, damp salt by weak diffusion creep (Hudec and Jackson, 2007). Jackson and Talbot (1986) described four mechanisms driving salt movement in an environment without far field tectonic forces: 1. Salt is incompressible and therefore when buried at depth below overburden of a greater density, salt becomes buoyant and gravitationally unstable (Figure 2.3a). 2. Differential loading of salt forces flows in response to the head gradient depending on the weight of the overburden and body forces within the salt (Figure 2.3b). 3. Gravitational displacement occurs where the flanks of a salt body move under its own weight via extension and shortening (Figure 2.3c). 4. Thermal loading is the volume change due to heat conduction and its associated change in temperature (Figure 2.3d). Resistance to salt movement comes from the strength of overlying sediment, dissolution and buoyancy drag (Jackson and Talbot, 1986).

2.3 Regional Tectonic Influence

Salt typically forms the mechanically weakest rock unit in a sedimentary sequence, and will therefore, often behave as a detachment (Trudgill et al., 1999). In the Gulf of Mexico the Louann Salt forms the regional detachment beneath the deltaic sediments. The system of induced extension and compression, produced by gravitational stresses of the delta setting, detach at the Louann Salt; all up-dip normal faults and down-dip thrust faults slide out at or in this level (Worrall and Snelson, 1989; Wu et al., 1990; Rowan, 1997).

Extensional salt tectonics in the Gulf of Mexico are confined to the delta top. In the absence of precursor diapirs the main control on extensional structural style is salt thickness. Thin salt layers are dominated by normal growth faults and low-amplitude salt structures such as salt rollers (Figure 2.4a). Thicker salt layers will form reactive diapirs and with continued extension, subsequent diapir fall (Hudec and Jackson, 2007). Reactive diapirs can progress completely from the reactive and active stages to become passive diapirs, which can remain at the surface as long as there is salt to feed them (Figure 2.5).

Shortening, located at the delta toe, thickens and therefore strengthens the overburden above salt, which retards the formation of new diapirs. In the absence of pre-existing salt structures, salt functions mainly as a detachment for large scale thrust faults, box fold anticlines and salt cored anticlines (Figure 2.4b; Hudec and Jackson, 2007). Pre-existing diapirs are preferentially reactivated during shortening creating plug-fed extrusions, through which salt can be displaced up and out, forming allochthonous salt sheets (Hudec and Jackson, 2007).

2.4 Salt Diapir Styles

A reactive diapir does not rise by forceful intrusion. Reactive salt diapirs fill the space created by the divergence of overburden fault blocks during extensional faulting (Figure 2.5b; Jackson, 1994). Regional extension is expected in delta tops like the survey area. Smaller, younger fault blocks float higher than larger, older fault blocks (Vendeville and Jackson, 1992a). The fluid pressures are below those needed for forceful intrusion.

An active diapir pierces by lifting and shoving aside its sedimentary roof (Figure 2.5c; Jackson et al., 1994). The principal driving force for active diapirism is the pressure exerted by the salt body on its surroundings (Schultz-Ela et al., 1993). In extensional settings, the force which stimulates extension above the diapir is generated by either a density contrast, between the salt and its overburden, or by differential pressure loading. During shortening, the driving force is generated by far field regional compressive stresses (Vendeville and Jackson, 1992a). The more the pressure of the salt exceeds that of the overburden, the more intense the extensional thinning of the overburden and transition from reactive diapirism to active diapirism will be. It may be difficult to distinguish between reactive and active diapirism as the two mechanisms can interact (Schultz-Ela et al., 1993).

Passive diapirs are diapirs that have emerged above the sea floor and remain there, continuing to grow by down-building with sediments accumulating on and around them (Figure 2.5d). The shape is determined by the relationship between the rates of salt extrusion, sedimentation and salt dissolution (Vendeville and Jackson, 1992a). Passive diapirs can evolve into allochthonous salt sheets, where mobilized salt overlays younger stratigraphic units (Hudec and Jackson, 2007; Figure 2.5e). This usually occurs during slow sedimentation rates (Hudec and Jackson, 2007). The sheet advance is determined by the rate the salt is extruded balanced by the rate of dissolution (Hudec and Jackson, 2007). Dissolution is prevented by a combination of a sedimentary veneer; an insoluble residual crust of gypsum; an overlaying layer of salt saturated brine, and; a low permeability roof (Jackson and Schulz, 1994).

Allochthonous salt sheets can advance by three mechanisms: 1. Extrusively, where the sheet spreads from a passive feeder faster than sedimentation, erosion and dissolution can contain it; 2. Open toed, where the sheet is partially buried by a roof that has been broken up by flow forces friction; 3. A thrust advancing allochthons, where the sheet and its continuous roof advance along a thrust fault. This advance mechanism can be efficient, leaving behind a salt weld, or inefficient, leaving behind discontinuous salt structures (Hudec and Jackson, 2007).

Salt cored anticlines are produced during shortening where the overburden has been thickened to a point where it is too competent to buckle. The overburden then folds and fills with salt from the flanks (Hudec and Jackson, 2007).

2.5 The Stress Regime around Salt Diapirs

In Northern Gulf of Mexico Mississippi-Fan deltaic settings, the gravity driven collapse of the shelf creates an extensional stress regime at the delta top and a compressional stress regime in the delta toe (Figure 2.6; Rowan, 1997). The extension regime at the delta top consists of large-scale normal growth faults reflecting a margin parallel maximum horizontal stress (σ_{Hmax}) orientation (REF). Compression at the delta toe produces large-scale thrust faults structures reflect a margin normal σ_{Hmax} orientation (Trudgill et al., 1999; Figure 2.6).

The orientation of σ_{Hmax} is measured in the field by borehole breakouts. Borehole breakouts form during drilling when the “maximum circumferential stress at the borehole wall exceeds the compressive rock strength, resulting in compressive failure and spalling of the borehole wall" (Bell, 1996). In vertical wells the circumferential stress is a function of the magnitude and the anisotropy between the σ_{Hmax} and the minimum horizontal stress (σ_{Hmin}). In vertical wells the maximum circumferential stress is perpendicular to the orientation of σ_{Hmax}; therefore, borehole breakouts will develop perpendicular to the orientation of σ_{Hmax} (Figure 2.7; Bell and Gough, 1979; Kirsch, 1898). Drilling-induced tensile fractures form due to tensile failure at the borehole wall when the minimum circumferential stress exceeds the tensile strength of the borehole wall (Aadnoy and Bell, 1998). Drilling-induced tensile fractures form parallel to the σ_{Hmax} orientation in vertical wells (Figure 2.7; Bell, 1996a; Brudy and Zoback, 1999).

In the delta top of the Gulf of Mexico, the σ_{Hmax} orientations are margin-parallel until the region offshore deformed by intrusive salt diapirs (Figure 2.8). Here, significant deflections from the expected margin-parallel orientation were observed near the seafloor surface adjacent to salt diapirs (Figure 2.8; King et al., in press; Yassir and Zerwer, 1997). Recent studies looking at 3D seismic data and geomechanical modelling have shown that the maximum horizontal stress is deflected by the salt-sediment contact of the salt diapirs at depth, as well as at the surface (King et al., in press).

Third-order stress field deflections in sedimentary basins are generated by local effects; such as the lateral density contrast of neighbouring rock units (Bell, 1996b). Therefore, the stress deflections observed around salt diapirs are as a result of the contrast in geomechanical rock properties between the salt and adjacent deltaic sediments (Zhang, 1994). Principal stresses intersect free surfaces at right angles and that geological structures, like the salt diapirs, can act as free surfaces. A free surface will deflect a principal stress unless that stress happens to be oriented exactly perpendicular to the surface (Bell, 1996b). If stress trajectories encounter a zone that is relatively “harder” or “stiffer” than the surrounding rocks, they will be deflected so that σ_1 intersects at right angles (Figure 2.9a). On the other hand, if the zone is relatively “softer” stresses will be deflected so that σ_1 parallels the interface (Figure 2.9b; Bell, 1996b).

One consequence of the deflection of the stress regime is that the principal stresses adjacent to intrusive salt diapirs may not simply be either vertical or horizontal but instead deflected by the salt-sediment contact to an inclined orientation. Boreholes are subject to the least stress anisotropy and therefore most stable when drilled in an orientation in the plane of σ_1 and σ_3 at an angle determined by the magnitudes of σ_1, σ_2 and σ_3 (Bell, 1996b).

2.6 Aim

The aim of this research is to attempt to determine the stress regime around salt diapirs in the Gulf of Mexico. The salt diapirs are to be interpreted from a 3D seismic data cube from the delta top of the Northern Gulf of Mexico Mississippi-Fan Delta. Two dimensional finite numerical models of the salt diapirs interpreted from the seismic data are to be built to determine the stress regime surrounding the diapirs. The modelled stress orientations will be used to produce borehole stability diagrams that will determine the most stable drilling orientations adjacent to salt diapirs.

3.0: Seismic Interpretation of Salt Diapirs in the Gulf of Mexico Method

3.1 The Data

The survey data for the seismic interpretation was provided by Western Geco. It is 3D seismic reflection data from the Ship Shoal area of the shelf of the Northern Gulf of Mexico Mississippi-Fan delta (Figure 2.8). The survey is 44743m x 16092m with 2230 crossline traces and 1280 inline traces. The seismic sections provided reach a depth of 8.7 seconds.

3.2 The Software

SMT Kingdom ™ 8.3 software was used for the interpretation of the seismic data. Kingdom ™ along with its 3D VuPak extension was used to manipulate; the amplitude data, envelope attribute, phase rotation, the colours and the opacity so that; the top salt horizon and associated faults could be better interpreted.

3.3.1 Interpreting Seismic Reflection Data

When a seismic line is shot, if record quality is good, there are a number of reflections on the resulting section (Figure 3.1). The larger reflections are interpreted as coming from the tops of geologic formations when there is a velocity contrast between the two units (Coffen, 1986). The relationships between reflections within seismic sections were used to interpret stratigraphic units, folds, faults and other large-scale geologic structures.

3.3.2 Identifying Lithology

In order to interpret the top salt-sediment contact, subsurface lithologies must be identified from seismic data. Lithologies respond differently to seismic waves varying the nature of the reflections. The velocity, frequency and amplitude of the wave reflections are affected by the lithology that they pass through and are reflected off.

3.3.2.1 Identifying the Deltaic Sedimentary Overburden from seismic data

Clays and silts are sediments settled from suspension. These sediments tend to be thinly bedded and tend to produce closely spaced reflections (REF). If the depositional area is laterally extensive, the reflections generally show moderate to good continuity. Amplitudes are moderate but dependent on lithology and bed spacing. Chaotic reflection patterns can result from deep-sea current activity, slumping or overpressured mobile shales (Badley, 1985). Coarser clastics can appear in a great variety of thicknesses, shape, and lateral extent. They are deposited in all environments (Badley, 1985). The depositional setting is usually the best guide to identifying clastics coarser than clay and slits. The depositional setting can be interpreted from the internal structure and facies association. Coarse clastics can be characterised by mounded configuration and/or sheet-like forms. Coarse clastics have the ability to modify the topography of the basin floor because high deposition rates can dictate the deposition of successive sediments. In shallow water depositional settings, individual clastic units tend to be thin (Badley, 1985). There are 3 general groups of carbonates classifying the thickness, shape, and lateral extent: 1. Laterally extensive sheet like deposits, 2. Bioclastic deposits, deposited by high energy currents and 3. Build ups, reefs, biotherms, banks, mounds etc. (Badley, 1985). The reflections from the top structural boundary of carbonate units have large positive reflection coefficients as carbonates usually have high velocities and densities compared to other common sedimentary rocks.

3.3.2.2 Identifying Salt from seismic data

On a seismic section, a salt dome is represented by an area of low amplitude, chaotic and unstructured reflections, often extending up from the bottom of the section (Figure 3.2). On a time slice the areas without reflections appears as a blank spot (Figure 3.3; Badley, 1985). In young basins like the Gulf of Mexico, there is a large velocity contrast between the low velocity deltaic sediments and high velocity salt. In the Northern Gulf of Mexico Mississippi-Fan delta salt diapirs have intruded into relatively uncompacted sediments (Wu et al., 1990). Here, the reflection amplitude at the salt-sediment horizon is usually large enough to ensure a moderate to high positive reflection coefficient (Figure 3.2; Badley, 1985). The large reflection coefficients above areas without normal reflections are good starting points for picking salt-sediment boundaries. Stratigraphic layers surrounding salt diapirs may bend upwards as they approach the diapirs due to the velocity contrast.

3.4 Picking Stratigraphic and Structural Boundaries with Kingdom TM

Once a boundary has been selected for picking, there needs to be a means of picking the same horizon throughout the survey area, or at least part of the area. With good data, horizons can be followed across whole sections. Problems arise when there is faulting, bad traces or some other complicating factor. If the reflector becomes poor, such as a break (Figure 3.4a), the reflector can be continued if the reflectors immediately above or below continue parallel and maintain equal spacing over the gap (Figure 3.4b; Coffen, 1986). The picked boundaries on the inline sections must conform to those picked in the crossline sections. If large discrepancies exist between the interpretations of the same structures on different lines, the line need to be repacked so that structures correlate between different lines. Thus, giving the best geologically valid interpretation.

Phase rotation of seismic data makes reflection events correspond with strata rather than with its top or bottom interface; effectively representing seismic reflection events in a lithostratigraphic sense (Mingchen, 2009). The degree of rotation depends on phase spectrum and phase of interest strata in seismic data. If the thickness of strata is close to half of the wavelength, a 90° rotation of zero phase data ensures that the seismic section corresponds with the lithology of the strata (Mingchen, 2009). The thickness and wavelength of the strata within the seismic data provided dictated that a rotation of 45° would be the most effective to analyse the salt and sediment lithologies (Figure 3.5).

The amplitude of reflections can be filtered using the opacity filter in Kingdom ^{TM} VuPak software extension. To better constrain salt-sediment boundaries an opacity filter can be applied to the data (Figure 3.6a). This filter removes the low amplitude waves, including the internal salt reflections. As a result the salt is not visible and represented by dark blank areas (Figure 3.6b). This technique can be used to clearly display large salt diapirs in 3D extending up from the base.

3.5 Identifying Faults

With high quality data, a fault can show up clearly on a seismic section as offsets of reflecting horizons, with breaks on the various horizons following a slanting path on the section (Figure 3.7). This path represents the fault plane as it intersects the seismic line. With 3D data the strike and dip of the fault can be determined. The throw of faults are best interpreted from a seismic section perpendicular to the strike of the fault. Faults not perpendicular to the inline and crossline sections may be interpreted using Kingdom’s ability to digitise angled arbitrary sections, from both the base map and in VuPak, to produce a section perpendicular to the strike of the fault (Figure 3.7).

3.6 Misleading Features

There can be misleading features in seismic data that can be interpreted as structures that do not exist. Multiples and diffractions were all but eliminated from the data in this study during processing due to good 3D migration. Surface or near-surface features can produce misleading anomalies that may affect deeper reflections and must be recognised (Coffen, 1986; Figure 3.8). Velocity anomalies from salt, reefs, igneous features, gas and contorted bedding can produce a nonlinear scale that gives the appearance of geometries that are not true (Badley, 1985). A good velocity model and depth conversion is required to eliminate this (Coffen, 1986). High amplitude reflections within a salt body can be interpreted in a number of ways (Figure 3.9). Internal reflections within the salt may result from: a heterogeneous salt composition, a salt body deposited as multi-stage flow events or it may represent the base of the salt body (REF). Looking for steep and narrow structures like salt diapirs requires long enough lines to detect the steep parts. Large structures may extend past the edge of the seismic lines giving flanks the appearance of: 1. Regional dip or 2. Allochthonous salt interpreted as the base salt layer (Coffen, 1986).

3.7 Recognising Salt Diapiric Structures and Styles from Seismic Data

Once the boundary between overburden and the top of the salt has been identified, a map of inline and crossline interpretations of top salt-sediment contact can be compiled. When the interpreted sections are combined into a map of top salt depth, salt high anomalies can be recognised. These highs are possibly salt diapirs (Hudec and Jackson, 2007).

Salt diapirs are identified and their style classified by the deformation or lack thereof in the surrounding sedimentary overburden. The overburden is deformed differently depending on whether the diapir style is reactive, active or passive. It is important to interpret the diapiric style as it can affect the stress state around the diapir. Active diapirs exhort a pressure out onto the overburden, passive and reactive diapirs do not, as described in the background (Jackson et al., 1994).

3.7.1 Identifying Reactive Salt Diapirs in Seismic Data

Reactive diapirs often have a triangular shape (Figure 3.10a); this comes from the pressurized salt layer supporting the partial weight of each fault block at an equilibrium level. The size of a reactive diapir is controlled by the amount of regional extension. The greater the extension, the taller the diapir, until it subsides. The rate of reactive diapirism is controlled by the viscosity of the salt and the rate of regional extension (Vendeville and Jackson, 1992a). Apart from intense but local shearing along the contacts of the diapir, the fault blocks are relatively preserved during the reactive stage (Figure 3.10b; Vendeville and Jackson, 1992a). Any sediments bent upwards approaching the salt diapir is due to subsidence of the flanks, not force from salt buoyancy as is the case with active diapirism.

3.7.2 Identifying Active Salt Diapirs in Seismic Data

Active piercing and local extensional faulting can form discrete structures visible on seismic profiles (Figure 3.11). Structural styles associated with natural active diapirs include double-flapped arching (Figure 3.11a) and an asymmetric combination of arching and extension (Figure 3.11c), which produces a single flap across the top of a diapir and no crestal graben (Schultz-Ela et al., 1993). Active diapirs can be distinguished from reactive and passive diapirs from the deformation in it's roof: 1. the roof is thinned by extensional faulting and the fault blocks are dispersed outward by entrainment on the spreading, flowing crest of the diapir (Schultz-Ela et al., 1993). 2. The roof strata slump off the domal bulge along internal glide planes (Schultz-Ela et al., 1993). 3. The strata displaced by entrainment or slumping accumulate as chaotic, sporadically overturned and thickened sequences next to the diapir (Schultz-Ela et al., 1993). 4. Erosion can truncate all these structures, leaving only a marked angular unconformity (Schultz-Ela et al., 1993). 5. Dissolution of salt can undermine any remaining roof, causing it to collapse and create new structures-perhaps long after the diapir has been reburied and re-exhumed (Schultz-Ela et al., 1993).

3.7.3 Identifying Passive Diapirs in Seismic Data

Passive diapirs typically evolve to a steep-sided, flat-crested structure (Figure 3.12a). The flat crest could be formed by dissolution or by gravitational spreading of the salt surrounded by air or water (Schultz-Ela et al., 1993). Passive diapirs, unlike other styles of diapirism, are surrounded by strata that show little faulting and thickness changes, and small amounts of folding except for the proximal effect of diapiric drag (Vendeville and Jackson, 1992a). There are not any visible effects of regional extension faulting because: 1. There may be no overburden to be faulted above an emergent diapir (Figure 3.12b; Vendeville and Jackson, 1992a). 2. Regional extension is preferentially accommodated by the salt flowing into widening diapiric walls (Vendeville and Jackson, 1992a). Passive diapirs can revert back to active piercement when sedimentation increases to the point where the diapir is covered by a roof that is thick enough for discrete structures to form within it (Figure 3.12c; Hudec and Jackson, 2007).

3.8 Interpreting Diapir Evolution from Seismic Data

The evolution of diapirs can be recorded in the surrounding successive sediments. Evidence can be found for previous diapir shapes from the migration of depocentres and turtle-back structures. During the mound stage there is syn-depositional thinning of sediments over a mounds crest. As the mound matures into a salt dome, salt is withdrawn into the growing diapir, which leads to a collapse of the flanking sequences and thinning towards the diapir (Cramez, 2006). A secondary depocentre develops above the collapsed areas (Cramez, 2006). Figure 3.13 tracks the salt withdrawal and generation of depocentres around a salt diapir as it grows. The space available for sediments increases locally creating local (Cramez, 2006). The depocentres will be progressively displaced toward the flanks of the dome (Cramez, 2006). The migration of depocenters creates turtle-back structures through the inversion of a structural low to a local high. Turtle-back structures are strata mounded between salt diapirs, having a flat base and rounded crest (Figure 3.14; Cramez, 2006).

4.0 Seismic Interpretation of Salt Diapirs in the Gulf of Mexico.

The seismic interpretation of the study area focussed on the top salt horizons and associated deformation within the sedimentary overburden. Salt diapirs and their distribution, type, geometry and extent of evolution were interpreted. The contact between the top of the salt and the deltaic sedimentary overburden was picked on 128 inline and 223 crossline seismic sections throughout the study area at 10 trace intervals. The top salt levels in TWT that were picked from all of the inline and crossline sections were combined and visualised as a map (Figure 4.1). The same time data was also visualised in 3D using Kingdom VuPak (Figure 4.2). The 3D image shows clearly the presence of structural highs and lows. Anomalistic highs in the salt structure may represent salt diapirs, and the lows may represent the associated salt withdrawal basins or the base of the salt layer. Figure 3.3 is a 1 second time slice from the 3D seismic cube. The 'blank spots' or areas with chaotic low reflection coefficients are salt diapirs. These show good correlation with the structural highs (i.e. Diapirs) in the top salt TWT map of Figure 4.1. At this level (1 second) the salt structures appear to be ellipsoid to circular shaped and relatively evenly distributed (King et al., in press).

4.1 Salt Diapirs in the Gulf of Mexico

Six salt diapirs were recognised and interpreted in the Ship shoal 3D seismic data cube (Figure 4.1). The diapirs were classified into 1 of 2 styles: Active diapirs (1, 2, 3 and 6) and Reactive diapirs (4 and 5). No passive diapirs were identified.

4.1.1 Group 1: Active diapirs

4.1.1.1 Diapir 1

Diapir 1 (Figure 4.1), was interpreted as an active dome due to its shape and the extensive deformation in the surrounding sediments (Figure 4.3a). Sedimentary layers in the roof thin towards and dip away from the diapir. The diapir has a double flapped roof structure (Figure 3.11a). The roof is thinned by extensional normal faulting above the crest of the diapir. The syn-deformational sediments reach the surface (Figure 4.3b). The diapir is surrounded by salt withdrawal basins and their depocentres migrate towards the dome. This is evidence of an earlier mound stage. Further evidence comes from the turtle back structures flanking the dome (Figure 4.3b).

4.1.1.2 Diapir 2

Diapir 2 is currently an active dome (Figure 4.1). The roof is thinned by extensional normal faulting above the crest of the diapir (Figure 4.4). Near the diapir crest, down to a depth of 1.1sec (TWT), the sedimentary layers in the roof dip away from the diapir as if they were forcefully pushed up and aside. The sedimentary layers deeper than 1.1sec (TWT) are well preserved and near horizontal right up until they are truncated by the side of the salt diapir (Figure 4.4a). This implies that the diapir once grew passively but has since been buried, likely due to either an increase in sedimentation or a decrease in the salt supply. Below depths of around 2.4sec the diapir is shaped like an active salt mound. The salt is more pronounced due to differential loading but the largest influence on the shape comes from the withdrawal basins flanking the diapir.

4.1.1.3 Diapir 3

Diapir 3 is an active dome (Figure 4.1). The roof is thinned by extensional normal faulting above the crest of the diapir (Figure 4.5). The sediments thin towards the dome with a double flapped structure (Figure 3.11a). The diapir is surrounded by salt withdrawal basins. The basins either side of the diapir, just a few kilometres apart, consist of sediments with differing seismic responses (Figure 4.5a). These differing seismic responses indicate that the basins contain either different sedimentary rocks or the same sedimentary packages, just differing in thicknesses. This can be caused by basin subsidence at different times or at differing rates. The depocenters migrate towards the dome, indicating that the diapir evolved from a salt mound. The salt to the northern flank of the dome looks to be depleted, forming a salt weld. A salt weld is formed when the top and bottom contacts of the salt to merge due to the expulsion of the salt.The lack of salt may stunt further growth of the diapir or influence the shape of the diapir as it continues to grow.

4.1.1.4 Diapir 6

The interpretation of diapir 6 is limited in its accuracy by its location on the available seismic lines (Figure 4.1); only part of the diapir is contained within the seismic data survey boundary (Figures 4.6). However, it was interpreted as if the diapiric style of the visible section is representative of the whole structure. Diapir 6 is an active dome with radiating normal faults from a central point on the crest (Figure 4.6b). The extensive faulting above the crest gives the appearance of a phantom growth fault (Figure 4.5b). There is thinning and turning up of the truncated sedimentary layers towards the salt dome. The diapir is surrounded by salt withdrawal basins. The salt diapir has intruded up a fault; the diapir is not considered reactive because the extension is created by the active piercement of the salt, induced by differential loading from the overburden.

4.1.2 Group 2: Reactive Diapirs

4.1.2.1 Diapir 4

As is the case with diapir 6, the interpretation of diapir 4 is also limited in its accuracy by its location as there are very few orientations to view the diapir in seismic section (Figure 4.1). Diapir 4 is a reactive diapir (Figure 4.7a). Normal faults above the diapir extend the overburden to compensate for the salt withdrawal from the adjacent basin (Figure 4.7b). The sedimentary roof or flaps are not pushed up above the diapir as is observed above active diapirs (Figure 3.11; Vendeville and Jackson, 1992a). The fault blocks are suspended by the salt pressure (Vendeville and Jackson, 1992a). The sedimentary roof is well preserved.

4.1.2.2 Diapir 5

Diapir 5, located in the south west of the survey area, is a reactive salt mound (Figure 4.1). The salt withdrawal in the surrounding basins has triggered extension above the salt mound (Figure 4.8). The fault blocks above the diapir are thinning and spreading. The diapir is not yet a salt dome; it is at the residual salt high stage of diapir evolution. A lack of salt supply from the diapirs flanks may have stunted its growth. The surrounding sediments have subsided around the mound creating the antiform (Figure 4.8b). In crossline sections the poorly imaged overburden takes the appearance of a synform, this is due to displacement of the fault blocks (Figure 3.10b). This is confirmed when the structure is observed on an inline section.

4.2 Regional Interpretations

4.2.1 Far Field Tectonic Forces

Discrete relatively ellipsoidal diapirs are observed with a uniform distribution in the seismic cube (Figure 3.3). Elliptical shaped diapirs form when under a slightly extensional tectonic regime, where σ_1 is σ_V and σ_{Hmax} and σ_{Hmin} are near equal. The diapirs deform by lateral and vertical flowage of salt. This creates withdrawal, which will control the accommodation space for deformed sediments (REFS).

Under such tectonic conditions normal-faults radiating from diapir crests, thin and extend the overburden. Faults strike parallel to σ_2 according to Mohr theory. Illustrated by Curry's model the extension produced by the normal faulting is higher than the apparent shortening produced by the piston uplift (Figure 4.9). When a salt layer flows upward the overburden is extended above it. The extension above the diapir crests creates radial normal-faults which extend the overburden in order to fill the space created by salt withdrawal from the diapir flanks (Figure 4.10).

4.2.2 Allochthonous Salt Sheet

In the study area the average depth of the salt layer feeding diapirs 1-6 is around 3.2 sec. This is not consistent with the previous research that found the base Louann salt layer in the Sigsbee Escarpment to be approximately 10km deep (Figure 4.11; Wu et al., 1990). The depth of around 4km for the base salt seen in this study suggests that the salt layer feeding the diapirs is an allochthonous salt sheet. Allochthonous salt structures are sheet-like salt bodies tectonically emplaced at stratigraphic levels above the source layer, such that the salt overlies stratigraphically younger strata. (Bally, 1981; Worrall and Snelson, 1989). The seismic data is not extensive or deep enough to confirm this theory but it is a strong possibility.

5.0 Finite Numerical Modelling of Salt Diapirs Method

5.1 ABAQUS ^{TM} Program

ABAQUS^{TM} CAE (Complete Abaqus Environment) is a well-recognized industry standard finite-element modelling program that produces robust mechanical simulations combining physical mechanical laws. The program allows models to be created and their geometries and parameters altered. Rock properties, such as density and Young’s Modulus, can be assigned to the models parts, made up of individual elements. ABAQUS^{TM} was used to construct two-part 2D models of salt diapirs intruding into sediments with varying geometries, rock properties and frictional coefficient of the interface between the salt and sediments.

5.2 Model Building

The process of constructing a model in ABAQUS ^{TM} CAE involves:

- Establishing the model dimensions and parts.
- Material properties: density, Young’s Modulus and Poisson’s Ratios are given to each of the parts.
- The parts are assembled and the contact is given a coefficient of friction.
- The model is loaded with gravity.
- The boundary conditions are defined.
- A quad free distributed mesh is applied.
- The model is now run to completion.
- The input file is then renumbered.

- Pore pressure is added to the model.
- The deformational mechanisms, Drucker-Prager Shear Criterion and Creep, are defined and added to the model.
- The Initial stresses are exported and then input into the final model in order to pre-stress it.
- The Final model is run.
- Results are analysed in the ABAQUS ^{TM} visualisation module.

5.2.1. Model Dimensions

The coordinates of each part of the model were plotted, incorporating the diapir and distant model boundaries (Figure 5.1). The boundaries were plotted at a distance far enough away from the diapir as not to significantly influence the mechanical deformation around the diapir. The East and West boundaries of each model are each 100km from the central diapir. The initial models vary in depth. The models of the interpreted diapirs are 20km deep so that the base is approximately ~15km deeper than the sediments.

Two sets of models were built. The models of set 1 are initial ‘proof of concept’ models, constructed to test and refine the parameters and variables to be used on the interpreted diapirs. The models of set 2 are the models of the interpreted diapirs 1-6, built to examine the stress regime adjacent to salt diapirs in the Gulf of Mexico.

The dimensions of the initial models of set 1 made use of the simple depth converted geometry of diapir 1, as well as a series of simple symmetrical shallow and deep diapirs. The geometry for the Model 2 was taken from a representative seismic section of diapir 1 (Figure

5.2a). Model 3 was designed with a symmetrical shape (Figure 5.2b). This model had three parts: the overburden; the salt, and; the basement. These three parts replicate the conditions of the Gulf of Mexico. Model 4 had just the one contact interaction along with the symmetrical geometry (Figure 5.2c). Model 5 was created to observe the influence of the depth of the diapir as well as the gradient of the diapir flanks. Within the one model were two diapirs; one tall and shallow; other short and deep (Figure 5.2d). Model 5 to Model 13 used this duel diapir geometry.

Model dimensions of set 2, diapir 1 to diapir 6 (Figure 5.3), were taken from the seismic interpretation (Figures 4.3, 4.4, 4.5, 4.6. 4.7 and 4.8). The diapirs are depth converted representations of the top salt. The depth conversion of the overburden used a velocity model of the Gulf of Mexico (Table 5.1; taken from Wu et al., 1990). This velocity data was recorded on the shelf and uppermost slope areas near Louisiana, close to the Ship Shoal survey area. These velocities were adequate to eliminate the pull-up effects for the purpose of depth conversion in this study (Table 5.1). The top salt in the study area did not reach depths of 7 seconds (TWT) and the influence on the depth conversion by the water depth in the sections was negligible. Therefore, the sections could be simply traced then stretched (Figure 5.4) according to the formula:

$$\text{Depth} = \text{TWT}/2v$$

Equation 1. Simple depth conversion formula. v is velocity (Table 1)

5.2.2. Rock Properties

The sediments in each model were assigned properties of density, Young's Modulus, Poisson's Ratio, pore fluid pressure and density (increasing with depth). The salt part was assigned a homogeneous density, Young's Modulus, Poisson's Ratio.

5.2.2.1 Density

The density of halite is 2163 kg/m^3. However, naturally occurring rock salt rarely consists of pure halite, so salt density depends on the proportion and mineralogy of impurities (Carmichael, 1984). The Louann salt is typically observed to be 98% Halite with 2% impurities (1.6% Anhydrite, 0.1% quartz, 0.1% gypsum, 0.1% smectite; Fredrich et. al., 2007). A common approximation is that the impurities found in the Louann Salt, increase salt density to 2200 kg/m^3 (REF).

The density of the sediments depend on both lithology and compaction state (Hudec and Jackson, 2007). A large dataset of density-depth pairs in the Gulf of Mexico wells compiled by Fairchild and Nelson (1989, Figure 5.5). This has been used to help determine realistic grain densities for the sediment overburden at a given depth; where a particular density is defined by the equation:

$$\rho=1400+172z^{-0.21}$$

Equation 2. Exponential density gradient used for sediments parts of the models. ρ is density, z is depth.

5.2.2.2 Young's Modulus

Young’s Modulus was used as a measure of sediment rigidity in this study. Young’s Modulus represents the stiffness of the material, or the ease at which the material undergoes strain for a given stress and is defined as the “ratio of the uniaxial stress over the uniaxial strain in the range of stress in which Hooke's Law holds” (Engelder and Marshak, 1988). Soft rocks, such as salt and highly fractured sedimentary rocks have a low Young’s Modulus (e.g. Salt), whilst stiff rocks such as dense, compacted and non-fractured sediments have a higher Young’s Modulus (e.g. Sandstone; Gudmundsson, 2004). ABAQUS ^{TM} models may utilise just one Young’s Modulus value for each part; In the Gulf of Mexico, the Young’s Modulus of the sediments is not homogeneous and generally increases with depth. Therefore, the accuracy of Young’s Modulus values in the models is limited. Young’s Modulus values were taken from research on rock properties in the Gulf of Mexico (Park et al., 2008; Liang et al., 2006; Rath et al., 2009). Young’s Modulus values of 3.1 GPa for the salt part and 34 GPa for the sediment part were used in each model (Tables 5.2 and 5.3).

5.2.2.3 Poisson’s Ratio

Poisson’s Ratio is the ratio of the transverse strain (contraction perpendicular to the applied load), to the axial strain (extension in the direction of the applied load) when an object is stretched. Values of Poisson’s Ratio have been observed to vary from 0.25 to 0.5 for salt (Liang et al., 2006). The Poisson’s Ratio for slightly impure salt as is found in the Gulf of Mexico is 0.3 (Liang et al., 2006). The sediment parts were assigned a Poisson’s Ratio of 0.3 derived from well data taken from deltaic sediments (King et al., 2010; Tables 5.2 and 5.3).

5.2.3. Assembly

Two parts were combined (Figure 5.6) and the interaction along the contact between the two parts was given a coefficient of friction.

5.2.3.1 The Salt-Sediment Contact Coefficient of Friction

The contact interaction between the salt and sediment parts may be given a coefficient of friction. The ability of salt to flow in the subsurface is limited by the thickness of the overburden and the boundary drag along the top and bottom surfaces of the salt layer (Hudec and Jackson, 2007). The coefficient of friction between the two parts was modelled initially as a rough contact with no sliding. Faults within sedimentary rocks have a typical coefficient of friction of 0.6 (Byerlee, 1968). Luján et al., (2001) measured the coefficient of salt layer décollements in thrust faulting as 0.43. Fiction coefficients of 1 for the initial models and 0.43 for the models of the interpreted diapirs were used.

5.2.4. Loads

A distributed gravity load of -9.81ms^{-2} was applied to all of the models in this study (Figure 5.7).

5.2.5. Boundary Conditions

The models were given boundary conditions that closely mimic conditions in nature where sediments are loaded onto a layer of salt, which is subsequently confined but is allowed to deform. The vertical sides of the models were completely restricted in their ability to rotate and move laterally. The bases of the models were completely restricted in their ability to rotate and move vertically (Figure 5.8). The top boundary was allowed to move freely.

5.2.6. Mesh

The models were given a quad-shaped freely distributed mesh made up of elements confined by four nodes. The smaller the element size the higher the accuracy of the deformation and the resolution of the stress analysis (Figure 5.9). The initial models had a mesh sizes ranging from 250m to 150m. The models of the interpreted diapirs had a mesh size of 150m.

5.2.7. Initial Run of the Models

The model is run to produce an input file. An input file is needed to add pore fluid pressure, overpressure, creep deformational mechanism, Drucker-Prager deformational mechanism and initial stress conditions for pre-stressing.

5.2.8. Renumbering

The models must be renumbered before pore fluid pressure and initial stress conditions can be added. The original ABAQUS^{TM} output numbers the nodes and elements of each part discriminately. Each part has its nodes and elements numbered starting from one. The nodes and elements must be renumbered so that each node and element has a unique number.

5.2.9. Pore Fluid Pressure

Pore fluids are fluids that occupy pore spaces in a soil or rock. Pore fluid pressure plays a critical role in subsurface stress regimes and rock failure. The effective stress, (σ_n – pore fluid pressure) rather than the absolute normal stress (σ_n) controls the resistance to rock failure (Handin et al., 1963). High pore fluid pressures can reduce the effective stress to failure (Handin et al., 1963; Hillis, 2007). This can be visualised using a Mohr circle diagram (Figure 5.10). Overpressure of pore fluid pressure shifts the effective stress towards the failure envelope and depletion of pore fluid pressure shifts the effective stress away from the failure envelope (Figure 5.10; Hubbert and Rubey, 1959; Rice, 1992). The parts require permeability and void ratios before pore fluid pressure is added. (Hamilton, 1976)

5.2.9.1 Reactive Diapir Models

For the models of reactive diapirs, the sediment parts were given a depth dependant pore fluid pressure gradient and the salt parts were not given pore fluid pressure values, as salt has a crystalline structure with insignificant porosity. A gradient of 12MPa/km was used for the pore fluid pressure of the sediments. This pore fluid pressure gradient falls within the envelope created by the hydrostatic gradient (9.81MPa/km) and the lithostatic gradient (24.5MPa/km; Dutta, 1997; Figure 5.11). For a particular pore pressure gradient, the pore-fluid pressure at each node was calculated as:

$$Pp = z * 12000$$

Equation 3. Pore fluid pressure gradient. Pp is pore fluid pressure in pascals, z is depth of the node in meters

5.2.9.2 Active Diapirs

A pressure was added to salt in the models of diapirs 1, 2, 3, and 6 to stimulate active diapirism. The aim was to pressurise the salt so that it could more than overcome the load applied by the sediments under the influence of gravity. The pressure had to have a negative gradient to allow for pressures deep in the model to be accommodated within the boundary conditions. The modelling software would not accept pore fluid pressure within the sediment part, in the way the input file was formatted.

5.2.10. Deformation Mechanisms

The sediments were allowed to deform by a combination of linear elastic and Drucker-Prager failure. The salt was allowed to deform by a combination of linear elastic and creep deformation.

5.2.10.1 Drucker-Prager Failure

The sediments were allowed to deform via Drucker–Prager yield criteria. The Drucker–Prager yield criterion refers to the point at which deformation changes from elastic to plastic (Figure 5.12; Bottero et al., 1980). The lack of borehole data from the survey area meant that the yield stresses from experimental data of the Gosford Sandstone had to be used as an analogue for the overburden (Table 5.6; Ord et al., 1991).

5.2.10.2 Creep

Creep is the tendency of a solid material to slowly move or deform under the influence of stresses (Hansen, 1977). It occurs as a result of long term exposure to high levels of stress that are below the yield strength of the material (Hansen, 1977). The uniaxial Norton-Bailey law creep power law was adopted:

$$\epsilon^c = A\sigma^n t^m$$

Equation 4. The uniaxial Norton-Bailey law creep power law. ϵ^c is creep strain component, A is creep material constant, σ is stress, ^{n} is creep law stress index, t is time and ^{m} is creep law time power (Shen, 2010).

All models with creep deformation utilised a creep material constant of $10^{-21.8}$, a creep law stress index of 2.667 and a creep law time power of -0.2.

5.2.11. Pre Stressing

Once the elements have also been renumbered and pore pressure added the model can be pre-stressed to ensure that the model is in equilibrium with gravity and does not compact when gravity was applied. The model is pre-stressed to equilibrium with gravity. The magnitudes of the normal stresses s11, s22 and the shear stress s12 are input into the final model to resist gravitational collapse.

The Poisson’s Ratios were changed from 0.5 in the initial model to 0.3 in the final model. The k ratio formula for uniaxial-strain condition:

$k = n / (1-n)$

Equation 4. (n is the Poisson's Ratio)

A Poisson’s Ratio of n=0.5 should achieve k=1 so that the normal Poisson's ratio of 0.3 can be used. If the same Poisson's ratio of 0.3 is used the model would have continued to collapse under the influence of gravity as the pre-stress obtained using that Poisson's ratio of 0.3 gives a k of 0.5.

5.2.12. Final Model Visualisation

The ABAQUS^{TM} Visualisation module is used to view the model results.

6.0 Finite Numerical Modelling of Salt Diapirs Results

ABAQUS^{TM} visualisation module was used to view the results of both the initial modelling and the models of the diapirs 1-6. The software can display each model post deformation with superimposed results of stress, pore fluid pressure and displacement as either contours or tensors. Colour indicates the magnitude of contoured results (e.g. Pore fluid pressure). The lengths of the lines indicate the magnitude when results are displayed as tensors (e.g. stress).

ABAQUS^{TM} visualises stress as tensors of the principle in-plane stresses S_{11}, S_{22} and S_{33}. S_{11} represents the maximum principle stress, σ_1, as the models have just two dimensions. Pore pressure and the pressure added to the salt were displayed as a coloured contour. The horizontal (U1) and vertical (U2) displacement in the sediments was visualised as a coloured contour to indicate areas of extension (Red), shortening (Blue) or areas without displacement

(Green). The vertical displacement should be as close to zero as possible for models in equilibrium with gravity. Stress orientations and magnitudes were visualised as tensors (Figure 6.1). The red lines represent σ_1, σ_2 comes out of the page and σ_3 was coloured green to better emphasise the orientation and magnitude of the maximum principle stress. The magnitude is proportional to the length of the tensor.

6.1 Initial Models

The initial models were intended to simulate the stress state of diapirs in an isotropic tectonic environment with only limited differential loading forcing salt movement. This predicts the stress state around reactive and passive diapirs.

Model 2 showed mass movement within the sediments due to the unsymmetrical shape of the diapir. The orientation of σ_1 is deflected to parallel with the salt-sediment contact of the diapir (Figure 6.2). At depth the orientation of σ_1 remains perpendicular to the salt-sediment contact.

An attempt was made to control for the influence of topography in Model 3 with symmetrical salt and sediment parts. The model also had a basement part to better imitate conditions observed in nature. Model 3 did not reach completion as ABAQUS^{TM} would not run the model with pore fluid pressure while there were two contact surfaces between parts.

Model 4 had a symmetrical representative shape, one surface contact and a finer mesh. This eliminated the horizontal mass movement within the sediments to focus on the principle of the maximum stress deflections at the salt-sediment contact for reactive and passive diapirs.

The regional σ_1 is vertical; this is representative of the extensional tectonic setting on the delta top of the Gulf of Mexico (Rowan, 1997; King et al., 2009). The maximum principle stress was deflected parallel to the salt-sediment contact (Figure 6.3). There is a gradual transition from a perpendicular σ_1 stress state over the base salt layer to a parallel σ_1 stress state on the salt diapir flanks (6.3).

Model 5 was created to determine how the orientation of σ_1 is influenced by the depth of a diapir and the dip of its flanks. Two diapirs were included in this model; one tall with steep flanks at a shallow depth, the other short with shallow dipping flanks at a deeper depth (Figure 6.4). The orientation of σ_1 stress around tall, steeply flanked diapir salt-sediment contact was deflected parallel as in model 4. The orientation of σ_1 above the shallow tall diapir is parallel to the diapir overburden boundary right up to the surface (Figure 6.4a). Above the short, deep diapir with shallow dipping flanks the orientation of σ_1 is gradual rotated from a vertical σ_1 orientation near the surface to a σ_1 orientation parallel with the salt-sediment contact. The short, deep diapir with shallow dipping flanks shows how pervasive the stress deflections are within the overburden (Figure 6.4b).

Model 7 was constructed using tri-elements (elements with 3 nodes as opposed to the 4 node quad elements used in other models) in order to try and give the elements a more uniform distribution and size. However, ABAQUS ^{TM} could not handle the model once pore fluid pressure was added to the input file.

Model 8 had tri-elements and no pore fluid pressure. The lack of pore fluid pressure resulted in stresses with magnitudes higher than the magnitudes observed in the models with pore fluid pressure. The lack of pore fluid pressure also results in an effective stress that resists rock failure more than would be expected in the Gulf of Mexico (Figure 5.10; Handin et al., 1963; Hillis, 2000).

Model 9 was used to vary the pore fluid pressure within the sediment part. The pore fluid pressures tested were 9.8MPa/km (hydrostatic gradient), 12MPa/km and 22MPa/km (lithostatic gradient). The results were consistent with the Coulomb criterion, that pore fluid pressure has an influence on the observed normal stresses (Figure 6.5; Handin et al., 1963; Hillis, 2000).

Models 1 to 9 used a homogeneous density value for the sediment part. In the deltaic setting of the Gulf of Mexico, this is not the case (Hudec et al., 2009); to better imitate conditions found in the Gulf of Mexico the sediment parts in Models 10 to 13 were built to give the sediment part a gradational density. The gradational density had an influence on the stress magnitudes when compared to the homogeneous density in previous models. The stresses in the sediments with gradation of density had lower magnitudes at shallow depths and larger magnitudes deeper in the sediments (Figure 6.5).

6.2 Finite Diapir Models

6.2.1 Type 1 – Active

Simple differential loading was insufficient to model active diapirism in the initial models. The models of diapirs interpreted as active (diapirs 1, 2, 3 and 6) required the salt to be overpressured in order to give the required buoyancy force for the salt to actively deform the overburden. Figure 6.6 shows a colour contoured visualisation of the pressure added to the salt layer of model diapir 1. The overpressure of the salt will cause the stress to deflect as if it is stiff (Zhang, 1994).

The vertical displacement inside the models is displayed as a colour contour (Figure 6.7). The visualisation shows uplift at the diapir crest. The uplift of the salt is accommodated by extension in the overburden immediately above the diapir. The extension is interpreted from a combination of the observed displacement in the overburden and the stress orientation above the diapir. In nature this extension would be accommodated by normal faults immediately above the diapir crest.

The stress orientations and magnitudes of the active diapir models were visualised. The orientation of σ_1 in each model is perpendicular to the salt-sediment contact of the diapirs (Figure 6.8). The orientation of σ_1 is perpendicular to the salt-sediment contact of the diapir crest; normal faulting is possible in this region of the model. This is consistent with what is expected for active diapirism, where there is forced extensional normal faulting above the diapir crest (Jackson et al., 1994).

There are limitations to the accuracy of the active diapir models. All attempts to give the interaction between the salt and sediment parts a realistic coefficient of friction failed to run to completion. Also there is transition where the overpressure of the salt part is overcome by the pressure exerted by the weight of the overburden. It is recommended that the overpressure given to the salt part in future models is adjusted so that this transition zone is at a depth, deep enough that it will not affect the nearby stress at all.

6.2.1.1 Diapir 1

The model of diapir 1 simulates an active salt dome. The orientation of σ_1 is perpendicular to the salt-sediment contact of the diapir and the deeper base salt (Figure 4.9). The regional orientation of σ_1 to either side of the diapir flanks is horizontal; this indicates that the sediments either side of the diapir are under a compressional regime to accommodate the uplift and extension immediately above the diapir crest.

6.2.1.2 Diapir 2

The model for diapir 2 simulates an active salt dome. The orientation of σ_1 is generally perpendicular to the salt-sediment contact of the diapir and the deeper base salt (Figure 6.10). The orientation of σ_1 next to the steep left side of the diapir is parallel to the salt-sediment contact. This is likely due to the steep geometry that limits the influence of the outward pressure exerted by the salt diapir.

The stress along the boundary of diapir 2 contains areas of compression. The rough contact interaction between the salt and the sediment contact cannot accommodate the displacement along the complex shape, creating areas of compression consistent with the highs and lows of the surface. ABAQUS^{TM} modelling software would not run the model of diapir 2 with a coefficient of friction of 4.3, limiting the areas of compression to this one particular model. Therefore, the areas of compression should not be incorporated into predictions of the stress state around diapir in the Gulf of Mexico.

6.2.1.3 Diapir 3

The model for diapir 3 simulates the interaction between the two active salt domes 3 and 6. The orientation of σ_1 is perpendicular to the salt-sediment contact of each diapir (Figure 6.11). The diapirs are too distant to significantly influence the stress around the other. They act as two discrete diapirs at this distance. The pervasiveness of the deflections was not quantified as the distance is dependent on the material properties, depth and geometry within the model.

6.2.1.4 Diapir 6

The model for diapir 6 simulates an active salt dome. As is the case with the previous active diapir models, the orientation of σ_1 is perpendicular to the salt sediment boundary of the diapir, and similar to the model for diapir 1 there is compression either side of the diapir to accommodate the extension immediately above the crest but unlike diapir 1, the compressional stress in diapir 6 is over come at depth by the weight of the sedimentary overburden (Figure 6.12). The orientation of σ_1 is rotated from horizontal near the surface to vertical at depth near the salt-sediment contact.

6.2.2 Type 2 – Reactive

The models of the reactive diapirs (diapirs 4 and 5) were allowed to deform by differential loading and gravitational collapse. Unlike the active diapir models, the reactive models did not have a pressure added to the salt. The buoyancy of the salt in the reactive models is only enough to support the weight of the overburden, and not enough to deform it. The reactive models have pore fluid pressure added to the sediment part (Figure 4.13). A sediment part with gradational pore fluid pressure should produce stress magnitudes more concordant with those found in nature e.g. vertical stress in sedimentary basins is often assumed to increase at 1.0psi/ft with depth (Tingay et al., 2003). The higher the pore fluid pressure the closer the effective stresses are to the failure envelope and rock failure (Figure 5.10; Handin et al., 1963; Hillis, 2000)

Displacement, or lack thereof, was displayed as coloured contours. The overburden directly above the diaper crest is static indicated by the green colour (Figure 6.14). The sediments to the left of the diapir have been slightly uplifted and the sediments on the right side of the diapir have subsided. The displacement is likely a response to the differing thickness of the sediment part either side of the model applying different loads on the deformable salt part.

The orientation of σ_1 is deflected parallel with the salt-sediment contact of the diapir (Figure 6.15). At depth, σ_1 remains perpendicular to the boundary. The orientation of σ_1 above the diapir crest is horizontal, which can describe either a compressional environment or if stresses are similar in magnitude it may show an isotropic stress state in a 2D model. The horizontal orientation of σ_1 compared with the lack of displacement observed above the diapir crest suggests that above the diapir crest is an isotropic stress state. An isotropic stress state is expected around reactive diapirs when there are no far-field stresses applied to the models, as the salt is simply in equilibrium with the weight of the overburden.

6.2.2.1 Diapir 4

The model for diapir 4 simulates a reactive salt dome. The orientation of σ_1 is deflected to parallel to the contours of the salt-sediment contact of the diapir (Figure 6.16). As is the case with the initial models, σ_1 deflected perpendicular to the base salt layers both at shallow and deeper depths. The rotation of the orientation of σ_1 from parallel to perpendicular to the salt-sediment contact occurs gradually at the base of the diapir flanks.

6.2.2.2 Diapir 5

The model for diapir 5 simulates a reactive salt mound. Diapir 5 is a mound with a wide flat crest. The edges of the plateau and the flanks act as a reactive diapir, where the orientation of σ_1 is deflected to parallel with the salt-sediment contact of the diapir (Figure 6.17). However, over the crest is a wide flat area that responds as if it was a base salt layer. Here, the orientation of σ_1 is perpendicular to the salt-sediment contact, implying that the diapir crest is too flat and wide for σ_1 to be deflected to the edges and around the diapir.

7.0 Discussion

The seismic interpretation of the seismic data using Kingdom^{TM} software demonstrated 6 discrete salt diapirs and their distribution, type, geometry and maturity. Two different styles of diapir piercement were identified: 1. Active diapirs, salt structures 1, 2, 3 and 6 were identified as diapirs actively piercing the overburden, and; 2. Reactive diapirs, salt structures 4 and 5 were identified as diapirs reactively responding to extension of the overburden. On the 1 second time slice (Figure 3.3) the salt structures appear to be ellipsoid to circular shaped and relatively evenly distributed (King et al., in press). The general shape of the salt structures infers that the regional stress regime is slightly extensional. The structures may be evenly distributed due to the Rayleigh-Taylor instability principle (Sharp 1984; Figure 3.3). The study area is located on a delta top; the delta top is an extensional setting, allowing for reactive diapirism. The base salt layer from which the identified diapirs grew is an allochthonous salt sheet, located at a depth of approximately 3s (TWT).

Two-dimensional finite element models were constructed from the top salt structural boundary, of representative seismic profiles for each of the six interpreted diapirs. Although the delta top is an extensional setting, the models were run under isotropic tectonic conditions (Finkbeiner et al., 2001). The salt parts of the models with active diapirs were given a pressure sufficient to overcome the pressure of the sedimentary overburden above the diapir crests. The salt parts of the reactive models were unpressurised. The models resulted in stress orientations and magnitudes influenced by: 1) the contrasting rock stiffness; 2) pore fluid pressure; 3) the interaction coefficient of friction; 4) the geometry, and; 5) the style of diapirism.

The contrasting geomechanical rock properties of the salt and sediments cause the stress to be deflected (Zhang, 1994). It is known that principal stresses intersect free surfaces at right angles and that geological structures, like the salt diapirs, can act as free surfaces. A free surface will deflect a principal stress unless that stress happens to be oriented exactly perpendicular to the surface (Bell, 1996b). If stress trajectories encounter a zone that is relatively “harder” or “stiffer” than the surrounding rocks, they will be deflected so that the σ_1 intersects at right angles. On the other hand, if the zone is relatively “softer” stresses will be deflected so that the σ_1 parallels the interface (Bell, 1996b). The influence on the magnitude by the pore fluid pressure within the rock was consistent with Mohr Coulomb theory; greater pore fluid pressures reduce the principal stresses. The sediment part of the active diapir models would not accept pore fluid pressure. Therefore, the stress magnitudes within the in the sedimentary overburden of the models with active diapirism will be slightly exaggerated. The stress state responded differently to each diapir style. The reactive models, with unpressurised salt, rotated the orientation of σ_1 parallel to the diapirs structural boundary while the active models, with pressurised salt, rotated the orientation of σ_1 perpendicular to the diapirs structural boundary.

7.1 Reactive Diapirs

The orientation of σ_1 was rotated from the regional vertical σ_1 to an orientation that follows parallel with the salt-sediment contact of the reactive diapirs. The stress follows the geometry until the base of the diapir flanks; here the rotation occurs gradually transitions to a σ_1 orientation that is perpendicular with the base salt layer. A parallel orientation of σ_1 over the diapir crest can indicate a zone of compression, however, once the movement within the model was queried, it was discovered that there was little to no movement over diapir crests, suggesting that the horizontal stresses are isotropic and not under compression.

7.2 Active Diapirs

The orientation of σ_1, in the models with active diapirism, is rotated perpendicular to the salt–sediment contact of the diapirs. The orientation of σ_1 was also rotated perpendicular to the base salt layer at depth. An analysis of the movement within the model shows that there was uplift and extension above the diapir crests. The movement combined with the near vertical σ_1 over the diapir crest infer that the overpressured salt simulated extension forced by the active piercement of the diapirs. The lack of a coefficient of friction given to the salt sediment interaction of the models of active diapirs had an effect on the stress. This was most prevalent in the model of diapir 2, where the small amount of available sliding was unable to accommodate the displacement, causing compensatory zones of compression (Figure 6.10a).

The large difference in stress orientation between the two diapiric styles emphasises the importance of accurate seismic interpretation. Incorrect interpretation of diapiric style can produce errors in the stress orientation of as much as 90 degrees.

8.0 Implications

8.1 Borehole Stability

The stress state of an area has implications for borehole stability. Weak sediments that are subject to high isotropic stress are liable to be mechanically unstable around wellbores (McLellan, 1994). Breakouts and drilling-induced tensile fractures (DITFs) occur when stress magnitude anisotropy perpendicular to the wellbore is higher than the rock strength (Figure 2.7; Bell, 1996). Borehole breakouts may be minimised by drilling in an orientation that subjects the well to the least stress anisotropy (Hillis and Williams, 1993). Raising the mud weight above pore fluid pressure levels will exert a differential pressure on the borehole wall that limiting drilling induced tensile fractures (Zoback et al., 1985).

In a regional extensional stress regime such as the Gulf of Mexico delta top, the greatest stress anisotropy occurs between the vertical stress ($\sigma_V = \sigma_1$) and the minimum horizontal stress ($\sigma_{Hmin} = \sigma_3$) (King et al., 2011). Therefore, the most stable wells are drilled at an angle in the plane with the σ_{Hmin} and the σ_V that subjects the borehole to the least stress anisotropy (Figure 8.1; Zhang, 1994; Peska and Zoback, 1995). Horizontal boreholes drilled toward the regional σ_{Hmax} orientation would be the least stable as they are subject to the greatest stress anisotropy (between σ_V and σ_{Hmin}; Hillis and Williams, 1993).

The modelling results showed that the stress regime surrounding the salt diapirs is complex (Figure 6.2). Boreholes drilled adjacent to salt diapirs that are within the region of the stress deflections must be planned with respect to the deflected stress field and not the regional stress field (Figure 8.2 and Figure 8.3). Figure 8.2 is a schematic representation of the reactive diapir 4; with a σ_1 parallel to the salt-sediment contact of the diapir (b, c) and perpendicular to the salt-sediment contact of the base (a). The most stable drilling directions for each stress orientation are represented in terms of borehole breakout stability diagrams (Figures 8.2 a_{BO}, b_{BO}, c_{BO}); and DITF stability diagrams (Figures 8.2 a_{DITF}, b_{DITF}, c_{DITF}). The stress state over the base salt (a) of diapir 4 has $\sigma_1 = \sigma_V > \sigma_2 = \sigma_{Hmax}$; (000°, 180°) > $\sigma_3 = \sigma_{Hmin}$ (090°, 270°; a normal stress regime). Figures 8.2 a_{BO} and a_{DITF} describes the most stable borehole orientation when drilling over the base salt (a) is at a 45° angle in the plane of σ_V and σ_{Hmin} (000°, 180°). The stress state over the diapir crest (b) has $\sigma_1 = \sigma_{Hmax}$ (090°, 270°) > $\sigma_2 = \sigma_{Hmin}$; (000°, 180°) > $\sigma_3 = \sigma_V$ (a reverse fault stress regime). Figures 8.2 b_{BO} and b_{DITF} are borehole stability diagrams showing the most stable drilling direction over the diapir crest. The most stable drilling direction is at a 35° angle in the plane of σ_V and σ_{Hmin} (000°, 180°). The stress state over the eastern diapir flank (c) has an inclined $\sigma_1 = \sigma_V$ (090°, 270°, dipping 45° east) > $\sigma_2 = \sigma_{Hmax}$; (000°, 180°) > $\sigma_3 = \sigma_{Hmin}$ (090°, 270°, dipping 45° east; an inclined normal fault stress regime). Figures 8.2 c_{BO} and c_{DITF} are wellbore stability diagrams showing the most stable drilling direction over the eastern flank of diapir 4. The most stable drilling directions are vertical and horizontal in the plane of σ_V and σ_{Hmin} (000°, 180°).

Figure 8.3 is a schematic representation of the active diapir 1; with a σ_1 perpendicular to the salt-sediment contact of the diapir (b, c) and the salt-sediment contact of the base (a). The most stable drilling directions for each stress orientation are represented in terms of borehole breakout stability diagrams (Figures 8.3 a_{BO}, b_{BO}, c_{BO}); and DITF stability diagrams (Figures 8.3 a_{DITF}, b_{DITF}, c_{DITF}). The stress state over the base salt (a) has $\sigma_1 = \sigma_v > \sigma_2 = \sigma_{Hmax}$; (000°, 180°) > $\sigma_3 = \sigma_{Hmin}$ (090°, 270°). Figures 8.3 a_{BO} and a_{DITF} describe the most stable borehole orientation when drilling over the base salt (a). The most stable drilling direction is at a 45° angle in the plane of σ_V and σ_{Hmin} (000°, 180°). The stress state over the eastern diapir flank (b) has an inclined $\sigma_1 = \sigma_V$ (090°, 270°, dipping 45° east) > $\sigma_2 = \sigma_{Hmax}$ (000°, 180°) > $\sigma_3 = \sigma_{Hmin}$ (090°, 270°, dipping 45° west). Figures 8.3 b_{BO} and b_{DITF} are wellbore stability diagrams showing the most stable drilling direction over the western diapir flank. The most stable drilling directions are vertical and horizontal in the plane of σ_V and σ_{Hmin} (000°, 180°). The stress state over the diapir crest (c) has $\sigma_1 = \sigma_V > \sigma_2 = \sigma_{Hmax}$ (000°, 180°) > $\sigma_3 = \sigma_{Hmin}$ (90°, 270°). Figures 8.3 c_{BO} and c_{DITF} are borehole stability diagrams showing the most stable drilling direction over the diapir crest. The most stable drilling direction is at a 45° angle in the plane of σ_V and σ_{Hmin} (000°, 180°).

The most stable drilling direction in the regional extensional setting at the delta top of the Gulf of Mexico, with a stress state of $\sigma_V > \sigma_{Hmax} > \sigma_{Hmin}$ (normal stress regime), is at a dip of 45° in the plane of σ_V and σ_{Hmin}. However, Wells drilled adjacent to salt diapirs that are within the proximity of the stress deflections are still most stable when oriented parallel to the σ_1-σ_3 plane at an angle that subjects the wells to the least stress anisotropy. Thus, wells must be planned with respect to the deflected stress field and not the regional stress field (Figure 8.2, 8.3). The diapir type must be considered as active salt diapirs of the Gulf of Mexico, there are stiffer than the surrounding rocks due to the overpressure within the salt (Zhang, 1994), deflect σ_1 perpendicular to the salt-sediment contact (Figure 6.8). Reactive salt diapirs of the Gulf of Mexico act as bodies softer than the surrounding sediments, deflecting σ_1 parallel to the salt-sediment contact (Figure 6.15). The proximity to the salt-sediment contact of the diapirs influences the deflection of σ_1. Therefore, wells drilled near salt diapirs may not be stable when drilled in one orientation; wells may instead have to follow a nonlinear path determined by numerical models such as those in this research.

9.0 Acknowledgements

As the author I would like to thank the main research supervisor Dr. Rosalind King; the two secondary supervisors Dr. Guillaume Backe and Dr. Adrian Tuitt; Western Geoco for providing the Ship Shoal three-dimensional seismic cube; JR's petroleum research for academic license of swift borehole stability modelling, and; SMT for academic license for Kingdom ™.

10.0 References

Aadnoy, B.S., and Bell, J.S., 1998, Classification of Drilling-Induced Fractures and Their Relationship to In-Situ Stress Directions: Log Analyst, v. 39, p. 27 - 42.

Addis, M.A., Barton, N.R., Bandis, S.C., and Henry, J.P., 1990, Laboratory Studies on the Stability of Vertical and Deviated Boreholes: Society of Petroleum Engineers Inc.

Alsouki, M., Riahi, M.A., and Yassaghi, A., 2011, Seismic imaging of sub-circular salt-related structures: evidence for passive diapirism in the Straits of Hormuz, Persian Gulf: Petroleum Geoscience, v. 17, p. 101 - 107.

Babley, M.E., 1985, Practical Seismic Interpretation: Boston, MA, IHRDC Press.

Bally, A.W., 1981, Thoughts on the tectonics of folded belts: The Geological Society of London, London, p. 13 - 32.

Barton, C.A., Castillo, D.A., Moos, D., Peska, P., and Zoback, M.D., 1998, Characterising the full stress tensor based on observations of drilling-induced wellbore failures in vertical and inclined boreholes leading to improved wellbore stability and permeability prediction. : Australian Petroleum Production and Exploration Association Journal, p. 467-487.

Bell, J.S., 1996a, Petro Geoscience 1. In Situ Stresses in Sedimentary Rocks (Part 1): Measurement Techniques: Geological Survey of Canada, v. 23.

Bell, J.S., 1996b, Petro Geoscience 2. In Situ Stresses in Sedimentary Rocks (Part 2): Measurement Techniques: Geological Survey of Canada, v. 23.

Bell, J.S., and Gough, D.I., 1979, Northeast-southwest compressive stress in Alberta: Evidence from oil wells: 45, p. 475-482.

Bottero, A., Negre, R., Pastor, J., and Turgeman, S., 1980, Finite Element Method and Limit Analysis Theory for Soil Mechanics Problems, Computer Methods in Applied Mechanics and Engineering, Volume 22, North-Holland Publishing Company, p. 131 - 149.

Brudy, M., and Zoback, M.D., 1999, Drilling-induced tensile wall-fractures: implications for determination of in-situ stress orientation and magnitude: International Journal of Rock Mechanics and Mining Sciences, v. 36, p. 191-215.

Byerlee, J., 1978, Friction of Rocks: Pure and Applied Geophysics, v. 116, p. 615-626.

Carmichael, R.S., 1984, Handbook of physical properties of rocks, Volume III: Boca Raton, CRC Press.

Coffeen, J.A., 1986, Seismic Exploration Fundamentals: Seismic techniques for finding oil.

Cramez, C., 2006, Short Course on Salt Tectonics, Geoscience, Energy and Environment - Courses and Lectures, Biblioteca Digital.

Currie, J.B., 1956, Role of concurrent deposition and deformation of sediments in development of salt-dome graben structures: American Association of Petroleum Geologists Bulletin, v. 40, p. 1 - 16.

Dutta, N.C., 1997, Pressure prediction from seismic data- implications for seal distribution and hydrocarbon exploration and exploitation in the deepwater Gulf Of Mexico, *in* Koestler, P.M.-P.a.A.G., ed., Hydrocarbon Seals: Importance for Exploration and Production Volume 7: Elsevier, Singapore, Norwegian Petroleum Society, p. 187 - 199.

Engelder, T., and Marshak, S., 1988, Analysis of Data from Rock-Deformation Experiments, Basic Methods of Structural Geology, p. 193 - 212.

Engelder, T., and Marshak, S., 1998, Analysis of data from rock-deforming experiments., *in* Marshak, S., and Mitra, G., eds., Basic Methods of Structural Geology: Prentice Hall, New Jersey.

Fails, T.G., 1990, The Northern Gulf Coast Basin: a classic petroleum province: Geological Society, London, Special Publications, v. 50, p. 221-248.

Fairchild, L.H., and Nelson, T.H., 1989, Emplacement and evolution of salt sills in northern Gulf of Mexico, AAPG Search and Discovery Article, Volume 91022.

Fiduk, J.C., Weimer, P., Trudgill, B.D., Rowan, M.G., Gale, P.E., Phair, R.L., Korn, B.E., Roberts, G.E., Gafford, E.T., Lowe, R.S., and Queffelec, T.A., 1999, The Perdido Fold Belt, Northwestern Deep Gulf of Mexico, Part 2: Seismic Stratigraphy and Petroleum Systems: AAPG Bulletin, v. 83, p. 578–612.

Finkbeiner, T., Zoback, M., Flemings, P., and Stump, B., 2001, Stress, pore pressure, and dynamically constrained hydrocarbon columns in the South Eugene Island 330 field, northern Gulf of Mexico.: American Association of Petroleum Geologists Bulletin, v. 85, p. 1007-1031.

Fredrich, J.T., Fossum, A.F., and Hickman, R.J., 2007, Mineralogy of deepwater Gulf of Mexico salt formations and implications for constitutive behavior: Journal of Petroleum Science and Engineering, v. 57, p. 354–374.

Ge, H., Jackson, M.P.A., and Vendeville, B.C., 1997, Kinematics and Dynamics of Salt Tectonics Driven by Progradation: AAPG Bulletin, v. 81, p. 398–423.

Gudmundsson, A., 2004, Effects of Young's modulus on fault displacement: Comptes rendus. Géoscience, v. 336, p. 85 - 92.

Hamilton, E.L., 1976, Variations of Density and Porosity with Depth in Deep-Sea Sediments: Journal of Sedimentary Petrology, v. 46, p. 280 - 300.

Handin, J., and Hager Jr, R.X., 1963, Experimental Deformation of Sedimentary Rocks Under Confining Pressure: Pore Pressure Tests: AAPG Bulletin, v. 47.

Hansen, F., 1977, Evaluation Of An Inelastic Law For Salt Creep, The 18th U.S. Symposium on Rock Mechanics (USRMS), American Rock Mechanics Association.

Heffer, K.J., and Lean, J.C., 1993, Earth Stress Orientation – A control on, and guide to, flooding directionality in a majority of reservoirs: In: Linville, W. (Ed.). Reservoir Characterisation III, Pennwell Becks, Tulsa,, p. 799-822.

Hillis, R., 2000, Variations of Density and Porosity with Depth in Deep sea sediments: Exploration Geophysics, v. 31, p. 448 - 454.

Hillis, R.R., and Williams, A.F., 1993, The stress field of the North West Shelf and wellbore stability: Australian Petroleum Production and Exploration Association Journal, p. 373 - 385.

Hubbert, M.K., and Rubey, W., 1959, Role of fluid pressure in mechanics of overthrust faulting,Pts.1 and 2: Geological Society of America Bulletin, v. 70.

Hudec, M.R., and Jackson, M.P.A., 2007, Terra infirma: Understanding salt tectonics: Earth-Science Reviews, v. 82, p. 1–28.

Hudec, M.R., Jackson, M.P.A., and Schultz-Ela, D.D., 2009, The paradox of minibasin subsidence into salt: Clues to the evolution of crustal basins: Geological Society of America Bulletin, v. 121, p. 201 - 221.

Jackson, M.P.A., Hudec, M.R., Jennette, D.C., and Kilby, R.E., 2008, Evolution of the Cretaceous Astrid thrust belt in the ultradeep-water Lower Congo Basin, Gabon: AAPG Bulletin, v. 92, p. 487–511.

Jackson, M.P.A., and Talbot, C.J., 1986, External shapes, strain rates, and dynamics of salt structures: Geological Society of America Bulletin, v. 97, p. 305 - 323.

Jackson, M.P.A., Venderville, B.C., and Schulz-Ela, D.D., 1994, Salt-related structures in the Gulf of Mexico: A field guide for geophysicists: Bureau of Economic Geology.

Jenyon, M.K., and Fitch, A.A., 1985, Seismic Reflection Interpretation.

King, R., Backé, G., Morley, C.K., Hillis, R., and Tingay, M., 2010a, Balancing deformation in NW Borneo: Quantifying plate-scale vs. gravitational tectonics in a delta and deepwater fold-thrust belt system: Marine and Petroleum Geology, v. 27.

King, R., Backé, G., Tingay, M., Hillis, R., and Mildren, S., in press, Stress deflections around salt diapirs in the Gulf of Mexico Delta Systems, U.S.A.

King, R., Hillis, R.R., Tingay, M.R.P., and Morley, C.K., 2010b, Present-day stress and neotectonic provinces of the Baram Delta and deep-water thrust belt: Journal of the Geological Society, v. 166, p. 197 - 200.

Kirsch, V., 1898, Die Theorie der Elastizität und die Beddürfnisse der Festigkeitslehre: Zeitschrift des Vereines Deutscher Ingenieure, v. 29.

Kleyn, A.H., 1983, Seismic Reflection Interpretation: London and New York and New York, N.Y., USA, Applied Science Publishers.

Liang, W., Yang, C., Zhao, Y., Dusseault, M.B., and Liu, J., 2006, Experimental investigation of mechanical properties of bedded salt rock: International Journal of Rock Mechanics & Mining Sciences, v. 44.

Luja´na, M., Stortib, F., Balany, J., Crespo-Blanca, A., and Rossetti, F., 2003, Role of de´collement material with different rheological properties in the structure of the Aljibe thrust imbricate (Flysch Trough, Gibraltar Arc): an analogue modelling approach: Journal of Structural Geology, v. 25, p. 867 - 881.

McLellan, P.J., and Wang, Y., 1994, Predicting the effects of pore pressure penetration on the extent of wellbore instability: Application of a versatile poro-elastoplastic model, Rock Mechanics in Petroleum Engineering: Delft, Netherlands, Society of Petroleum Engineers.

Mingchen, J., Yongjun, C., and Xuguang, G., 2009, Application of Seismic Sedimentology Method to Lithologic Trap Identification of Shinan Area in Junggar Basin, Xinjiang Oilfield Company, Petrochina: Karamay, Xinjiang 834000, China.

Morley, C.K., King, R., Hillis, R., Tingay, M., and Backe, G., 2010, Deepwater fold and thrust belt classification, tectonics, structure and hydrocarbon prospectivity: A review: Earth-Science Reviews, v. 104, p. 41 - 91.

Nelson, E.J., Hillis, R.R., Meyer, J.J., Mildren, S.D., Van Nispen, D., and Briner, A., 2005, The reservoir stress path and its implications for water flooding, Champion Southeast Field, Brunei., Proceedings of Alaska Rocks the 40th U.S. Symposium on Rock Mechanics, American Rock Mechanics Association.

Ord, A., Vardoulakis, I., and Kajewski, R., 1991, Shear Band Formation in Gosford Sandstone: International Journal of Rock Mechanics & Mining Sciences, v. 28, p. 397 - 409.

Park, B.Y., Herrick, C.G., Lee, M.Y., and Ehgartner, B.L., 2008, Numerical Simulation Evaluating the Structural Stability of the Strategic Petroleum Reserve (SPR) in Bayou Choctaw Salt Dome, USA: American Rock Mechanics Association.

Peel, F.J., Travis, C.J., and Hossack, J.R., 1995, Genetic structural provinces and salt tectonics of the Cenozoic offshore U.S. Gulf of Mexico: a preliminary analysis, Salt tectonics: a global perspective. American Association of Petroleum Geologists Memoir, Volume 65, p. 153 - 175.

Peška, P., and Zoback, M.D., 1995, Compressive and tensile failure of inclined well bores and determination of in situ stress and rock strength: Journal of Geophysical Research, v. 100, p. 12,791-12,811.

Rath, J.S., Argüello, J.G., Stone, C.M., and Sobolik, S.R., 2009, Evaluating the Present in-situ Stress-State for the Richton, MS, Strategic Petroleum Reserve Site using Geomechanical Analyses: American Rock Mechanics Association.

Rice, J., 1992, Fault Stress States, Pore Pressure Distributions, and the Weakness of the San Andreas Fault, *in* Geophysics, I., ed., Fault Mechanics and Transport Properties of Rocks, Volume 51, p. 475 - 503.

Rowan, M.G., 1997, Three-dimensional geometry and evolution of a segmented detachment fold, Mississippi Fan foldbelt, Gulf of Mexico: Journal of Structural Geology, v. 19, p. 463 - 480.

Rowan, M.G., and Venderville, B.C., 2006, Foldbelts with early salt withdrawal and diapirism: Physical model and examples from the northern Gulf of Mexico and the Flinders Ranges, Australia: Marine and Petroleum Geology, v. 23, p. 871 - 891.

Schultz-Ela, D.D., Jackson, M.P.A., and Vendeville, B.C., 1993, Mechanics of active salt diapirism: Tecfonophysics, v. 228, p. 275 - 312.

Sharp, D.H., 1984, An overview of Rayleigh-Taylor instability: Physica D: Nonlinear Phenomena, v. 12, p. 3 - 10.

Shen, X., 2010, Subsidence Prediction and Casting Integrity With Respect to Pore-Pressure Depletion With 3-D Finite-Element Method, SPE Latin American and Caribbean Petroleum Engineering Confrence: Lima, Peru, Society of Petroleum Engineers.

Stover, S.C., Ge, S., Weimer, P., and McBride, B.C., 2001, The effects of salt evolution, structural development, and fault propagation on Late Mesozoic–Cenozoic oil migration: A two-dimensional fluid-flow study along a megaregional profile in the northern Gulf of Mexico Basin: AAPG Bulletin, v. 85, p. 1945 –1966.

Tingay, M.R.P., Hillis, R.R., Morley, C.K., King, R.C., Swarbrick, R.E., and Damit, A.R., 2009, Present-day stress and neotectonics of Brunei: Implications for petroleum exploration and production: American Association of Petroleum Geologists Bulletin, v. 93, p. 75 - 100.

Trevino, R.H., and Vendeville, B.C., 2008, Origin of coast-perpendicular extensional faults, western Gulf of Mexico: The relationship between an early-stage ridge and a late-stage fault: AAPG Bulletin, v. 92, p. 951–964.

Trudgill, B.D., Rowan, M.G., Fiduk, J.C., Weimer, P., Gale, P.E., Korn, B.E., Phair, R.L., Gafford, E.T., Roberts, G.E., and Dobbs, S.W., 1999, The Perdido Fold Belt, Northwestern Deep Gulf of Mexico, Part 1: Structural Geometry, Evolution and Regional Implications: AAPG Bulletin, v. 83, p. 88 - 113.

Tuitt, A., King, R., Hergert, T., Tingay, M., and Hillis, R., in press, Modelling of sediment wedge movement along low-angle detachments using ABAQUS^{TM}.

Venderville, B.C., and Jackson, M.P.A., 1992b, The fall of diapirs during thin-skinned extension: Marine and Petroleum Geology, v. 9, p. 331 - 354.

Vendeville, B.C., and Jackson, M.P.A., 1992a, The rise of diapirs during thin-skinned extension: Marine and Petroleum Geology, v. 9, p. 354 - 371.

Worrall, D.M., and Snelson, S., 1989, Evolution of the northern Gulf of Mexico, with emphasis on Cenozoic growth faulting and the role of salt: Geological Society of America Centennial Special Volume, The Geology of North America, p. 97-138.

Wu, S., Bally, A.W., and Cramez, C., 1990, AIIochthonous salt, structure and stratigraphy of the north-eastern Gulf of Mexico. Part 2: Structure: Marine and Petroleum Geology, v. 7, p. 334 – 370.

Yassir, N.A., and Zerwer, A., 1997, Stress regimes in the Gulf Coast, offshore Louisiana: data from well-bore breakout analysis: American Association of Petroleum Geologists Bulletin, v. 81, p. 293 - 307.

Zhang, Y., Dusseault, M.B., and Yassir, N.A., 1994, Effects of rock anisotropy and heterogeneity on stress distributions at selected sites in North America: Engineering Geology, v. 37, p. 181 - 197.

Zoback, M., Moos, D., Mastin, L., and Anderson, R.N., 1985, Wellbore breakouts and in-situ stress: Journal of Geophysical Research, v. 90, p. 5523 - 5530.

11.0 Table Captions

Table 5.1

Seismic velocity model of the deltaic sediments from the delta top of the Gulf of Mexico.

Table 5.2

The density, Young’s Modulus and Poisson’s Ratio used for the salt and sediment parts of each of the initial models.

Table 5.3

Density, Young’s Modulus and Poisson’s Ratio used for the salt and sediment parts of each of the models of interpreted diapirs.

Table 5.4

Permeability, void ratio and pore fluid pressure used for the salt and sediment parts of each of the initial models.

Table 5.5

Permeability, void ratio and pore fluid pressure used for the salt and sediment parts of each of the models of interpreted diapirs.

Table 5.6

The Drucker-Prager yield criterion values input into all models with Drucker-Prager deformation.

12.0 Figure Captions

Figure 2.1

The Gulf of Mexico is located offshore from the southern United States of America, the east of Mexico and the west of Cuba. A) Bathymetric map of the Gulf of Mexico. Outlined is the map area of Figure 2.8. B) The stratigraphy of the Gulf of Mexico is dominated by several thick Upper Jurassic to Pleistocene delta systems that overlay the Louann Salt (Peel et al., 1995; Trudgill et al., 1999; Figure from King et al., in press).

Figure 2.2

A schematic representation of a variety of structural petroleum traps associated with salt dome in the Gulf of Mexico (REF).

Figure 2.3

The mechanics of salt movement as described by Jackson and Talbot (1986): A) Bouyancy halokinesis; B) Differential loading halokinesis; C) Gravity spreading halokinesis; D) Thermal convective halokinesis.

Figure 2.4

A) Schematic forward model of salt tectonics during regional extension, constructed using Geosec-2D (modified from Hudec and Jackson, 2007). Thin salt layers are dominated by normal growth faults and low-amplitude salt structures such as salt rollers. Thicker salt layers will form reactive diapirs and with continued extension, subsequent diapir fall. B) Schematic forward model of salt tectonics during regional shortening, constructed using Geosec-2D (modified from Hudec and Jackson, 2007). The salt functions mainly as a detachment for large scale thrust faults, box fold anticlines and salt cored anticlines.

Figure 2.5

Diapir piercement and evolution during regional extension: A) Pre-extension; B) Reactive diapirism; C) Active diapirism; D) Passive diapirism; and, E) Allocthonous sheet advance. Diapirs do not necessarily progress through all of these stages. The maturity of a given structure depends on availability of salt, total amount of extension, and relative rates of extension and sedimentation (Hudec and Jackson, 2007; modified from Vendeville and Jackson, 1992a).

Figure 2.6

Schematic diagram of a delta deep-water fold thrust belt illustrating the linked extension and compression. The delta top exhibits normal listric growth faults reflecting a margin-parallel maximum horizontal stress and the delta toe (or deepwater fold-thrust belts) exhibits imbricate thrust sheets and associated fault-propagation folds reflecting a margin-normal maximum horizontal stress orientation (from King & Backé, 2010).

Figure 2.7

A Vertical borehole cross-section of a well drilled into an extensional stress regime. Borehole breakouts will develop perpendicular to the orientation of maximum horizontal stress. Drilling-induced tensile fractures will develop parallel to the maximum horizontal stress (REF).

Figure 2.8

Map illustrating the maximum horizontal stress orientations across the Gulf of Mexico (Black arrows: Yassir and Zerwer, 1997; White arrows: King et al., in press). The mean regional maximum horizontal stress orientation is margin-parallel, consistent with the idealised model of a delta—deepwater fold-thrust belt (Figure 2.6). Deflection of maximum horizontal stress orientations from margin-parallel occurs where salt diapirs pierce the deltaic sediments at the shelf edge break (REF). The maximum horizontal stress orientations align parallel to the interface between salt and sediment shown in areas 1 and 2 (insets; King et al., in press). The Ship Shoal seismic survey area used in this research is highlighted in green.

Figure 2.9

A schematic plan view diagram that shows how the maximum principal stress is deflected by contrasts in geomechanical properties. A) A stiff salt body within softer sediments, the orientation of maximum horizontal stress is deflected normal to the salt-sediment contact. B) A soft salt body within stiffer sediments, the orientation of maximum horizontal stress is deflected parallel to the salt-sediment contact (Bell, 1996a).

Figure 3.1

Seismic reflection data from the Ship Shoal survey in the Gulf of Mexico. The reflections are interpreted as coming from the tops of geologic formations when there is a velocity contrast between adjacent units.

Figure 3.2

Seismic reflection data of salt diapirs in the Gulf of Mexico. The salt dome is represented by the area of low amplitude, chaotic and unstructured reflections; extending up from the bottom of the section.

Figure 3.3

A time slice at 1.0s of the seismic reflection data from the Ship Shoal survey. Amplitude is represented in a grey colour scale. Salt is represented by areas of low amplitude, chaotic and unstructured reflections or ‘blank spots’.

Figure 3.4

A) Seismic reflection data of a salt diapir in the Ship Shoal survey area. The salt-sediment horizon can only be followed part way across the section. B) The gaps in the reflector can be continued because the reflectors immediately above are continuous and parallel, and maintain equal spacing over the gap.

Figure 3.5

Seismic reflection data of salt diapirs in the Gulf of Mexico. The data has had a 45° phase rotaion applied. This effectively makes reflection events correspond with strata rather than with its top or bottom interface; effectively representing seismic reflection events in a lithostratigraphic sense (REF).

Figure 3.6

Salt diapirs from the Gulf of Mexico with an opacity filter applied. A) The opacity filter (green line), filters out attribute amplitudes. B) the result is an image of the seismic data with all of the low amplitude reflections within the salt filtered out leaving a dark spot/area that represents the geometry of the salt diapir. This is a more accurate image than the standard amplitude data.

Figure 3.7

A normal fault visualised in Kingdom™ VuPak extension using an oblique view. Fault plane is highlighted red. Red arrows indicate fault throw, interpreted from displacement of the seismic stratigraphy.

Figure 3.8

Seismic reflection data from the Gulf of Mexico. A surface or near-surface feature (e.g. shallow gas) has produced a misleading anomaly that is masking deeper reflections.

Figure 3.9

Seismic reflection data of a salt diapir from the Gulf of Mexico. The arrow identifies an internal reflection within the salt. Internal reflections within the salt may result from: a heterogeneous salt composition, a salt body deposited as multi-stage flow events or it may represent the base of the salt body.

Figure 3.10

A) Schematic representation of a reactive diapir. The fault blocks are relatively well preserved during the reactive stage (REF). B) Example of a reactive diapir from the Gulf of Mexico, in seismic section (Modified from Rowan et al., 1999).

Figure 3.11

A) A schematic representation of an active diapir with a double flapped arching roof (Modified from Schultz-Ela et al., 1993) B) Example of an active diapir with a double flapped arching roof from seismic reflection data (REF). C) A schematic representation of asymmetric active diapirism with a single flapped roof (Modified from Schultz-Ela et al.,

1993) D) Interpretation of the salt diapir (REF) (B), the sedimentary overburden deformed to an antiform shape above then diapir crest, normal extensional faults radiate from the diapir crest.

Figure 3.12

A) A schematic representation of a passive diapir. The diapir has breached the surface. Surrounding sediments approach the diapir horizontally (Modified form Hudec and Jackson, 2007). B) A schematic representation of a buried passive diapir (Modified form Hudec and Jackson, 2007). C) Example of a buried passive diapir from the Gulf of Mexico (Modified from Hale et al., 1992).

Figure 3.13

The evolution of a salt diapir from a salt mound to a salt dome. As the mound matures into a salt dome, salt is withdrawn into the growing diapir which leads to a collapse of the flanking sequence and thinning towards the original pillow. The salt withdrawal from the diapir flanks is tracked from 1 to 5 (Modified from Cramez, 2006).

Figure 3.14

Turtle-back structures are strata mounded between salt diapirs, having a flat base and rounded crest created through the inversion of a structural low to a local high (Modified from Cramez, 2006).

Figure 4.1

Map of top Louann Salt interpreted from the Ship Shoal 3D seismic survey in the Gulf of Mexico (depth in TWT). Salt diapirs are labelled 1-6.

Figure 4.2

A perspective view from the North-East of the top salt depth (TWT) imaged in 3D using Kingdom^{TM} software VuPak extension.

Figure 4.3

A) Representative seismic reflection data section of diapir 1. B) Seismic section of diapir 1 with a 45° phase rotation filter applied, interpreted for: top salt-sediment contact (green), deformation of the overlying sedeiments (blue) and local faults (light yellow). Note the clarity of stratigraphic units adjacent to the salt diapir with 45° phase rotation applied.

Figure 4.4

A) Representative seismic reflection data section of diapir 2. B) Seismic section of diapir 2 with a 45° phase rotation filter applied, interpreted for: top salt-sediment contact (green), deformation of the overlying sediments (blue) and local faults (light pink). Note the clarity of stratigraphic units adjacent to the salt diapir with 45° phase rotation applied.

Figure 4.5

A) Representative seismic reflection data section of diapir 3. B) Seismic section of diapir 3 with a 45° phase rotation filter applied, interpreted for: top salt-sediment contact (green), deformation of the overlying sedeiments (blue) and local faults (light pink). Note the clarity of stratigraphic units adjacent to the salt diapir with 45° phase rotation applied.

Figure 4.6

A) Representative seismic reflection data section of diapir 6. B) Seismic section of diapir 6 with a 45° phase rotation filter applied, interpreted for: top salt-sediment contact (green), deformation of the overlying sedeiments (blue) and local faults (light brown). Note the clarity of stratigraphic units adjacent to the salt diapir with 45° phase rotation applied.

Figure 4.7

A) Representative seismic reflection data section of diapir 4. B) Seismic section of diapir 4 with a 45° phase rotation filter applied, interpreted for: top salt-sediment contact (green), deformation of the overlying sedeiments (blue) and local faults (dark green). Note the clarity of stratigraphic units adjacent to the salt diapir with 45° phase rotation applied.

Figure 4.8

A) Representative seismic reflection data section of diapir 1. B) Seismic section of diapir 5 with a 45° phase rotation filter applied, interpreted for: top salt-sediment contact (green), deformation of the overlying sedeiments (blue) and local faults (white). Note the clarity of stratigraphic units adjacent to the salt diapir with 45° phase rotation applied.

Figure 4.9

Currie’s (1956) model of active diapirism forcing extension above the diapir crest. The extension produced by the normal faulting is higher than the apparent shortening produced by the piston uplift.

Figure 4.10

A time slice section of the seismic reflection of diapir 1 area at 1 second. Faults are highlighted in red. The extension above the diapir crests creates radial normal-faults, which extend the overburden in order to fill the space created by salt withdrawal from the diapir flanks.

Figure 4.11

A depth section with a 3 times vertical exaggeration from the Sigsbee Escarpment in the Mississippi Fan Delta of the Gulf of Mexico. A large allochthonous salt sheet is present at a depth of 3-5km. The Louann Salt layer is at depths of 7.5 – 10km.

Figure 5.1

Model dimensions. The left and right boundaries of each model are each 100km away from the central diapir. The model is 20km deep so that the base is approximately ~15km deeper than the sediments (x_D = the width of the diapir, y_D = the height of the diapir).

Figure 5.2

Set 1: The dimensions of the initial models. A) Model 2; B) Model 3; C) Model 4; D) Models 5 – 13 (x_D = the width of the diapir, y_D = the height of the diapir).

Figure 5.3

Set 2: The dimensions of the interpreted diapir models. Active diapirs: A) Diapir 1; B) Diapir 2; C) Diapir 3; D) Diapir 6. Reactive Diapirs: E) Diapir 4; F) Diapir 4 (x_D = the width of the diapir, y_D = the height of the diapir).

Figure 5.4

The top salt in the study area did not reach depths of 7 seconds (TWT) and the influence on the depth conversion by the water depth in the sections was negligible. Therefore, the sections could be simply traced then stretched according to equation 1. A) Interpreted seismic section of diapir 1 with a 45° phase rotation. B) The salt-sediment contact is traced. C) The Salt sediment contact is stretched to 1:1 vertical exaggerated dimensions.

Figure 5.5

The density-depth pairs of Gulf of Mexico sediments used for the density gradient of the sediment part. Well data was compiled by Fairchild and Nelson (1989)

Figure 5.6

Assembly of the model diapir 1. A) The salt (below) and sediments (above) parts. B) The two parts are assembled with a perfect fit.

Figure 5.7

The distributed gravity load of $-9.81 ms^{-2}$ was applied the model Diapir 1. Black arrows indicate the direction of the load.

Figure 5.8

The boundary conditions of the model diapir 1. The vertical sides of the model were completely restricted in their ability to rotate and move laterally. The base of the model was completely restricted in its ability to rotate and move vertically. The top surface was allowed to deform freely.

Figure 5.9

A) The mesh applied to the model diapir 1. The close up view (B) is outlined in black. B) Close up view of the mesh size and distribution surrounding the diapir of the model diapir 1. The salt-sediment contact is delineated by the orange line.

Figure 5.10

Mohr circle diagrams illustrating the effects of increasing pore fluid pressure (overpressure) and decreasing pore fluid pressure (depletion) on rock failure, assuming that the total normal stress is not affected by changes in pore fluid pressure (Modified from Hillis, 2000).

Figure 5.11

A gradient of 12MPa/km was used for the pore fluid pressure of the sediments. The gradient falls within the envelope created by the hydrostatic gradient (9.81MPa/km) and the lithostatic gradient (24.5MPa/km; Dutta, 1997).

Figure 5.12

The shear stress vs. shear strain graph of the failure point for the sandstone used to represent the sediments of the Gulf of Mexico (Ord et al., 1991). The Drucker–Prager yield criterion refers to the point at which deformation changes from elastic to plastic.

Figure 6.1

Stress orientations and magnitudes were visualised as tensors. The black symbols represent σ_1. The magnitude is proportional to the length of the tensor. White lines outline the model elements, the intersections are nodes.

Figure 6.2

A) Stress orientation and magnitude results for model 2. The orientation of σ_1 (Black) within the sediments is deflected from vertical to be parallel to the salt-sediment contact of the salt diapir.

Figure 6.3

A) Stress orientation and magnitude results for model 4. The orientation of σ_1 (Black) within the sediments is deflected from vertical to be parallel to the salt-sediment contact of the salt diapir. B) Close up view of the stress orientation and magnitude results of the salt-sediments contact of model 4's diapir crest.

Figure 6.4

A) Stress orientation and magnitude results for the tall diapir of model 5. The orientation of σ_1 (Black) within the sediments is deflected from vertical to be parallel to the salt-sediment contact of the salt diapir. B) Close up view of the stress orientation and magnitude results of the salt-sediments contact of tall diapir's crest. C) Stress orientation and magnitude results for the deep diapir of model 5. The orientation of σ_1 (Black) within the sediments is deflected from vertical to be parallel to the salt-sediment contact of the salt diapir. D) Close up view of the stress orientation and magnitude results of the salt-sediments contact of the deep diapir's crest.

Figure 6.5

A) Stress orientation and magnitude results for the tall diapir of model 13. The orientation of σ_1 (Black) within the sediments is deflected from vertical to be parallel to the salt-sediment contact of the salt diapir. B) Close up view of the stress orientation and magnitude results of the salt-sediments contact of tall diapir’s crest. C) Stress orientation and magnitude results for the deep diapir of model 13. The orientation of σ_1 (Black) within the sediments is deflected from vertical to be parallel to the salt-sediment contact of the salt diapir. D) Close up view of the stress orientation and magnitude results of the salt-sediments contact of the deep diapir’s crest.

Figure 6.6

A) Colour contour representation of the pore fluid pressure results for the model diapir 1. A pressure gradient of 10MPa/km was given to the salt part of active diapir models. The pressure decreases with depth so that it can be contained within the rigid boundary conditions. B) Close up of the pressurised salt within the diapir.

Figure 6.7

Colour contour representation of the vertical displacement results for the model diapir 1. Uplift above the diapir crest is consistent with an active diapir.

Figure 6.8

A) The salt-sediment contact of diapir 1. The orientation of σ_1 within the sediments is deflected from vertical to be normal to the salt-sediment contact.

Figure 6.9

A) Stress orientation and magnitude results for the model diapir 1. The orientation of σ_1 (Black) within the sediments is deflected from vertical to be normal to the salt-sediment contact of the salt diapir. B) Close up view of the stress orientation and magnitude results of the salt-sediments contact of crest of diapir 1.

Figure 6.10

A) Stress orientation and magnitude results for the model diapir 2. The orientation of σ_1 (Black) within the sediments is deflected from vertical to be normal to the salt-sediment contact of the salt diapir. B) Close up view of the stress orientation and magnitude results of the salt-sediments contact of crest of diapir 2.

Figure 6.11

A) Stress orientation and magnitude results for the model diapirs 3 and 6. The orientation of σ_1 (Black) within the sediments is deflected from vertical to be normal to the salt-sediment contact of the salt diapirs. B) Close up view of the stress orientation and magnitude results of the salt-sediments contact of crest of diapirs 3.

Figure 6.12

A) Stress orientation and magnitude results for the model diapir 6. The orientation of σ_1 (Black) within the sediments is deflected from vertical to be normal to the salt-sediment contact of the salt diapir. B) Close up view of the stress orientation and magnitude results of the salt-sediments contact of crest of diapir 6.

Figure 6.13

A) Colour contour representation of the pore fluid pressure results for the model diapir 4. A pressure gradient, increasing with depth, of 12MPa/km was given to the sediments part of reactive diapir models. B) Close up of the overpressured sediments surrounding the salt diapir.

Figure 6.14

Colour contour section of the vertical displacement results for the model diapir 4. The overburden directly above the diaper crest is static consistent with reactive diapirism. The displacement over the diapir flanks is likely a response to the differing thickness of the sediment part either side of the diapir applying different loads.

Figure 6.15

A) The salt-sediment contact of diapir 4. The orientation of σ_1 within the sediments is deflected from vertical to be normal to the salt-sediment contact.

Figure 6.16

A) Stress orientation and magnitude results for the model diapir 4. The orientation of σ_1 (Black) within the sediments is deflected parallel to the salt-sediment contact of the salt diapir. B) Close up view of the stress orientation and magnitude results of the salt-sediments contact of crest of diapir 4.

Figure 6.17

A) Stress orientation and magnitude results for the model diapir 5. The orientation of σ_1 (Black) within the sediments is deflected from vertical to be parallel to the salt-sediment contact of the salt diapir flanks and edges of the crest. However, over the crest is a wide flat area that responds as if it was a base salt layer. B) Close up view of the stress orientation and magnitude results of the salt-sediments contact of the entire crest of diapir 5. C) Close up view of the stress orientation and magnitude results of the salt-sediments contact of the western side of the crest. D) Close up view of the stress orientation and magnitude results of the salt-sediments contact of the eastern side of the crest.

Figure 8.1

A) Borehole breakout stability diagram for an extensional stress regime with a maximum horizontal stress orientation of 090°. The most stable drilling directions are coloured blue and the least stable in red. B) Drilling induced tensile fracture stability diagram for an extensional stress regime with a σ_{Hmax} orientation of 090°. The most stable drilling directions are coloured blue and the least stable in red.

Figure 8.2

Schematic representation of diapir 4 and the stress regime: a. over the base salt layer; b. directly above the diapir crest; c. over the Eastern diapir flank. a_{BO}, b_{BO} and c_{BO} are borehole breakout stability diagrams; a_{DITF}, b_{DITF} and c_{DITF} are drilling induced tensile fracture diagrams; that correspond to the 3 stress regimes a,b and c. The most stable drilling direction is coloured blue; the least stable is coloured red.

Figure 8.3

Schematic representation of diapir 1 and the stress regime: a. over the base salt layer; b. directly above the diapir crest; c. over the Eastern diapir flank. a_{BO}, b_{BO} and c_{BO} are borehole breakout stability diagrams; a_{DITF}, b_{DITF} and c_{DITF} are drilling induced tensile fracture diagrams; that correspond to the 3 stress regimes a,b and c. The most stable drilling direction is coloured blue; the least stable is coloured red.

13.0 Tables

Stratigraphy	Time (s)	Internal velocity (m/s)
Sea water	0-0.073	1500
Deltaic sediments	0.073-7	2500
Deep sediments	7+	4500

Table 5.1

Model	Model part	Density kg/m3	Young's Modulus (GPa)	Poisson's Ratio
2,	Salt	2200	3.1	0.3
	Sediments	2400	34	0.3
3,	Salt	2200	3.1	0.3
	Sediments	2400	34	0.3
4,	Salt	2200	3.1	0.3
	Sediments	2400	34	0.3
5,	Salt	2200	3.1	0.3
	Sediments	2400	34	0.3
7,	Salt	2200	3.1	0.3
	Sediments	2400	34	0.3
9	Salt	2200	3.1	0.3
	Sediments	2400	34	0.3
10,	Salt	2200	3.1	0.3
	Sediments	$P = 1400 + 172d^{0.21}$	34	0.3
11,	Salt	2200	3.1	0.3
	Sediments	$P = 1400 + 172d^{0.21}$	34	0.3
13,	Salt	2200	3.1	0.3
	Sediments	$P = 1400 + 172d^{0.21}$	34	0.3

Table 5.2

Model	Model part	Density kg/m3	Young's Modulus (GPa)	Poisson's Ratio
diapir_1	Salt	2200	3.1	0.3
	Sediments	$P = 1400 + 172d^{0.21}$	34	0.3
diapir_2	Salt	2200	3.1	0.3
	Sediments	$P = 1400 + 172d^{0.21}$	34	0.3
diapir_3a6	Salt	2200	3.1	0.3
	Sediments	$P = 1400 + 172d^{0.21}$	34	0.3
diapir_4	Salt	2200	3.1	0.3
	Sediments	$P = 1400 + 172d^{0.21}$	34	0.3
diapir_5	Salt	2200	3.1	0.3
	Sediments	$P = 1400 + 172d^{0.21}$	34	0.3

Table 5.3

Model	Permeability (v, darcy)	Void ratio	Pore Fluid Pressure (Pa)
2,	1	0.5	-
	1	0.25	17000xd
3,	1	0.5	-
	1	0.25	Failed
4,	1	0.5	-
	1	0.25	17000xd
5,	1	0.5	-
	1	0.25	17000xd
7,	1	0.5	-
	1	0.25	Failed
9	1	0.5	-
	1	0.25	9800-22000xd
10,	1	0.5	-
	1	0.25	12000xd+w
11,	1	0.5	-
	1	0.25	12000xd+w
13,	1	0.5	-
	1	0.25	12000xd+w

Table 5.4

Model	Permeability (v, darcy)	Void ratio	Pore Fluid Pressure (Pa)
diapir_1	1	0.5	-
	1	0.25	12000xd+w
diapir_2	1	0.5	-
	1	0.25	12000xd+w
diapir_3a6	1	0.5	-
	1	0.25	12000xd+w
diapir_4	1	0.5	-
	1	0.25	12000xd+w
diapir_5	1	0.5	-
	1	0.25	12000xd+w

Table 5.5

Yield Stress	Strain
2.00E+08	0.00E+00
3.30E+08	0.007
4.30E+08	0.01
5.00E+08	0.011

Table 5.6

14.0 Figures

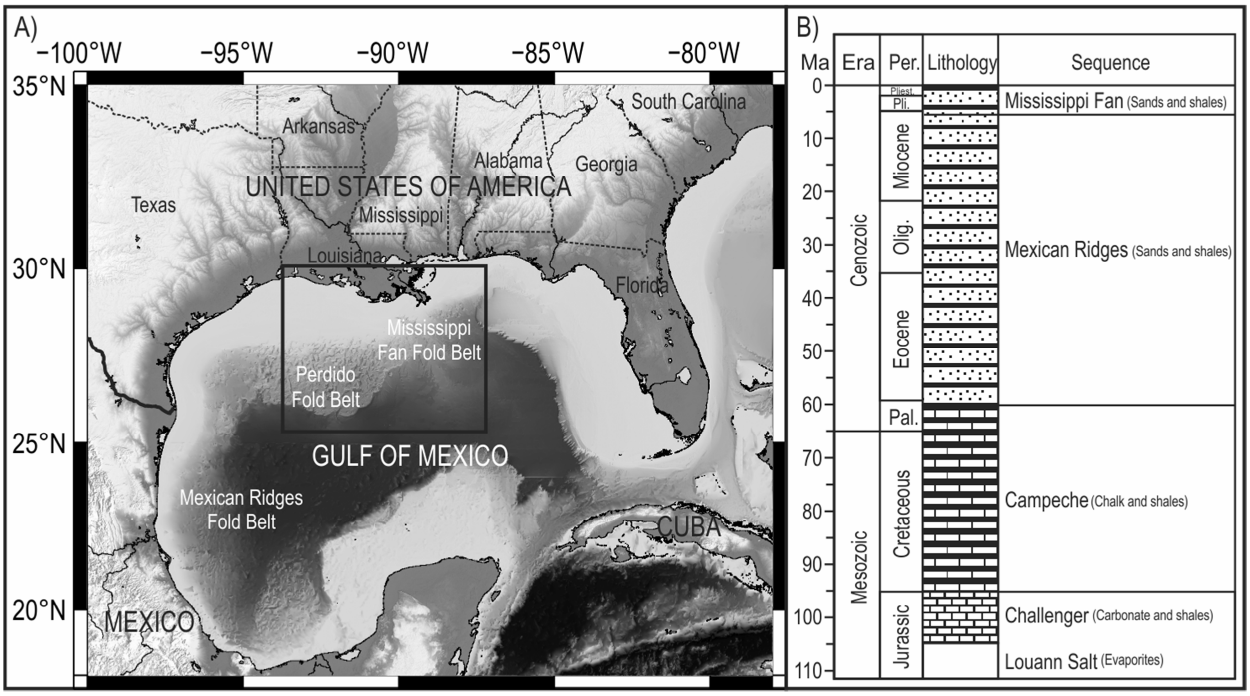

Figure 2.1

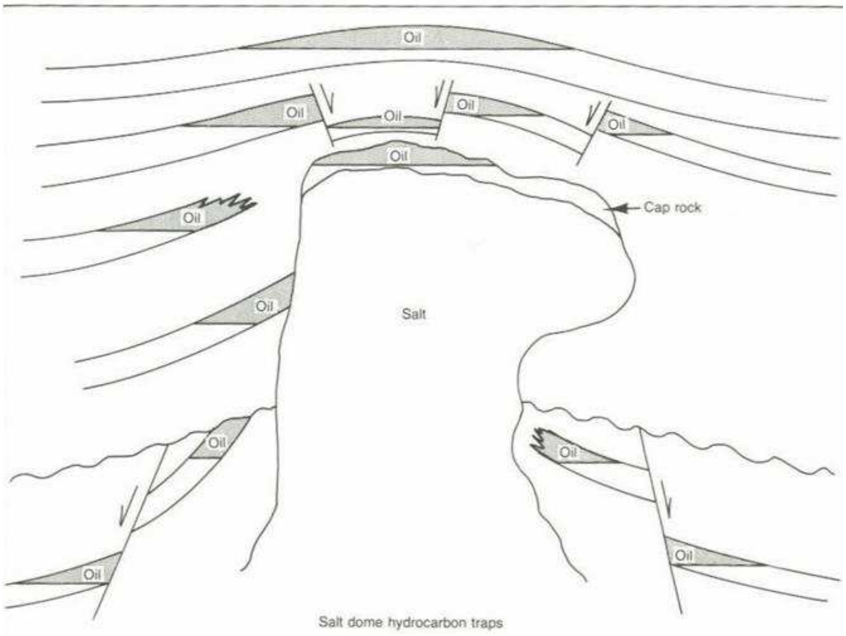

Figure 2.2

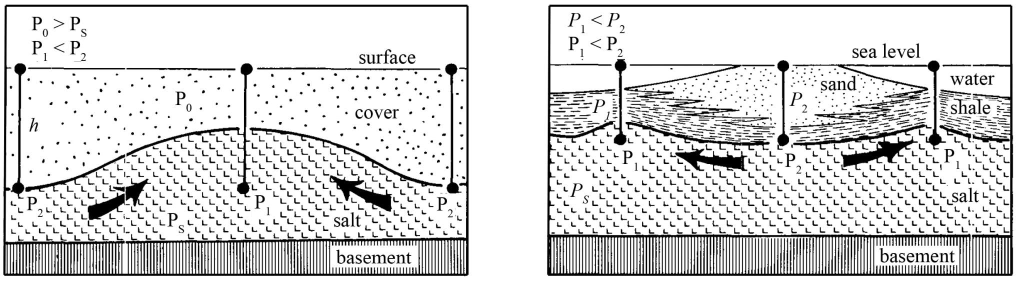

A) Bouyancy halokinesis

B) Differntial loading halokinesis

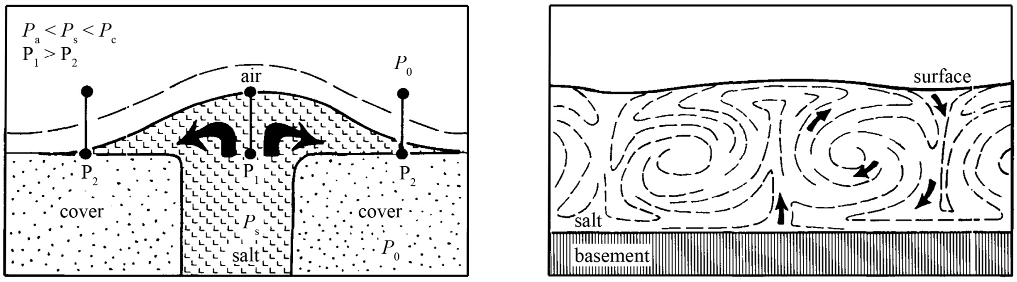

C) Gravity spreading halokinesis

D) Thermal convective halokinesis

Figure 2.3

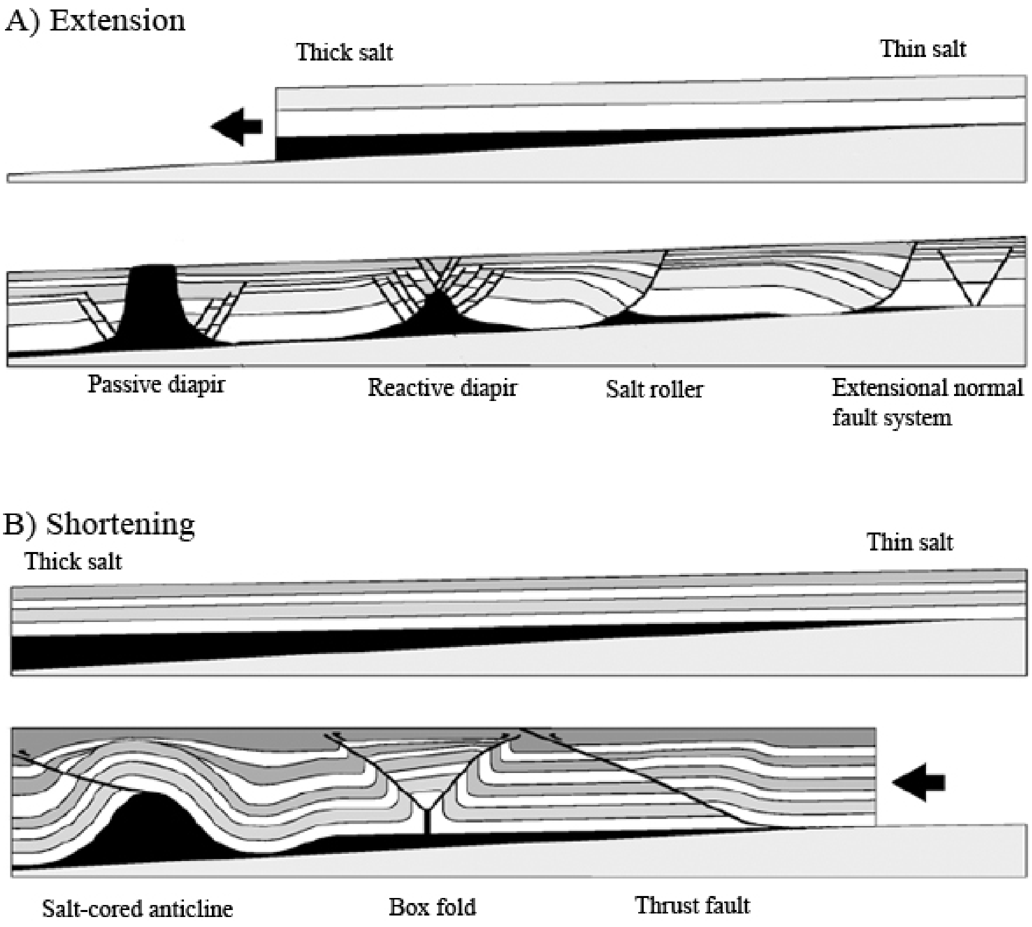
A) Extension
Thick salt
Thin salt
Passive diapir
Reactive diapir
Salt roller
Extensional normal fault system
B) Shortening
Thick salt
Thin salt
Salt-cored anticline
Box fold
Thrust fault

Figure 2.4

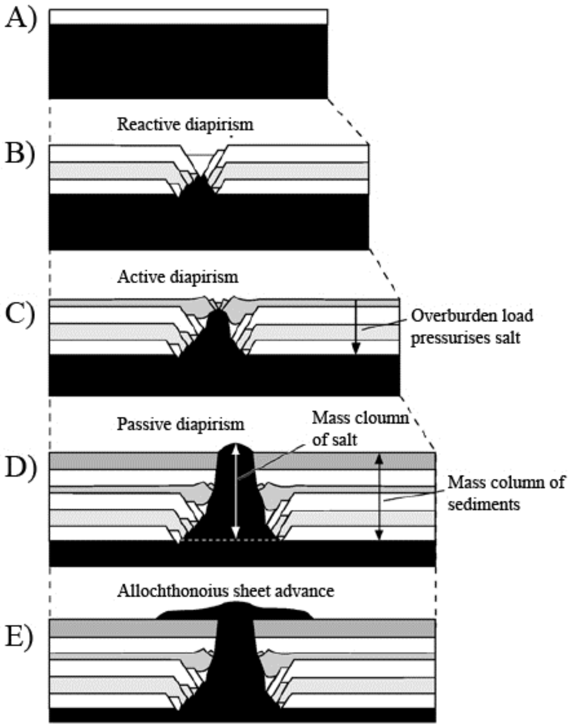

Figure 2.5

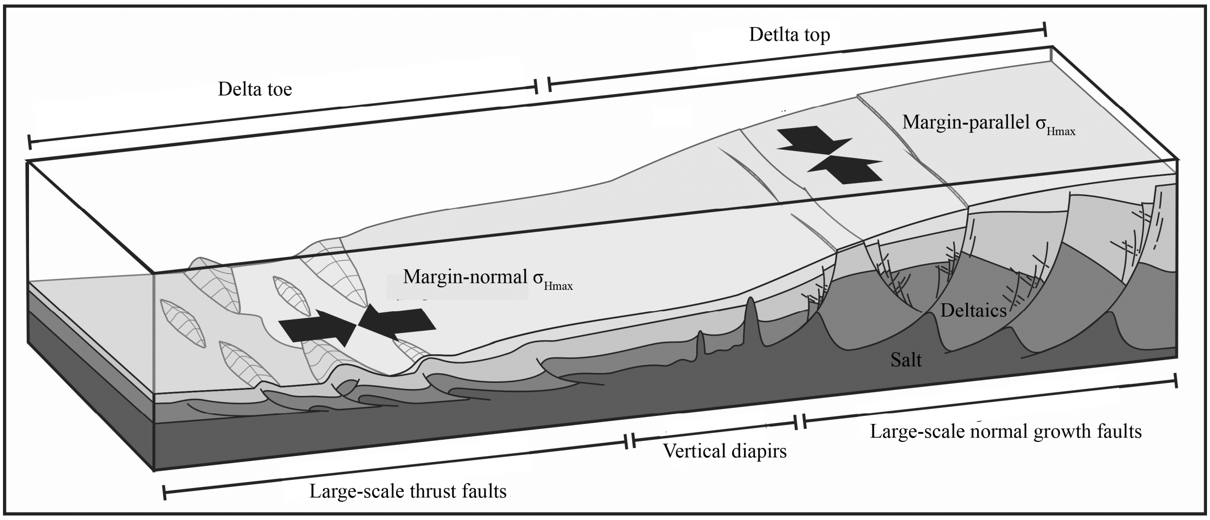

Figure 2.6

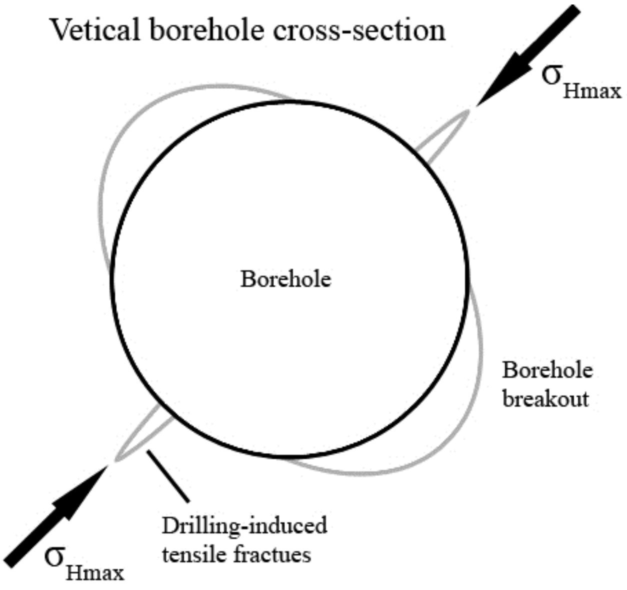

Figure 2.7

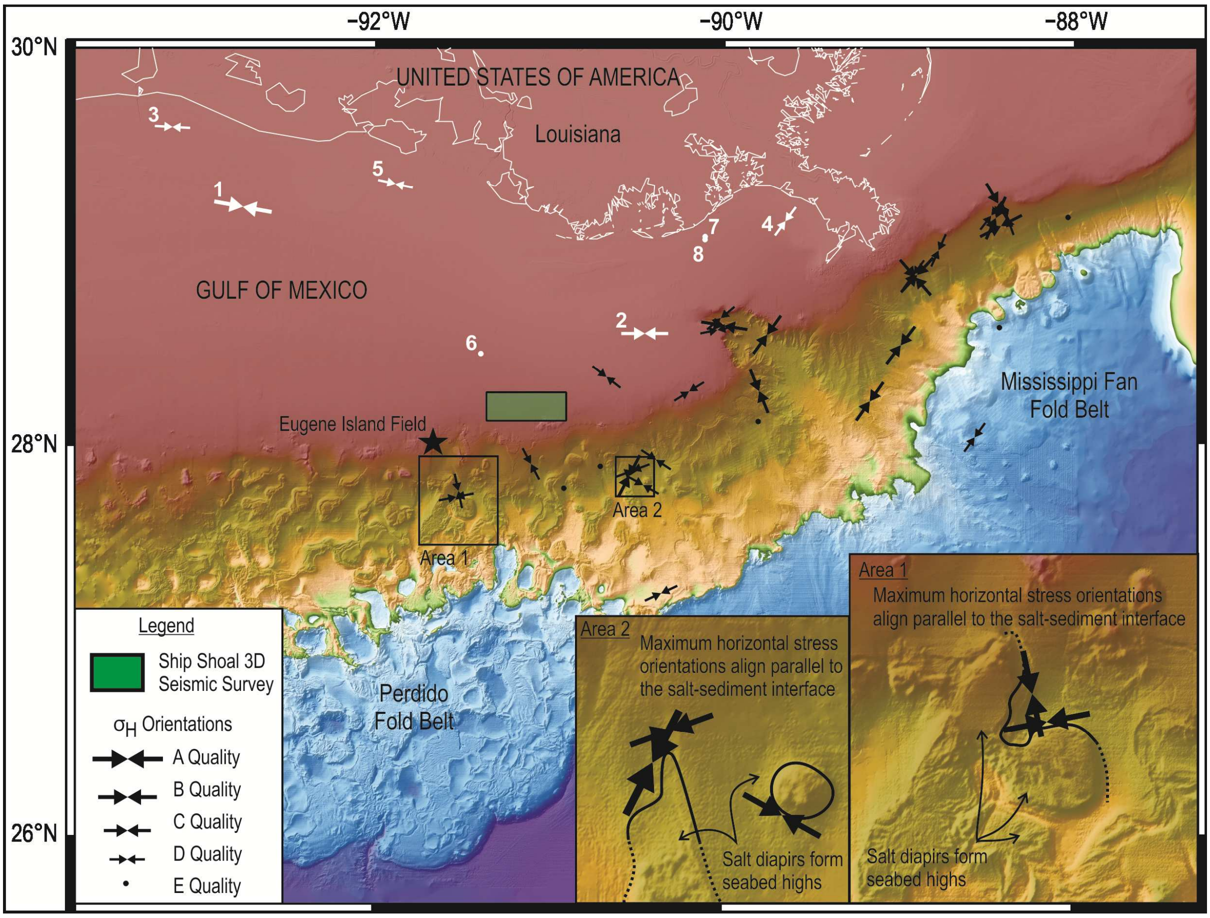

Figure 2.8

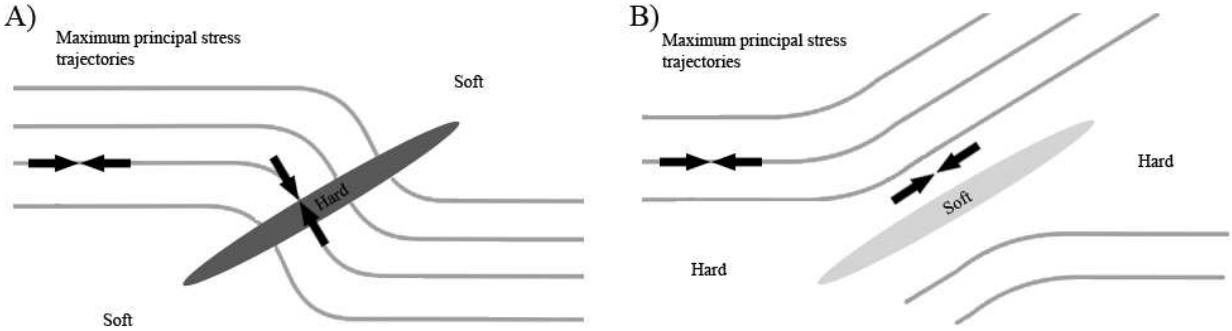

Figure 2.9

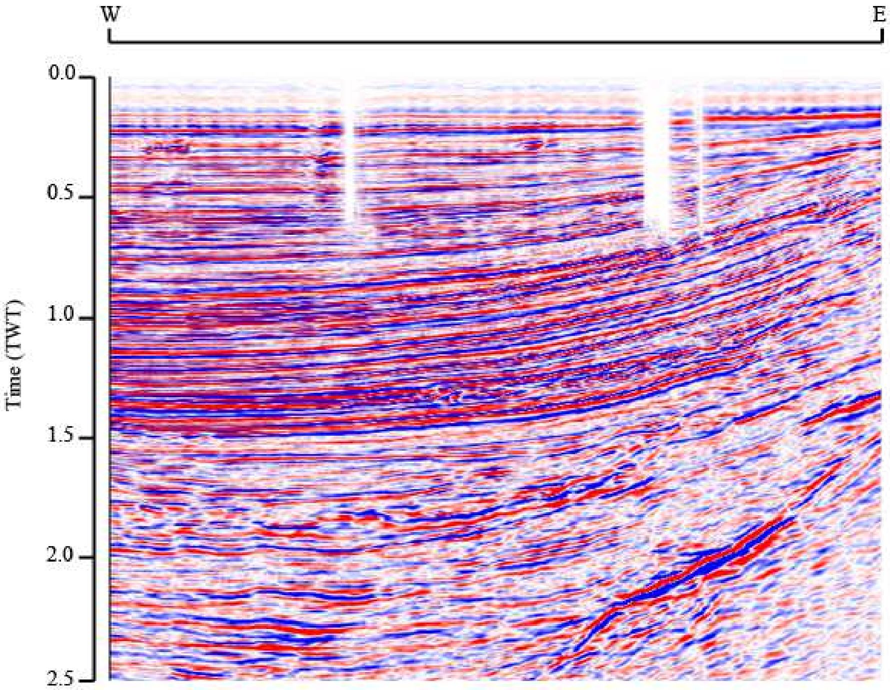

Figure 3.1

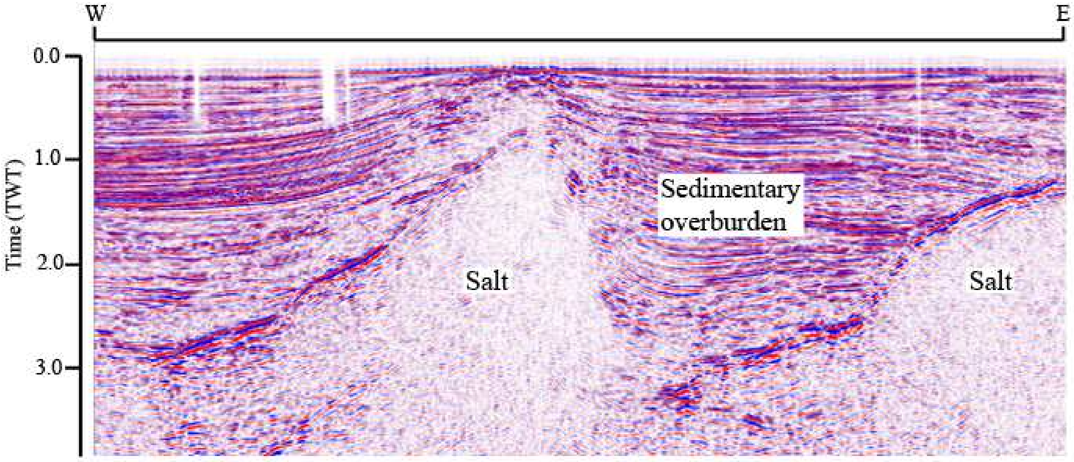

Figure 3.2

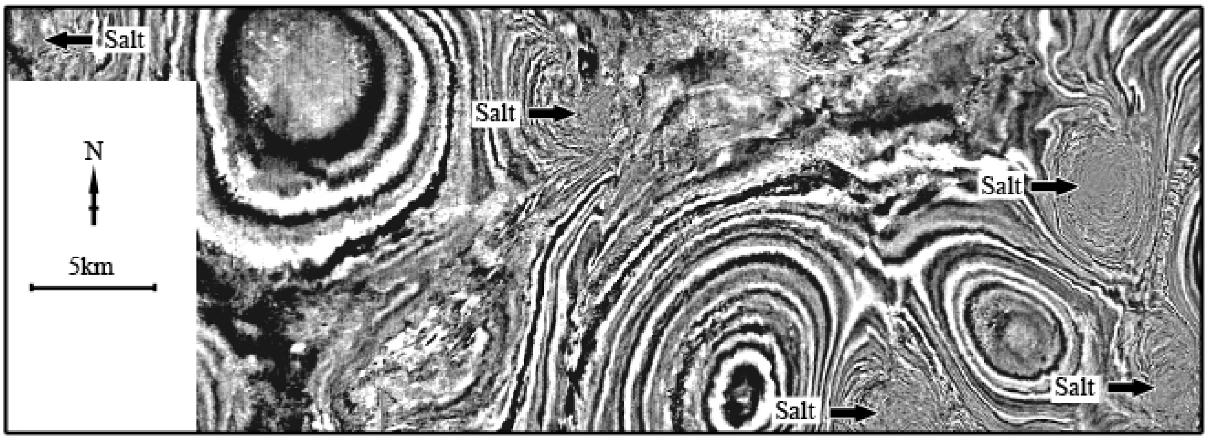

Figure 3.3

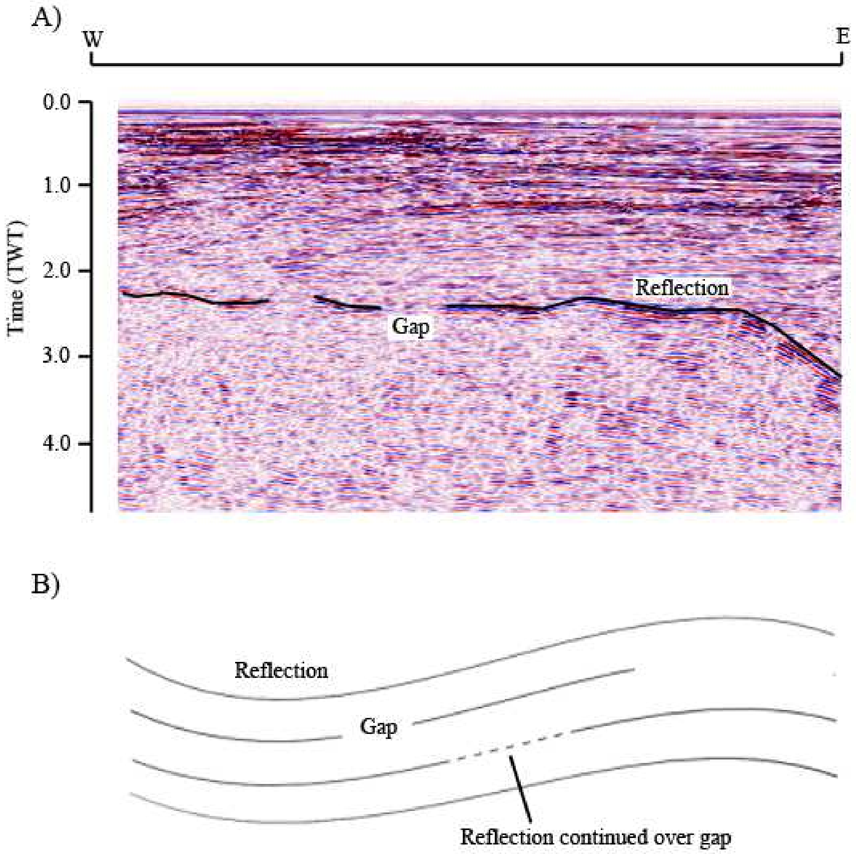

Figure 3.4

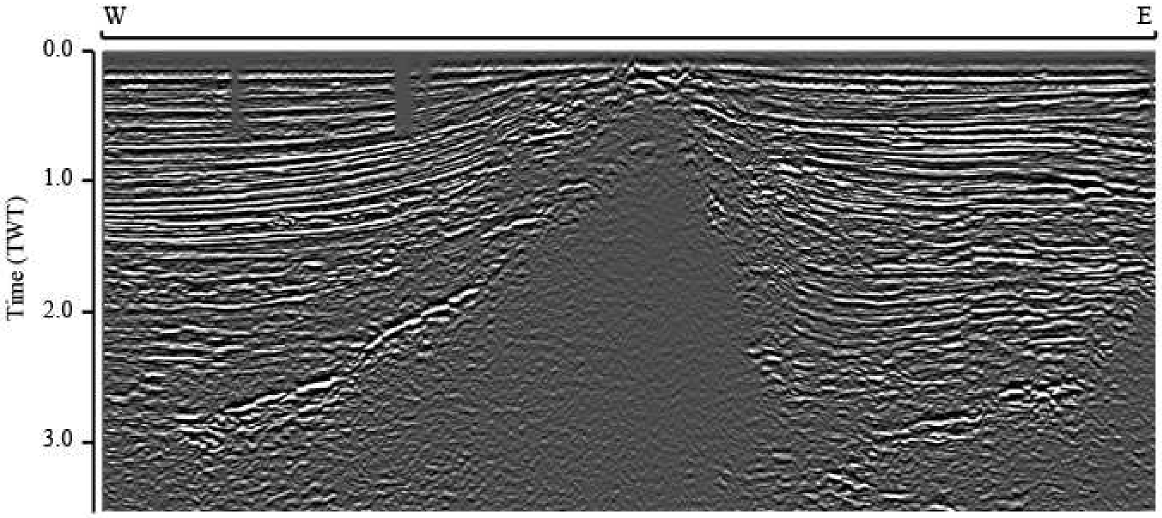

Figure 3.5

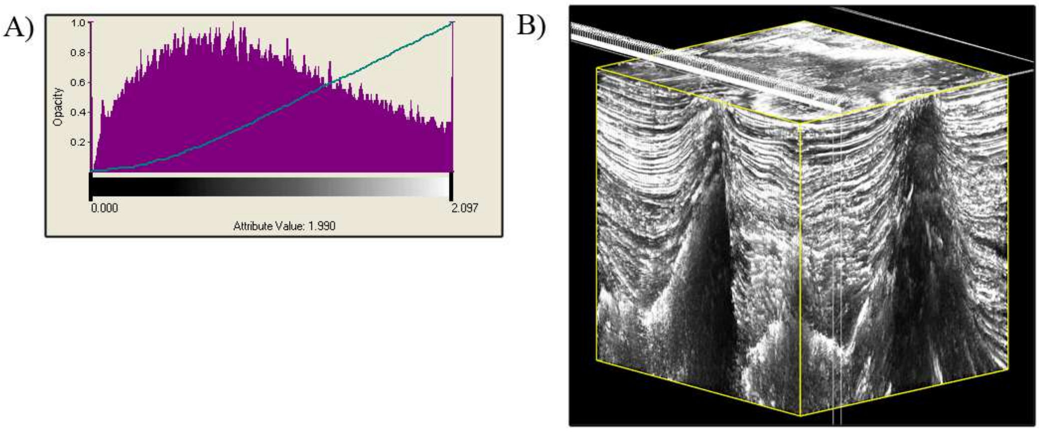

Figure 3.6

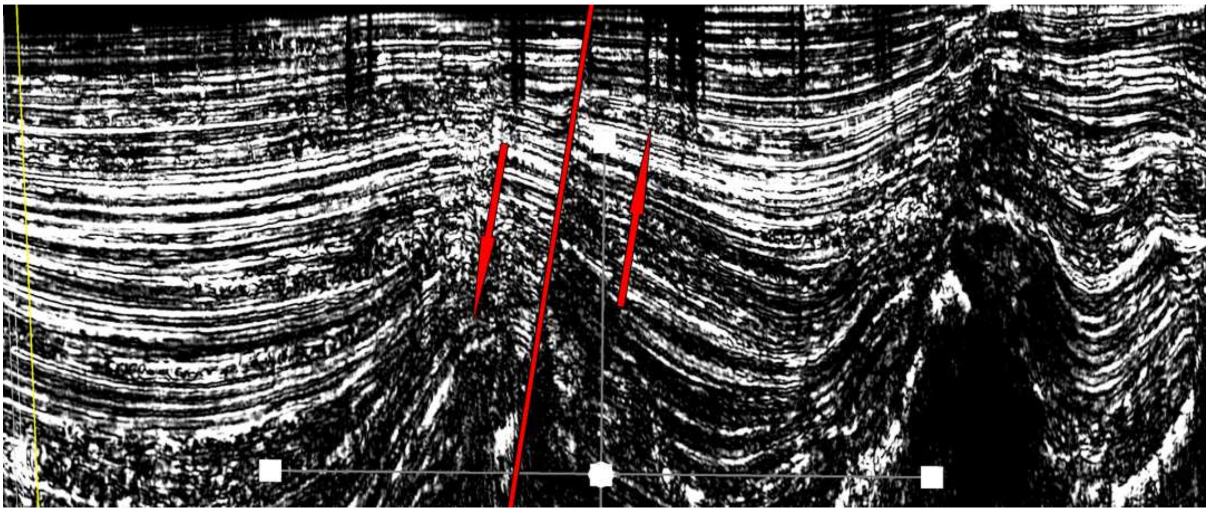

Figure 3.7

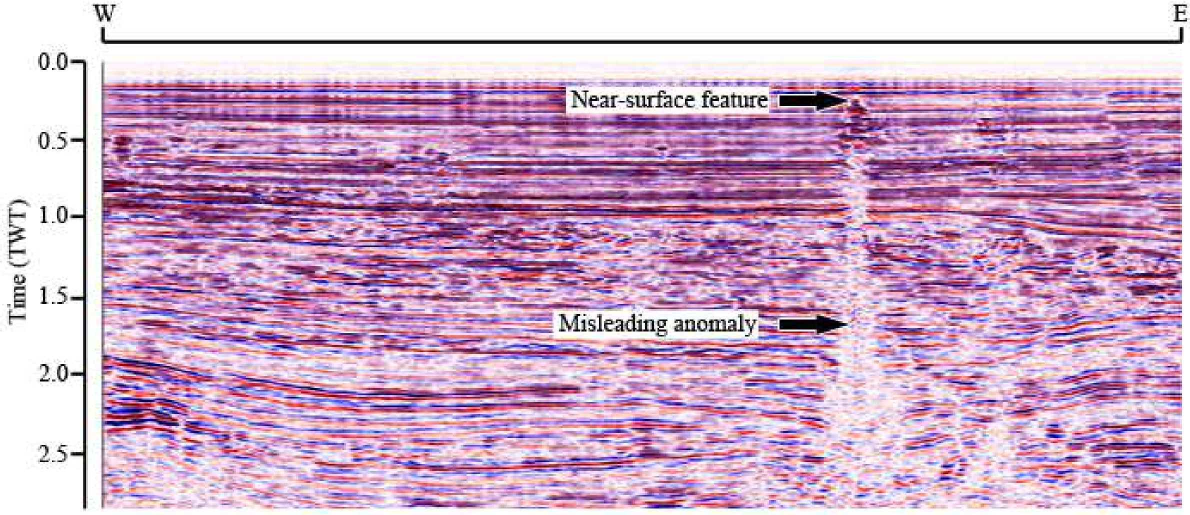

Figure 3.8

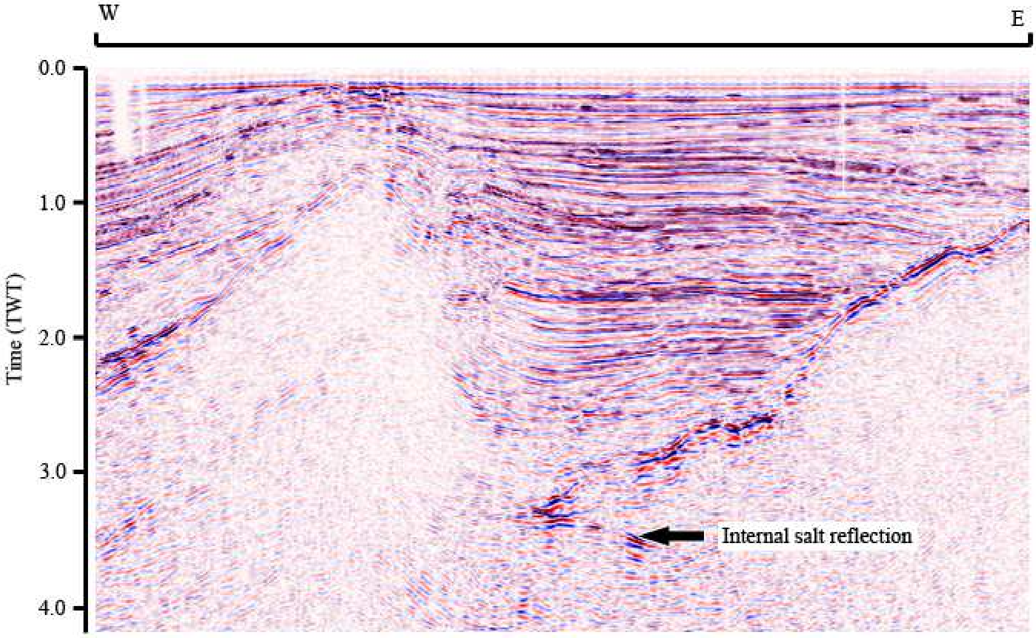

Figure 3.9

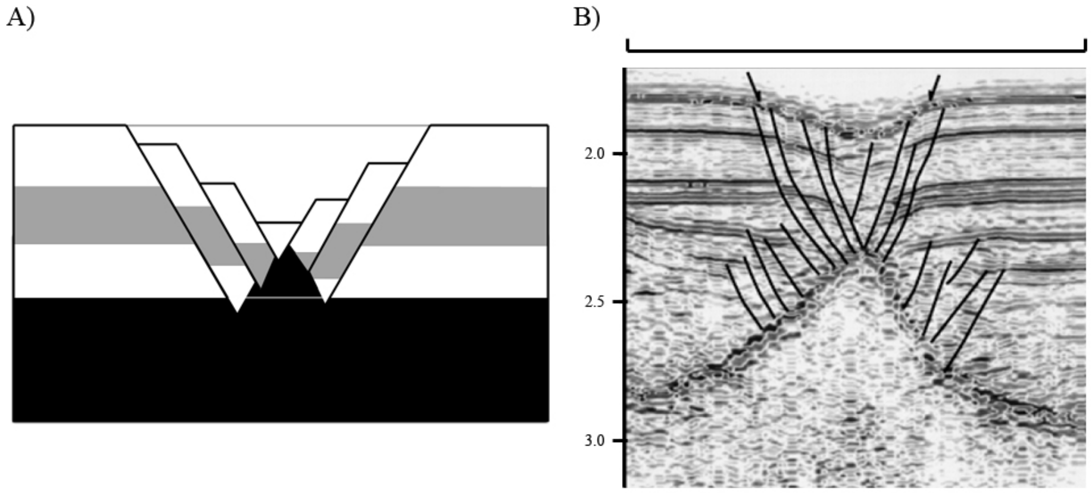

Figure 3.10

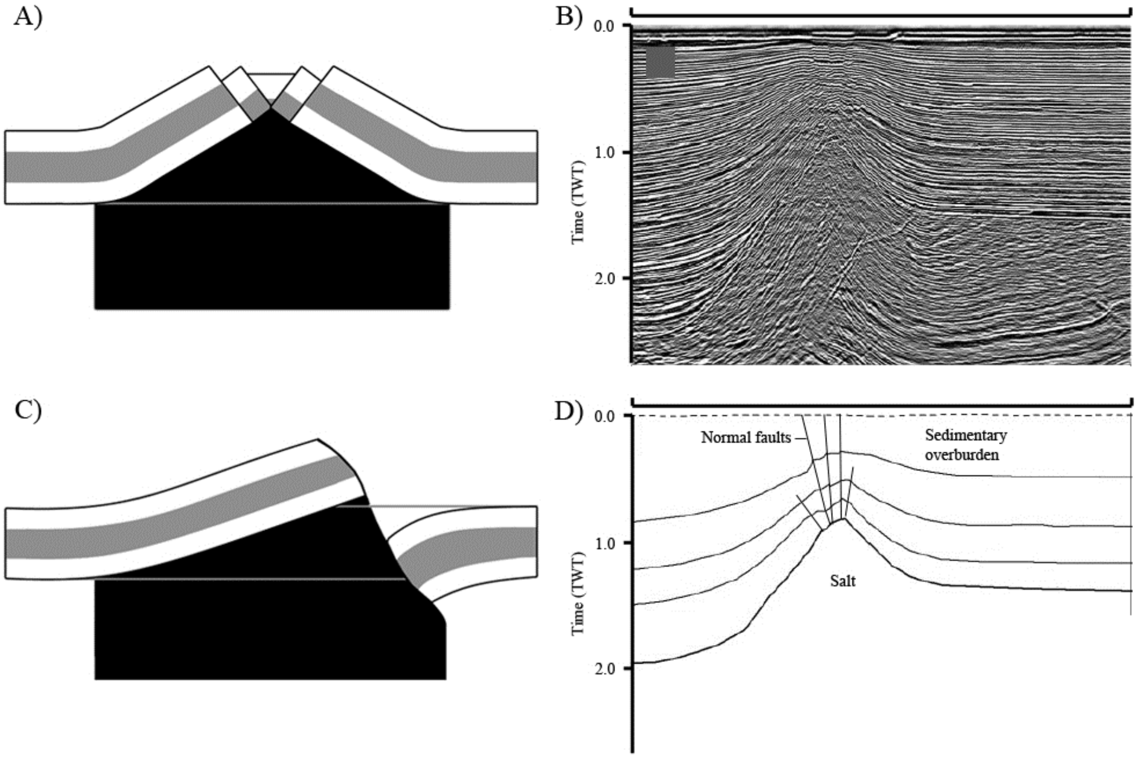

Figure 3.11

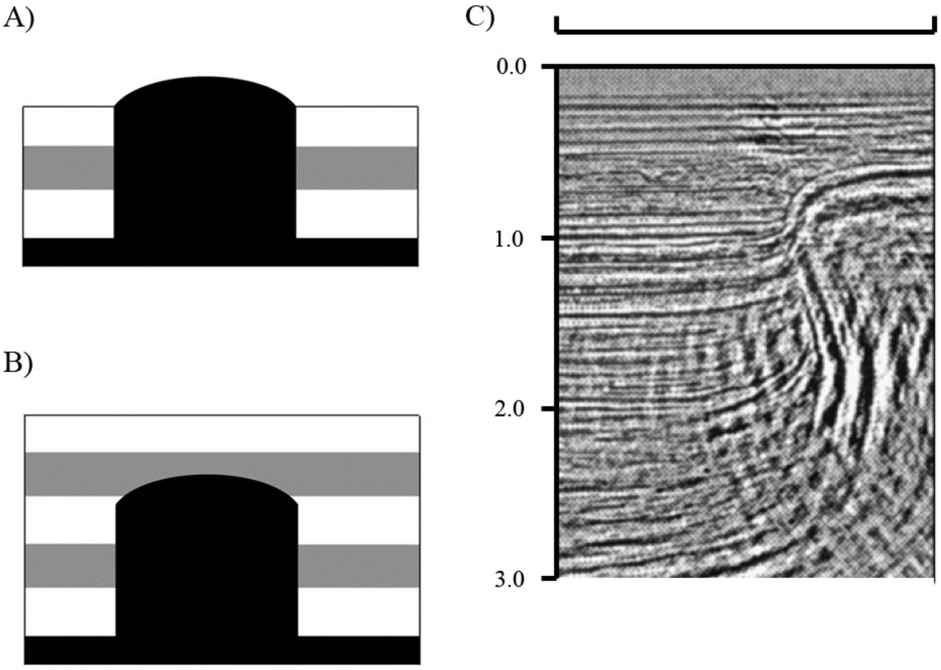

Figure 3.12

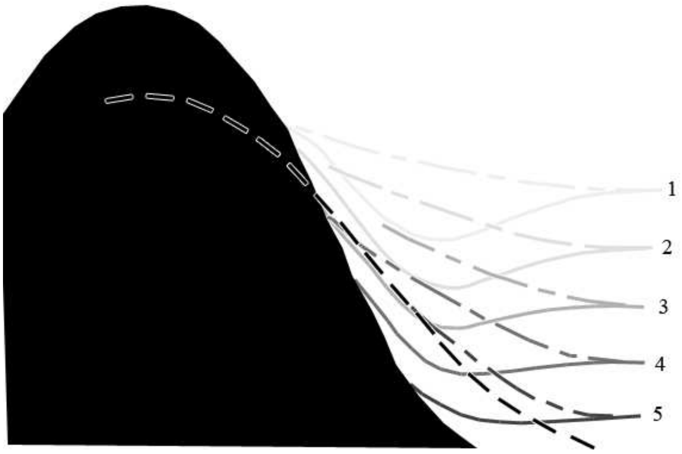

Figure 3.13

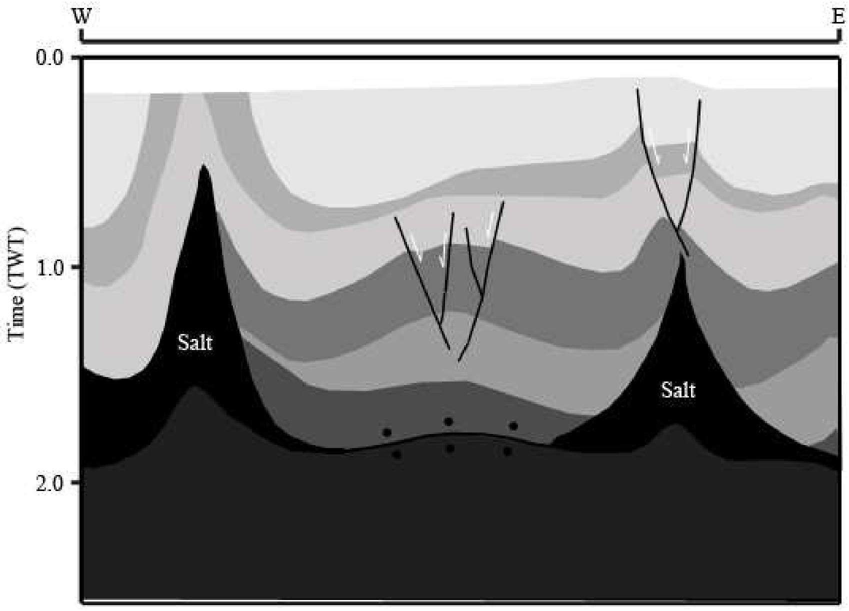

Figure 3.14

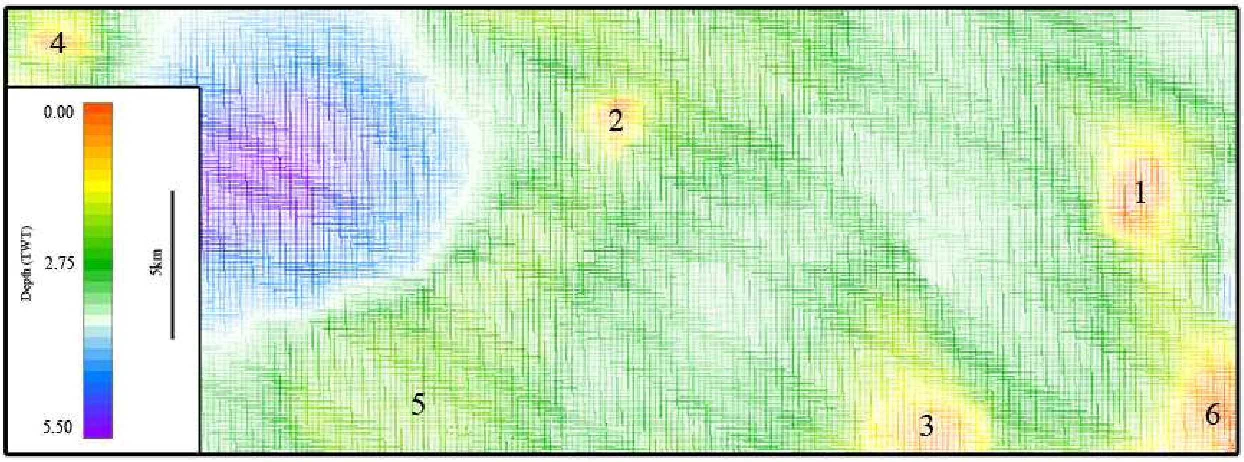

Figure 4.1

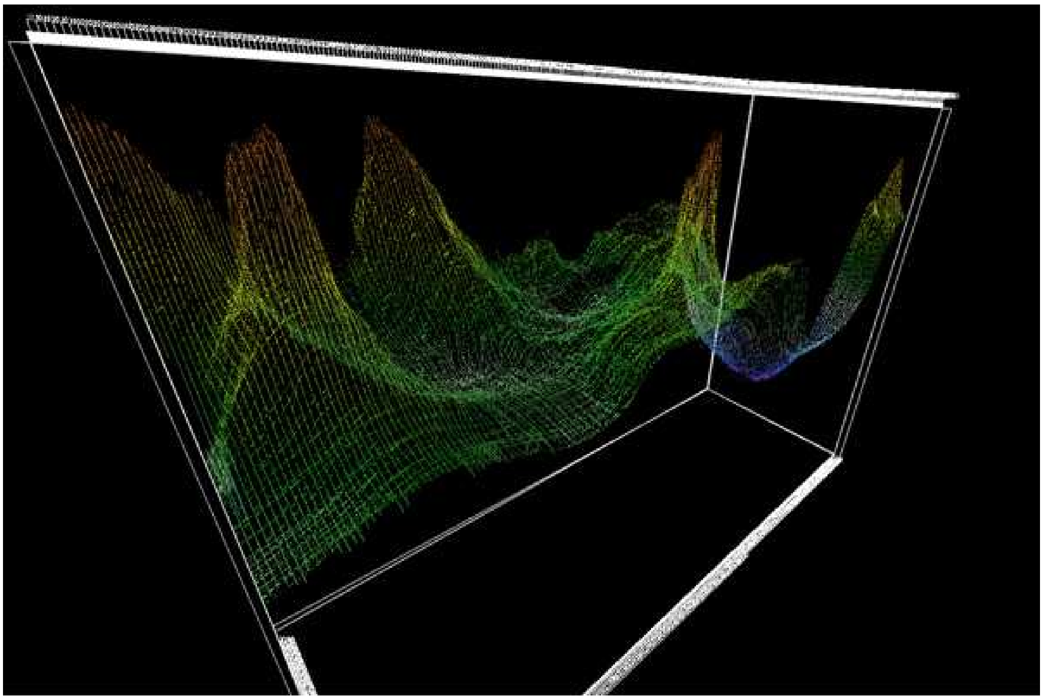

Figure 4.2

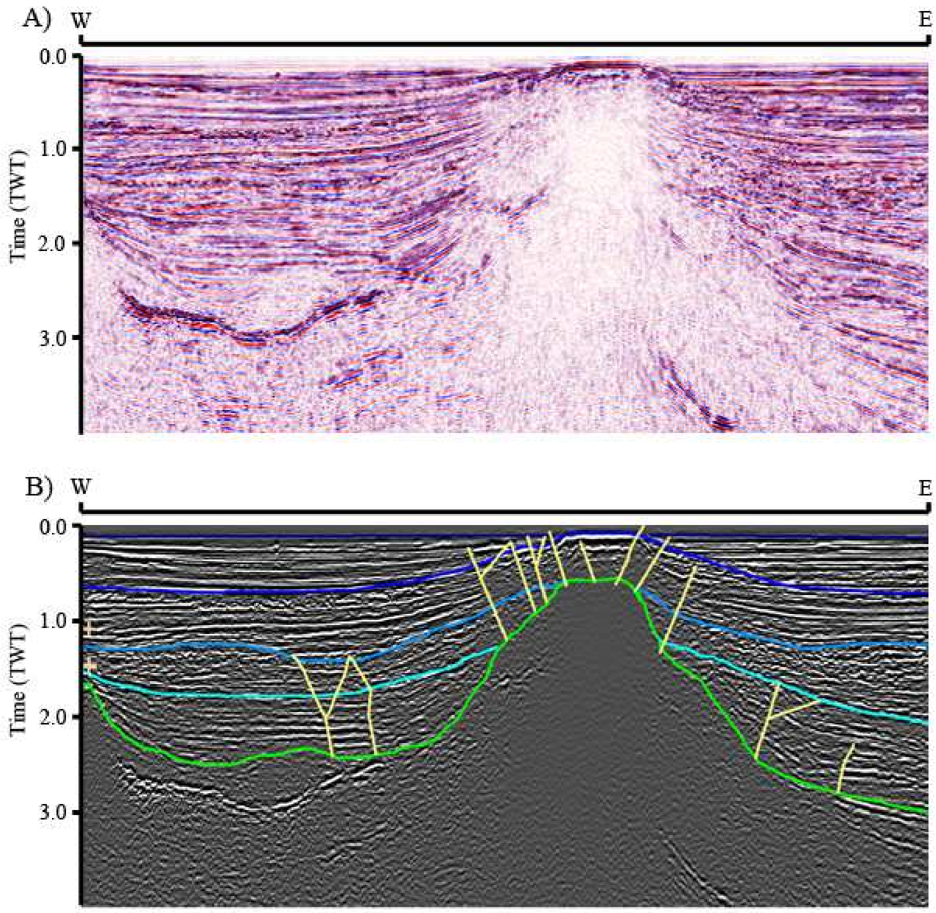

Figure 4.3

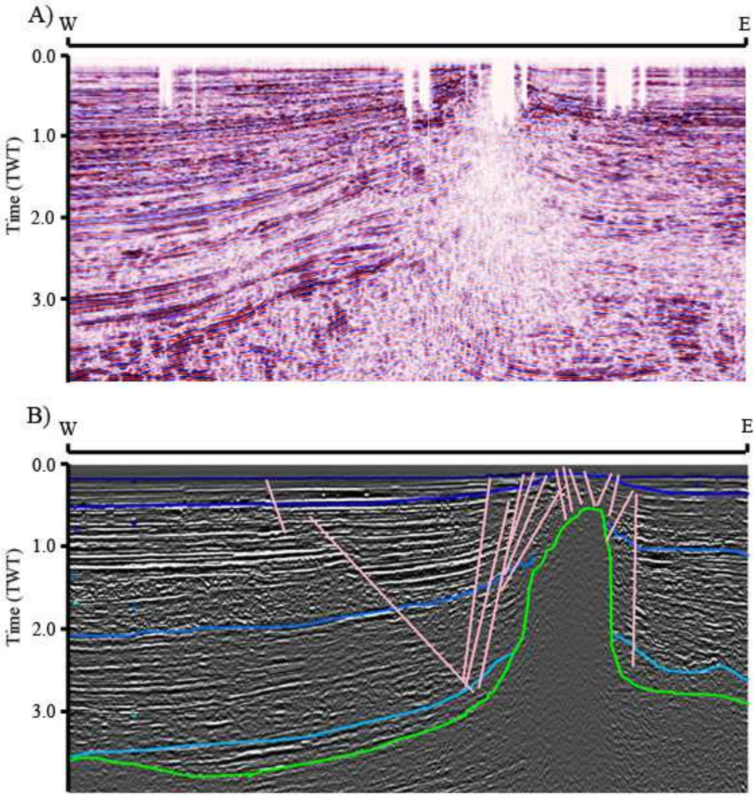

Figure 4.4

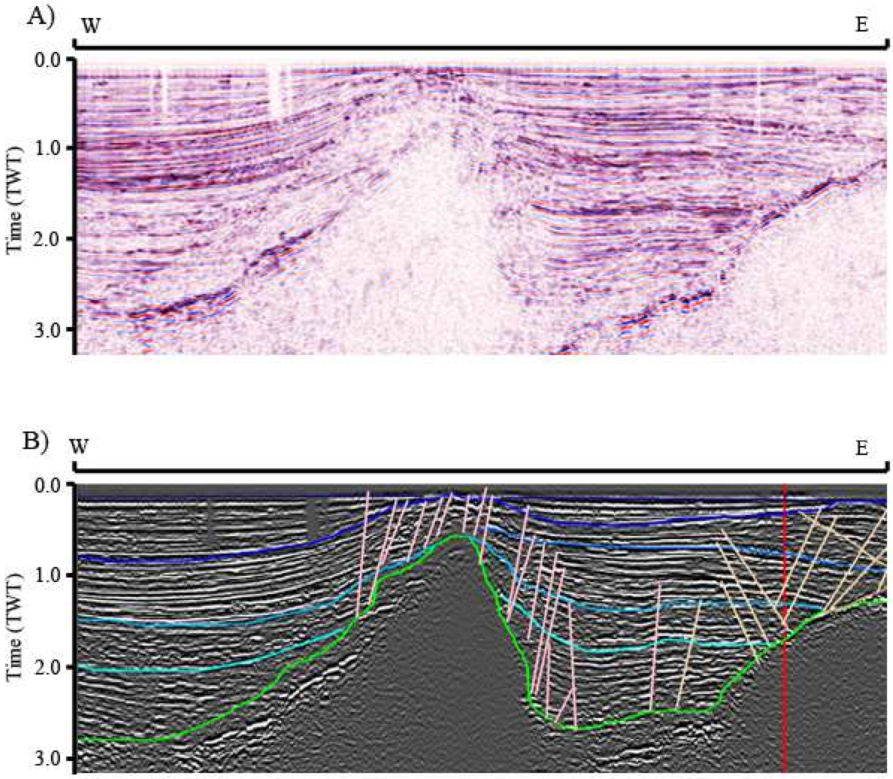

Figure 4.5

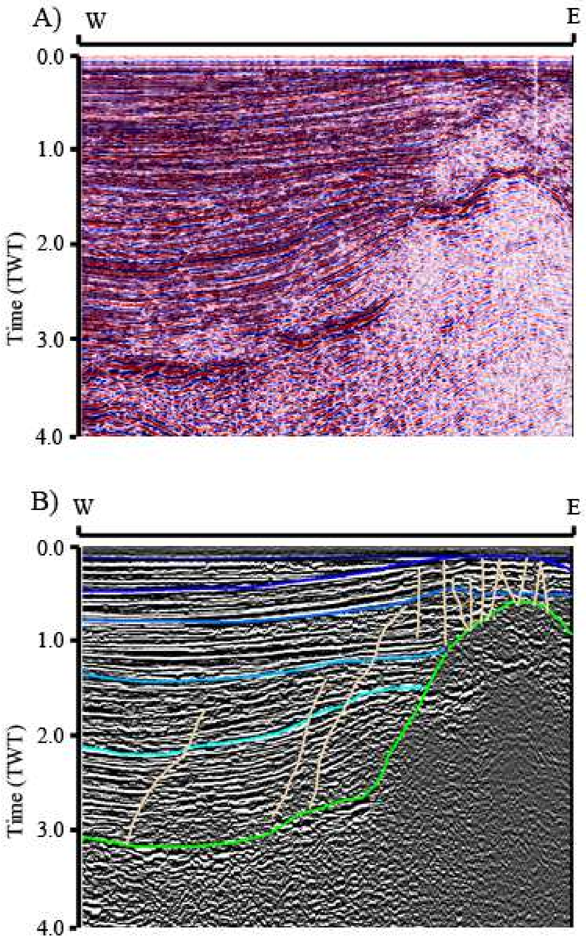

Figure 4.6

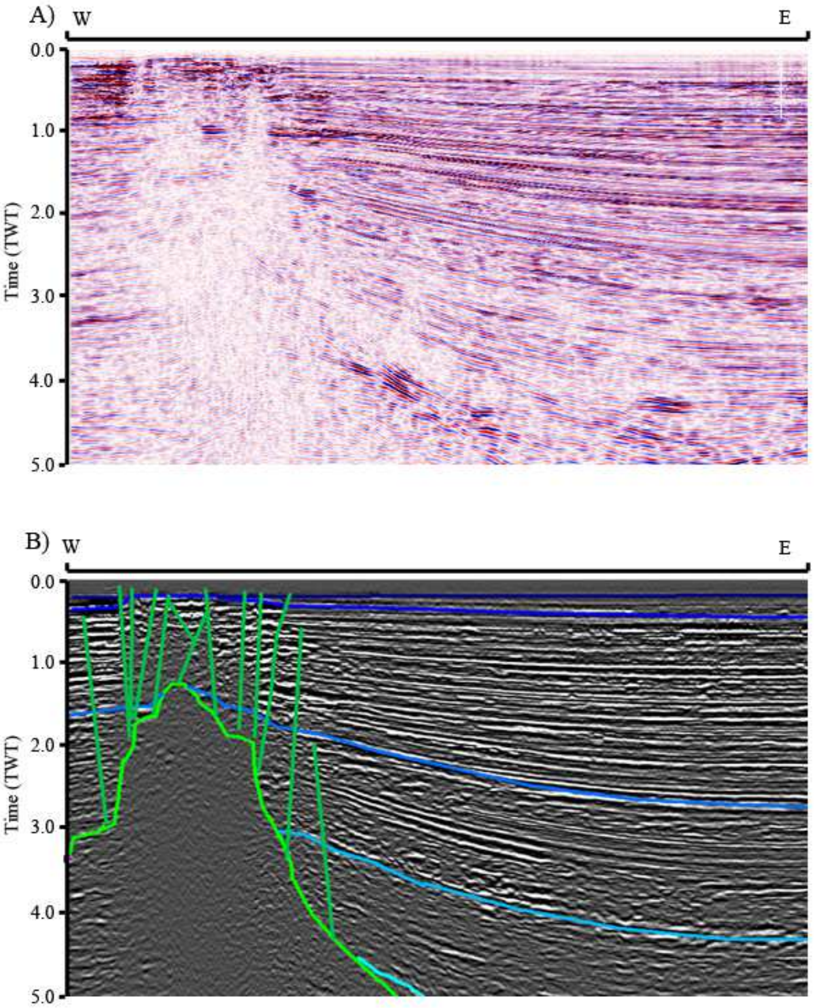

Figure 4.7

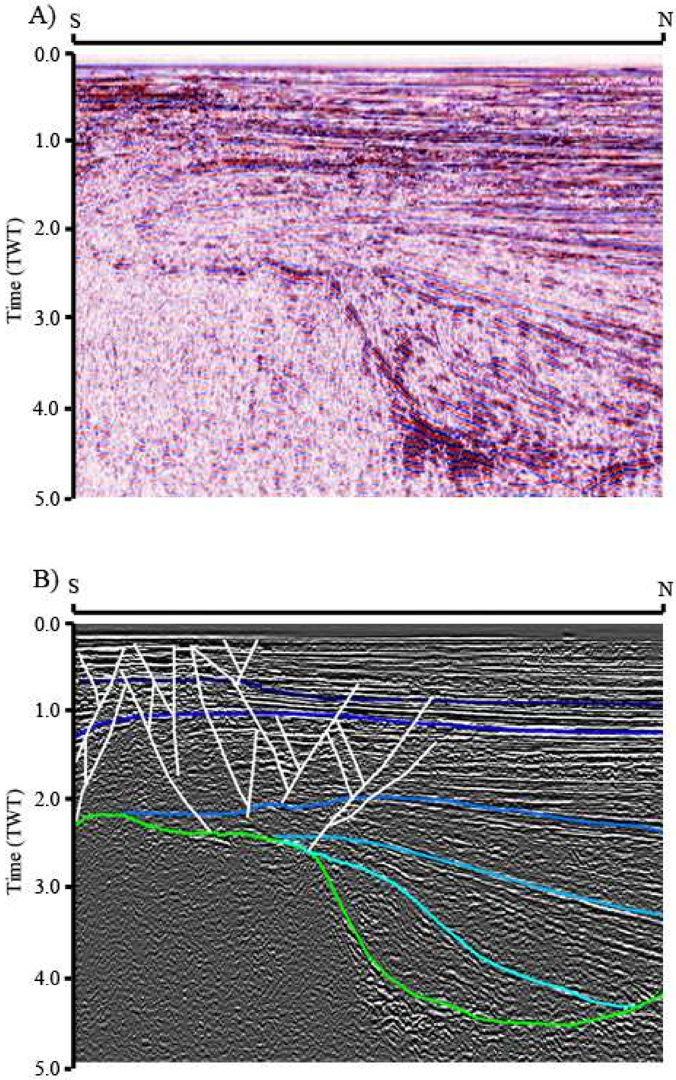

Figure 4.8

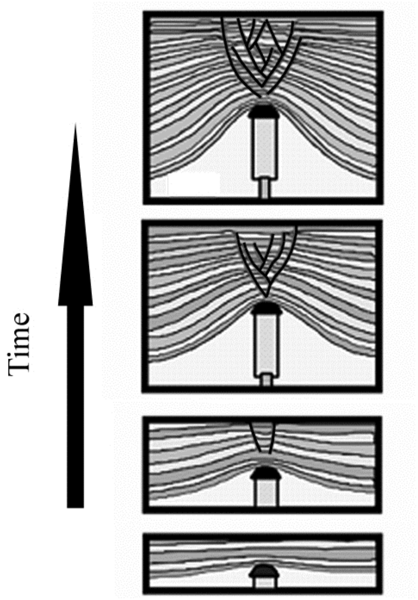

Figure 4.9

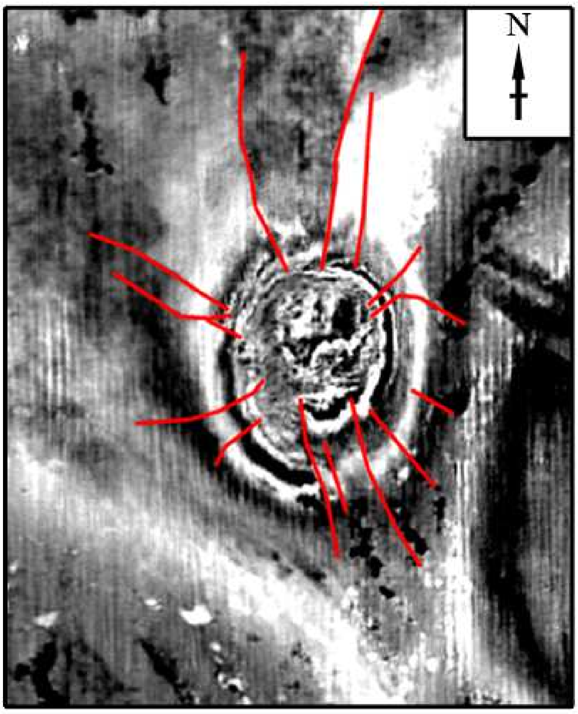

Figure 4.10

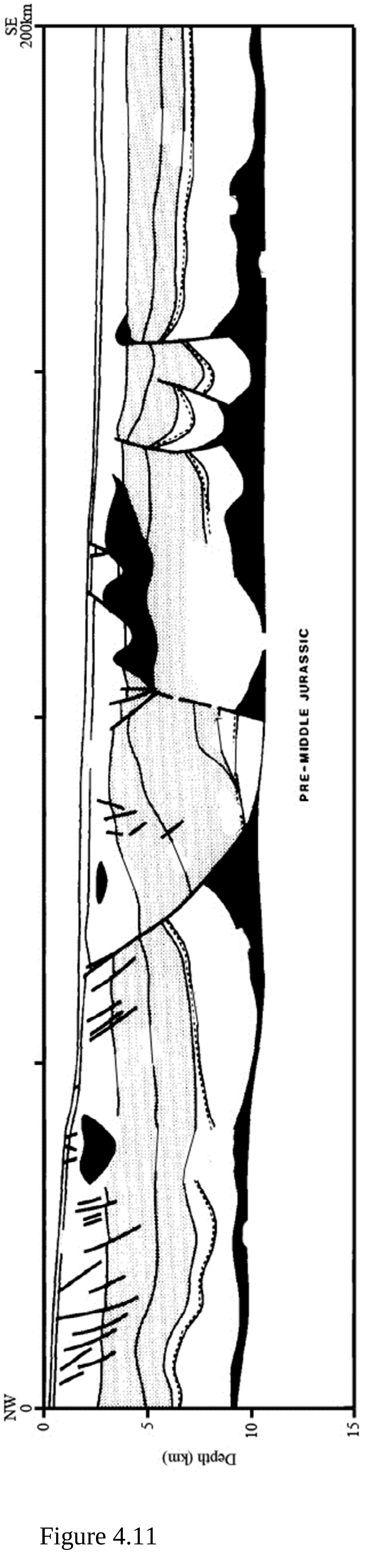

Figure 4.11

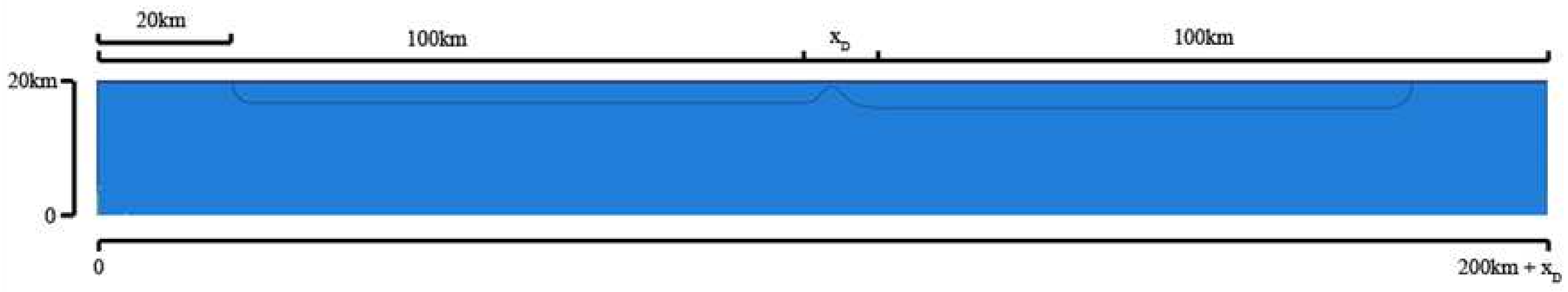

Figure 5.1

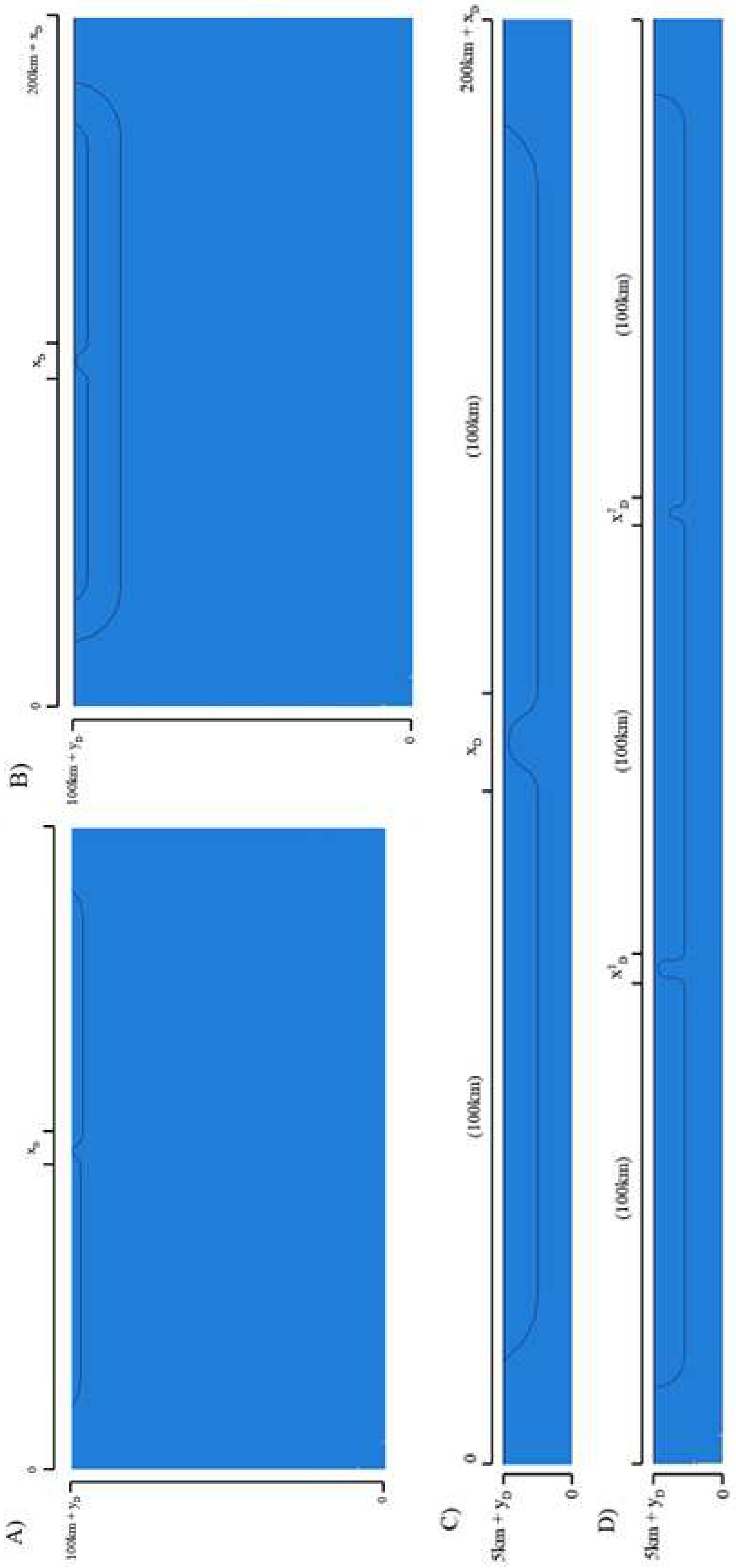
A)
100km + y_D
0
0
x_D
B)
100km + y_D
0
0
x_D
200km + x_D
C)
5km + y_D
0
0
(100km)
x_D
(100km)
200km + x_D
D)
5km + y_D
0
(100km)
x^1_D
(100km)
x^2_D
(100km)

Figure 5.2

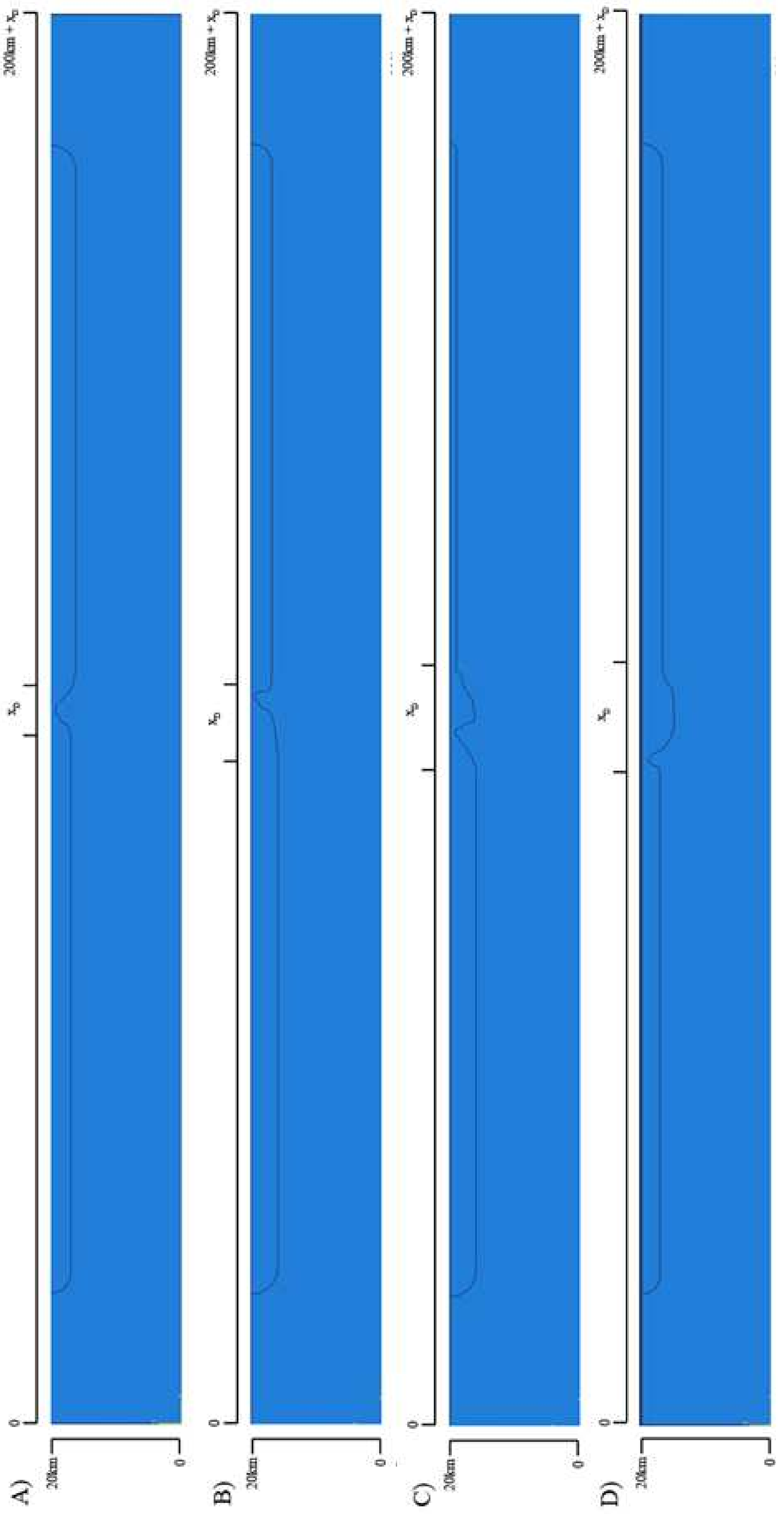

Figure 5.3

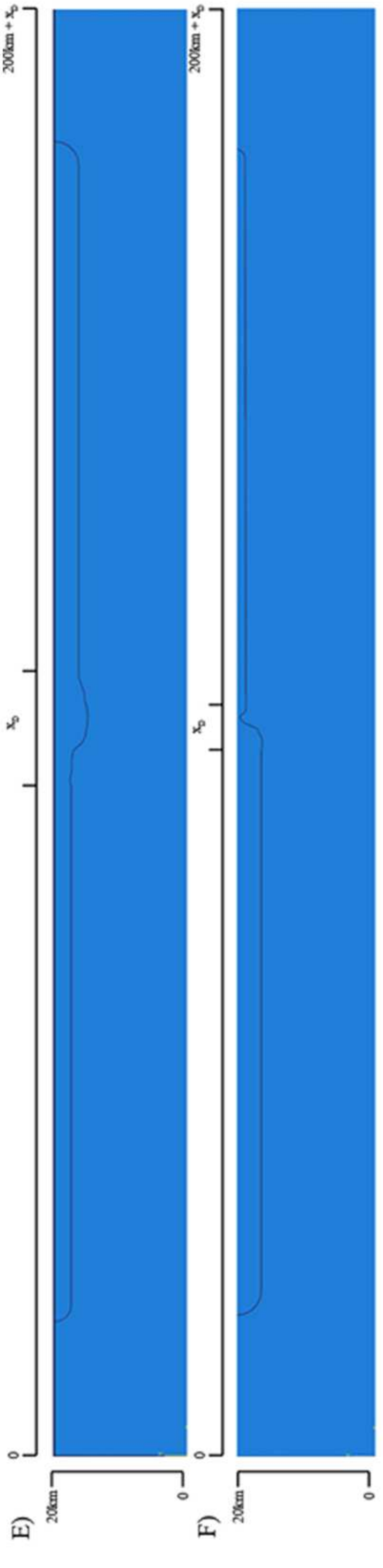

Figure 5.3 continued

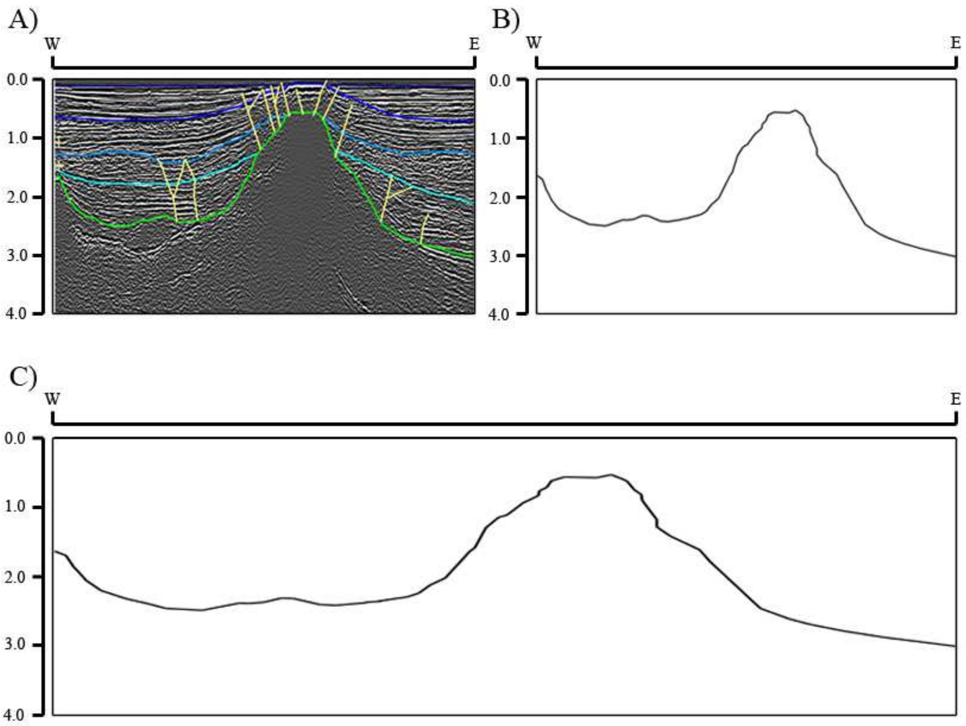

Figure 5.4

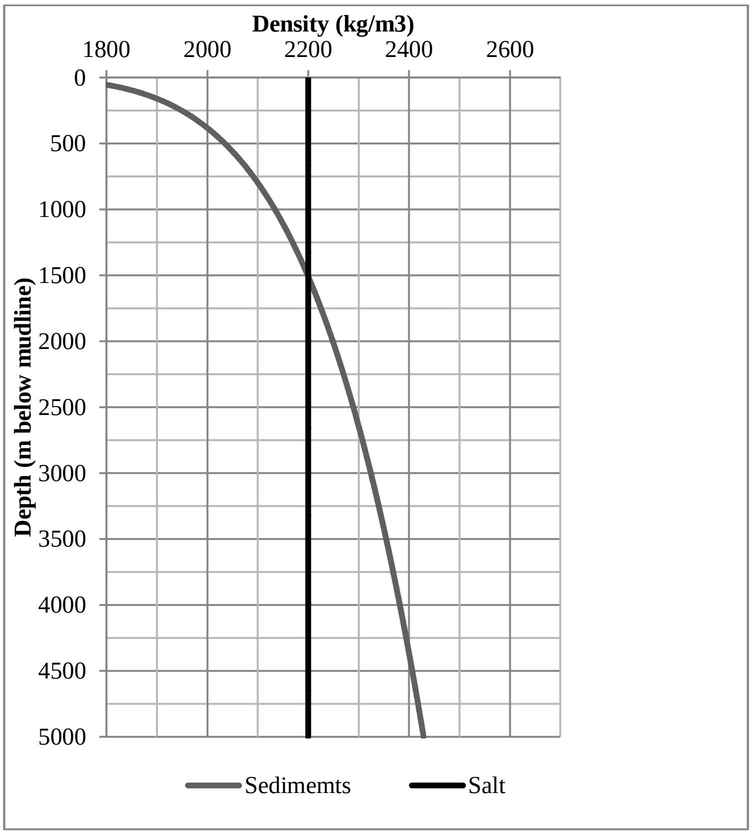

Figure 5.5

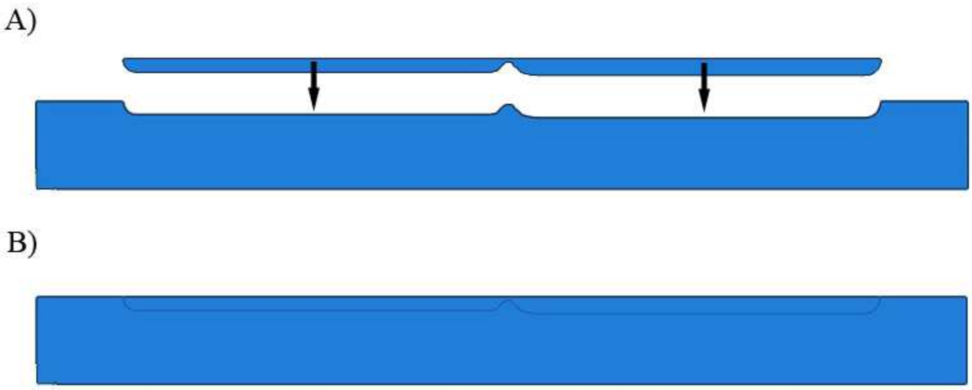

Figure 5.6

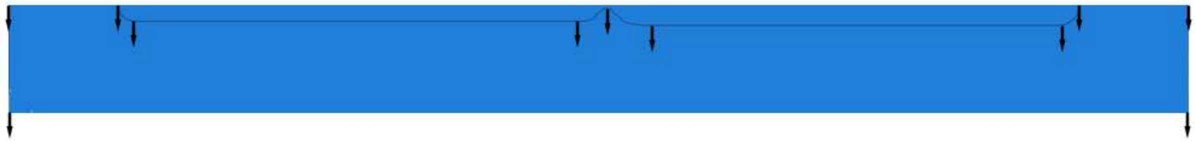

Figure 5.7

Figure 5.8

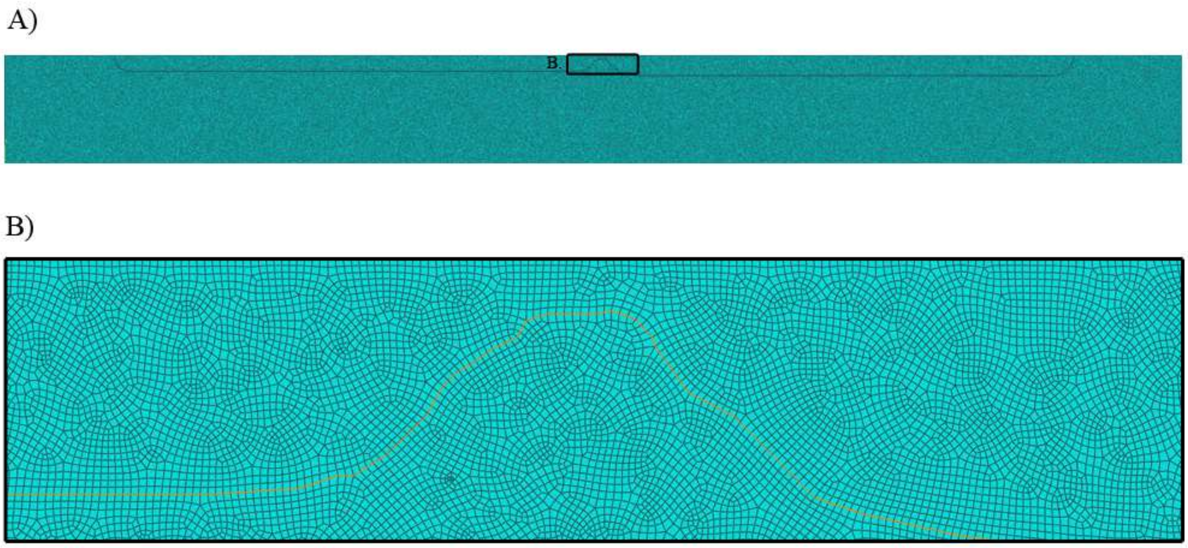

Figure 5.9

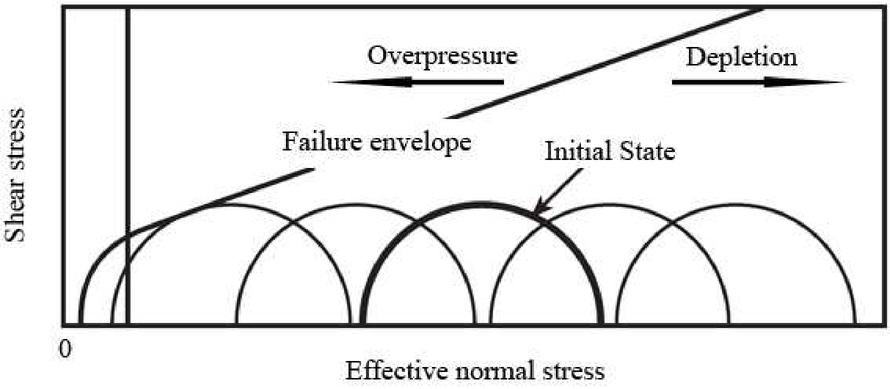

Figure 5.10

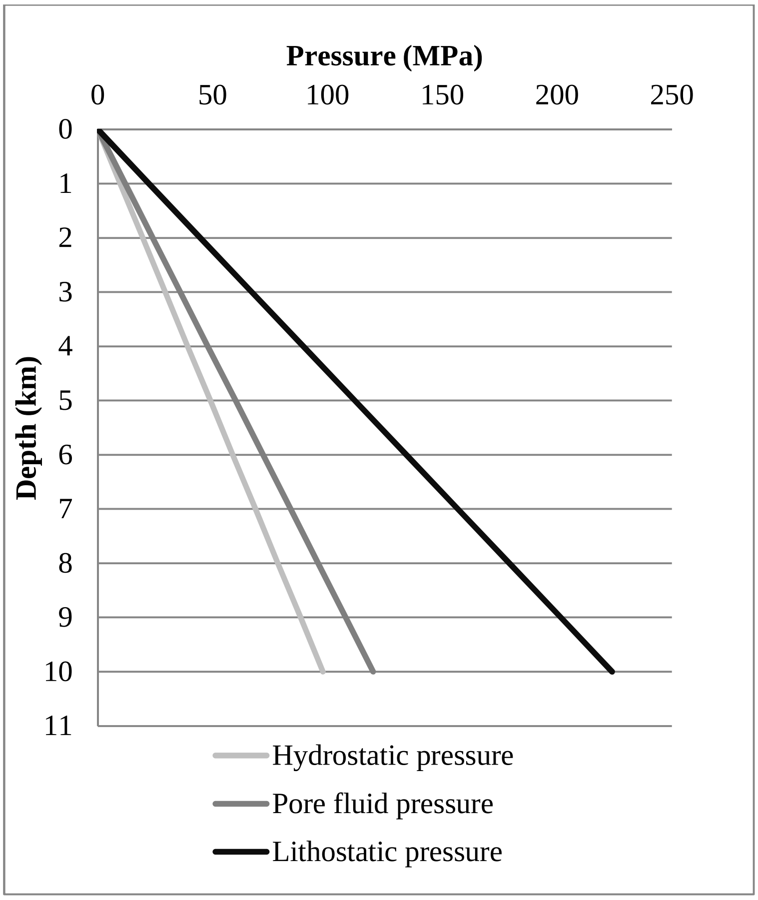

Figure 5.11

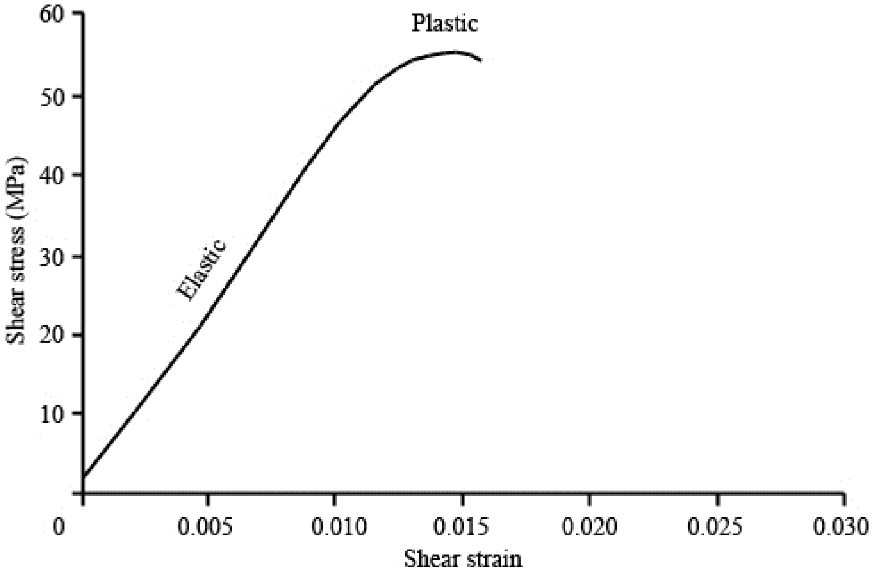

Figure 5.12

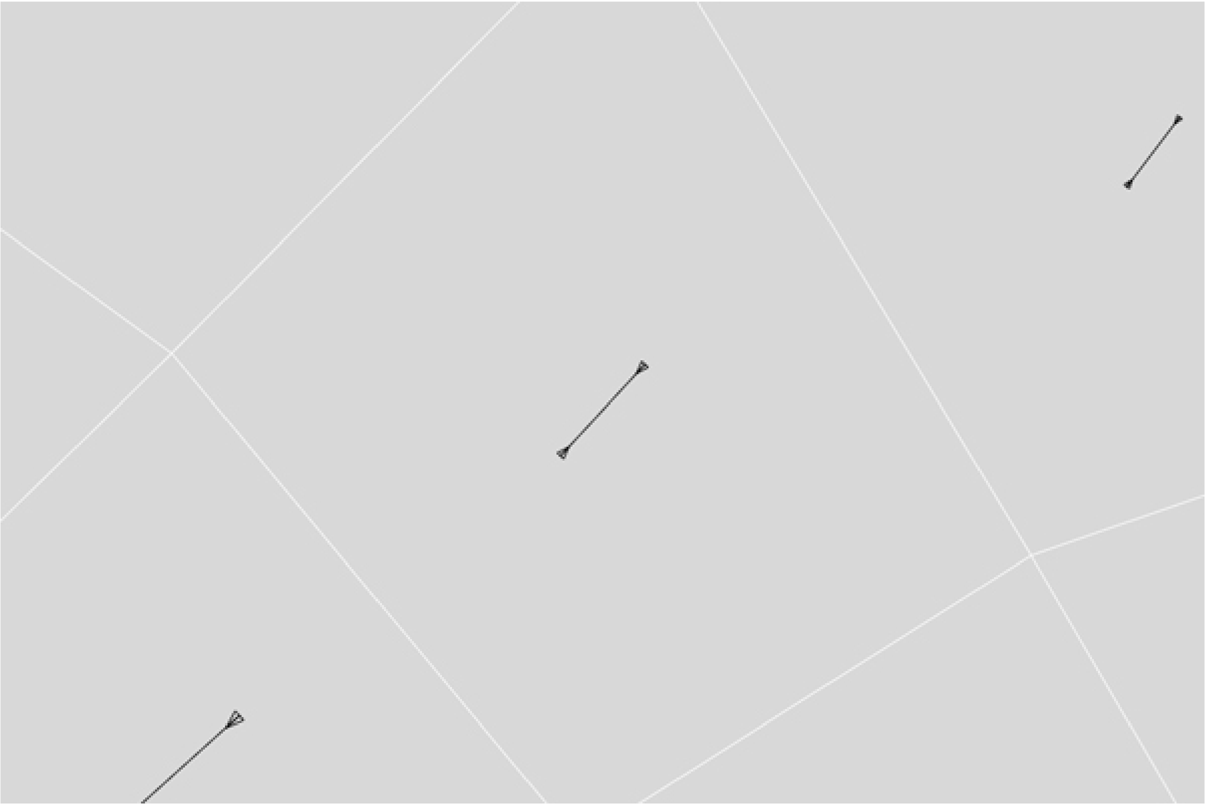

Figure 6.1

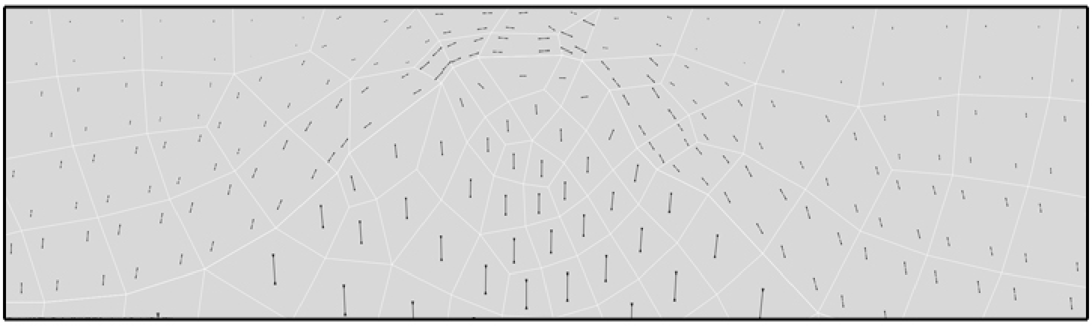

Figure 6.2

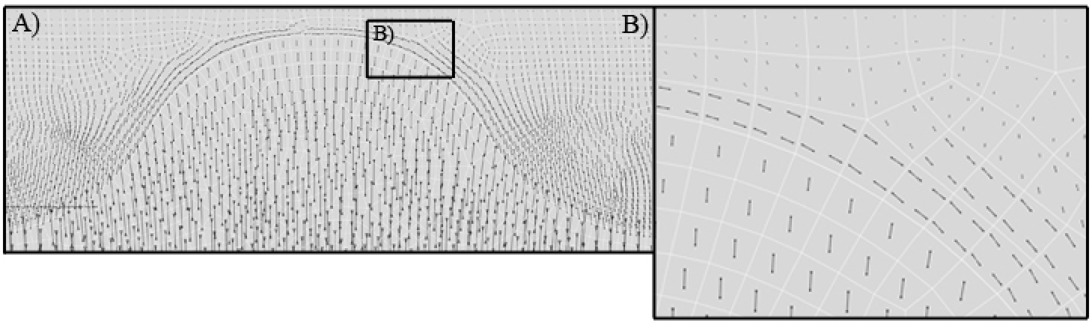

Figure 6.3

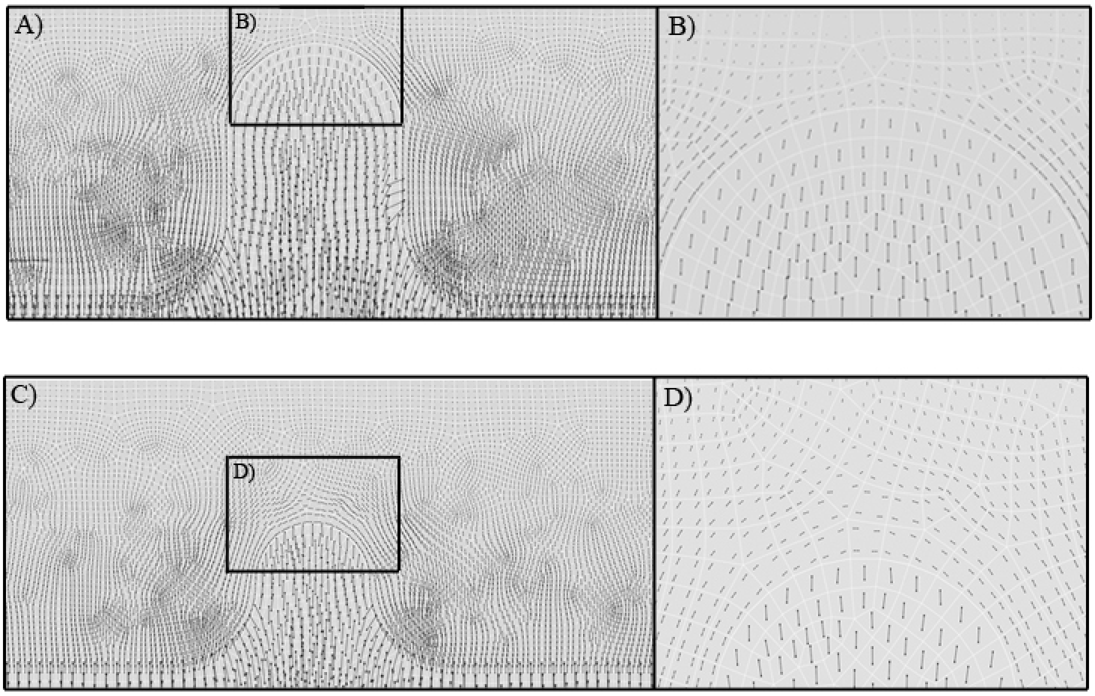

Figure 6.4

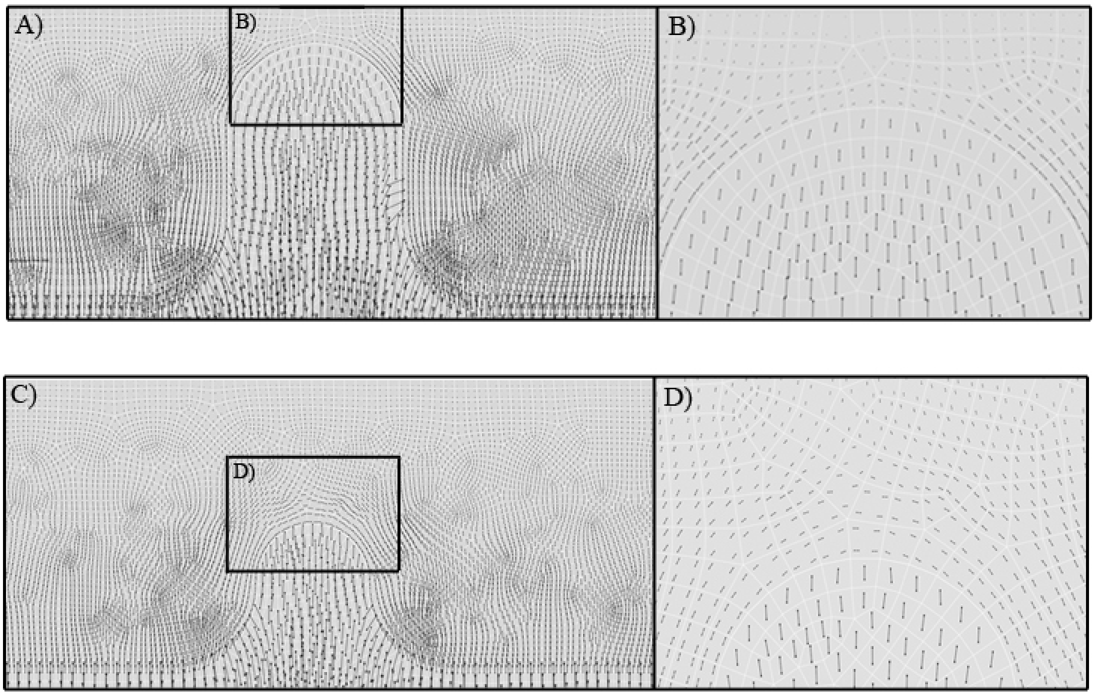

Figure 6.5

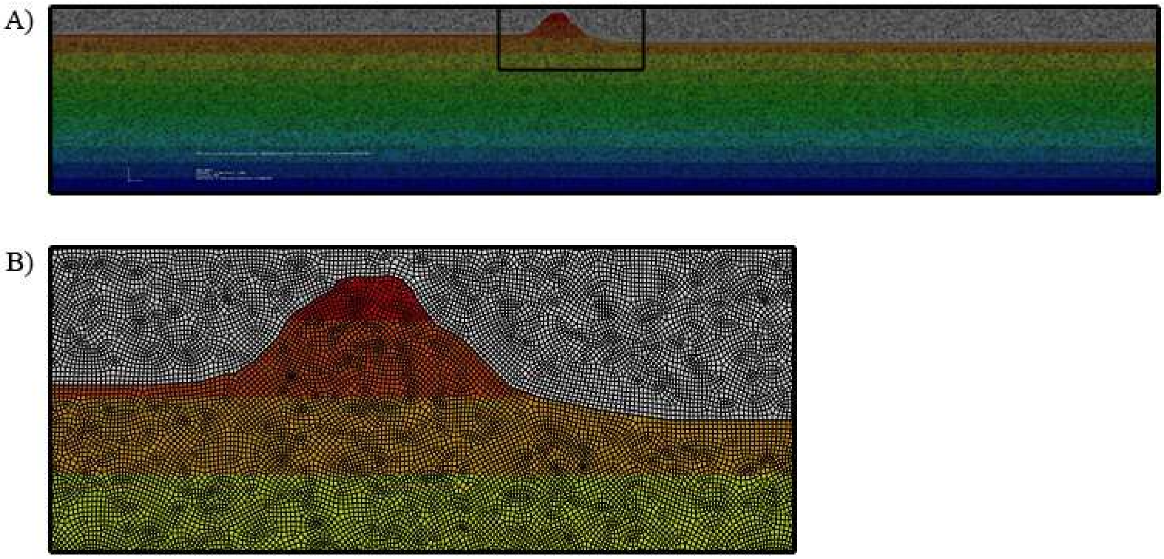

Figure 6.6

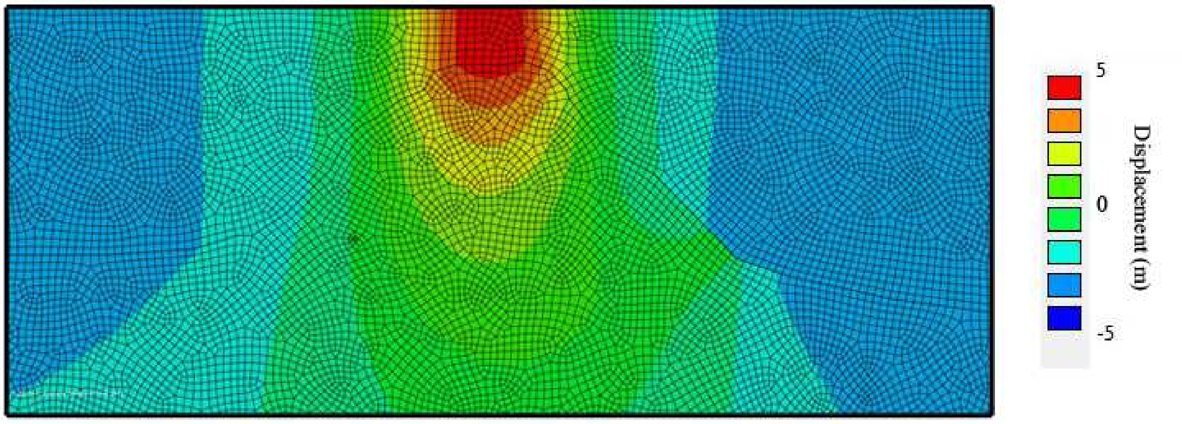

Figure 6.7

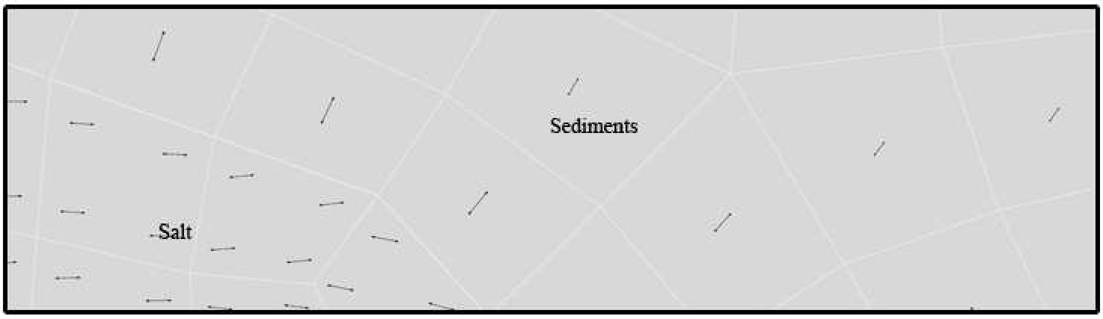

Figure 6.8

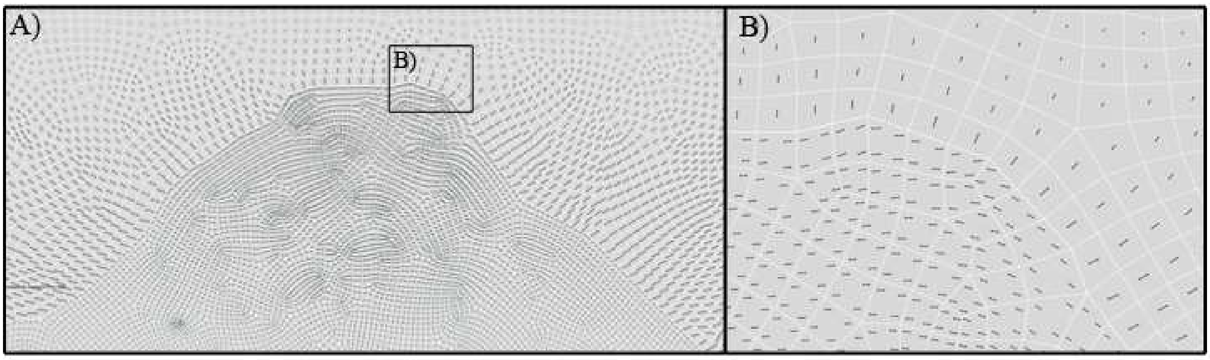

Figure 6.9

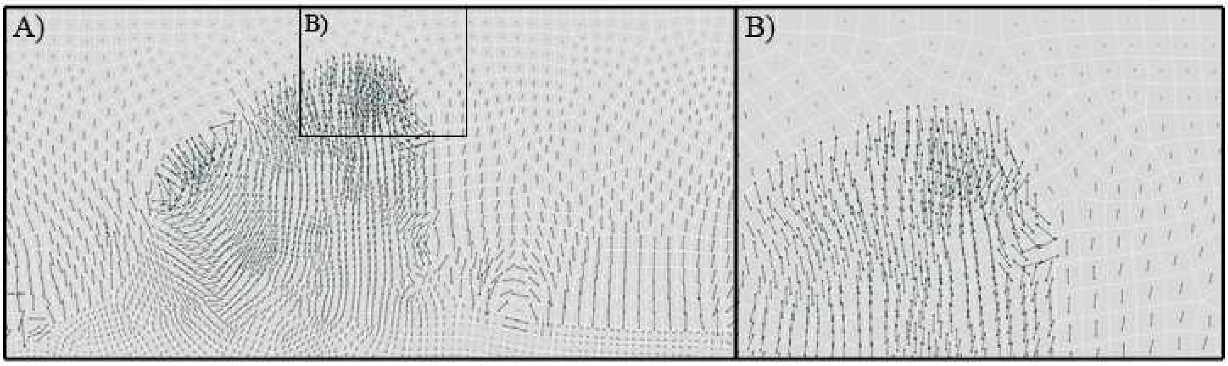

Figure 6.10

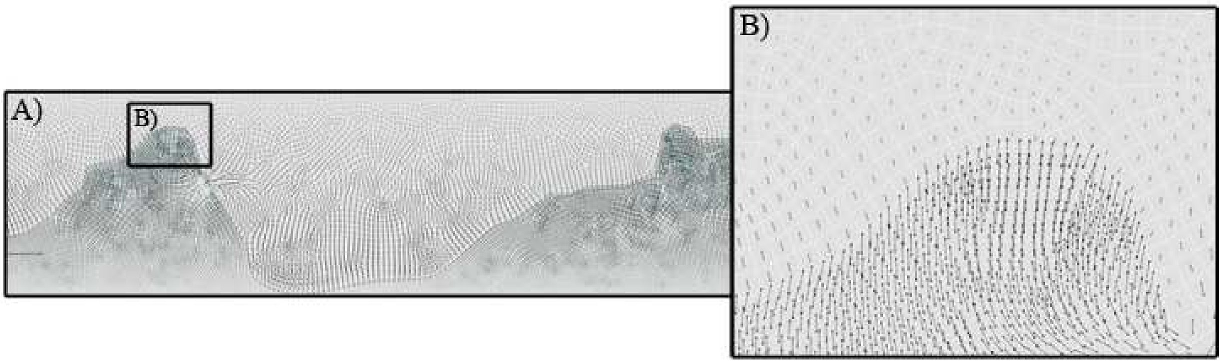

Figure 6.11

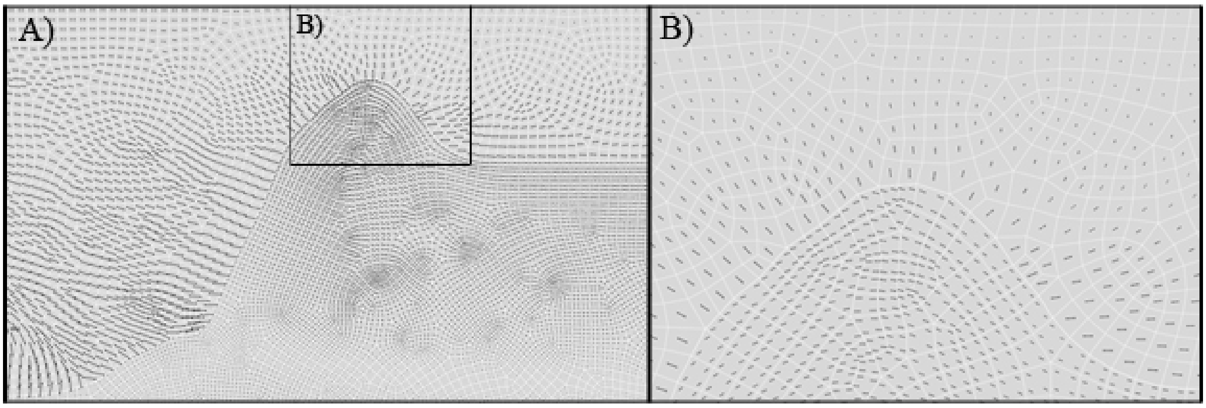

Figure 6.12

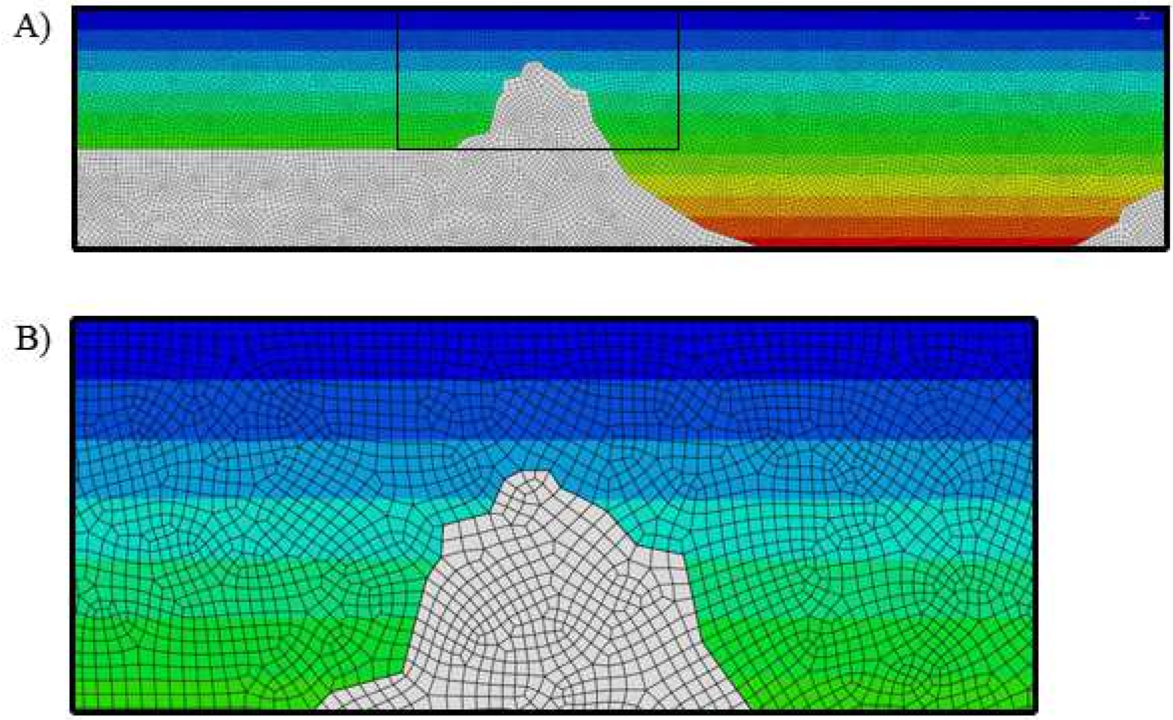

Figure 6.13

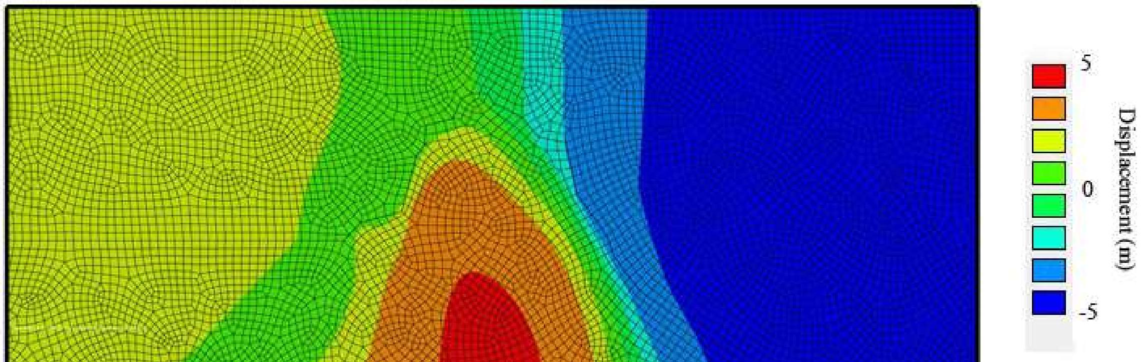

Figure 6.14

Figure 6.15

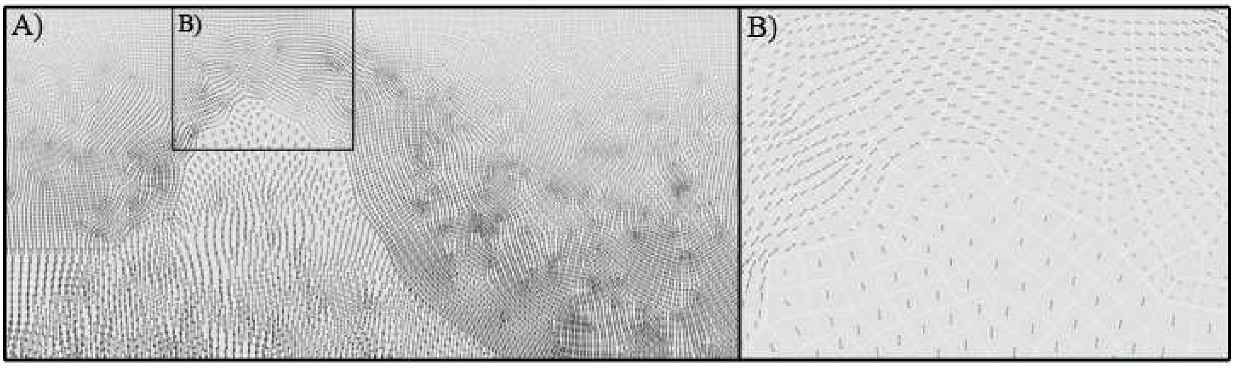

Figure 6.16

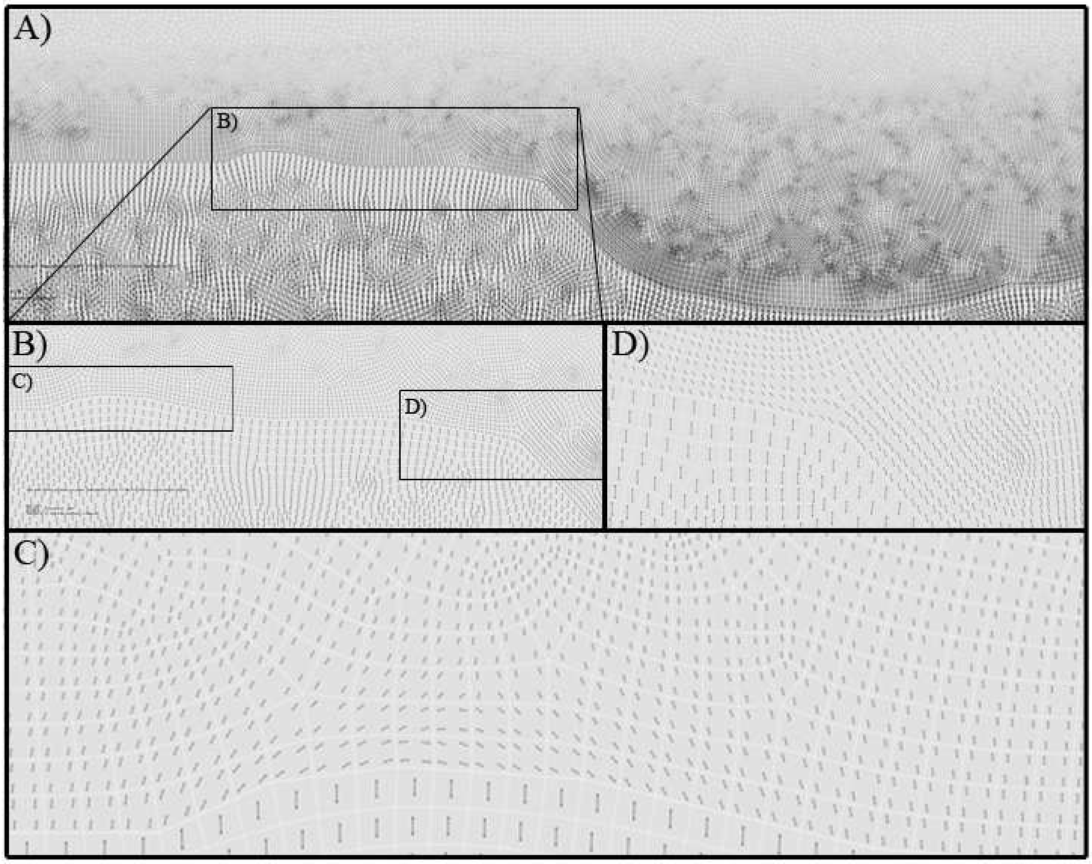

Figure 6.17

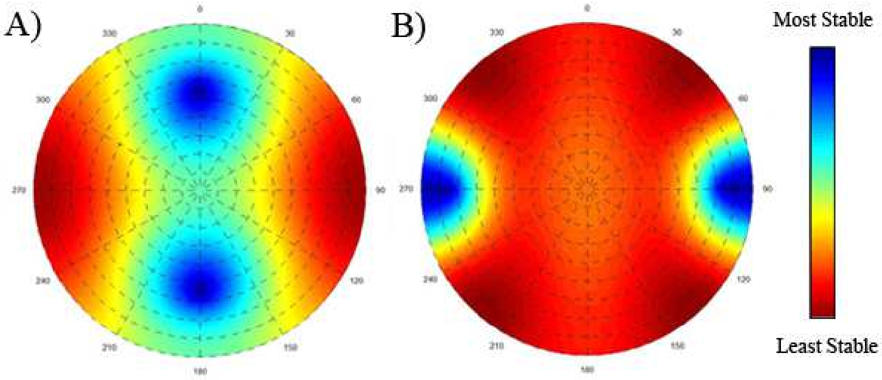

Figure 8.1

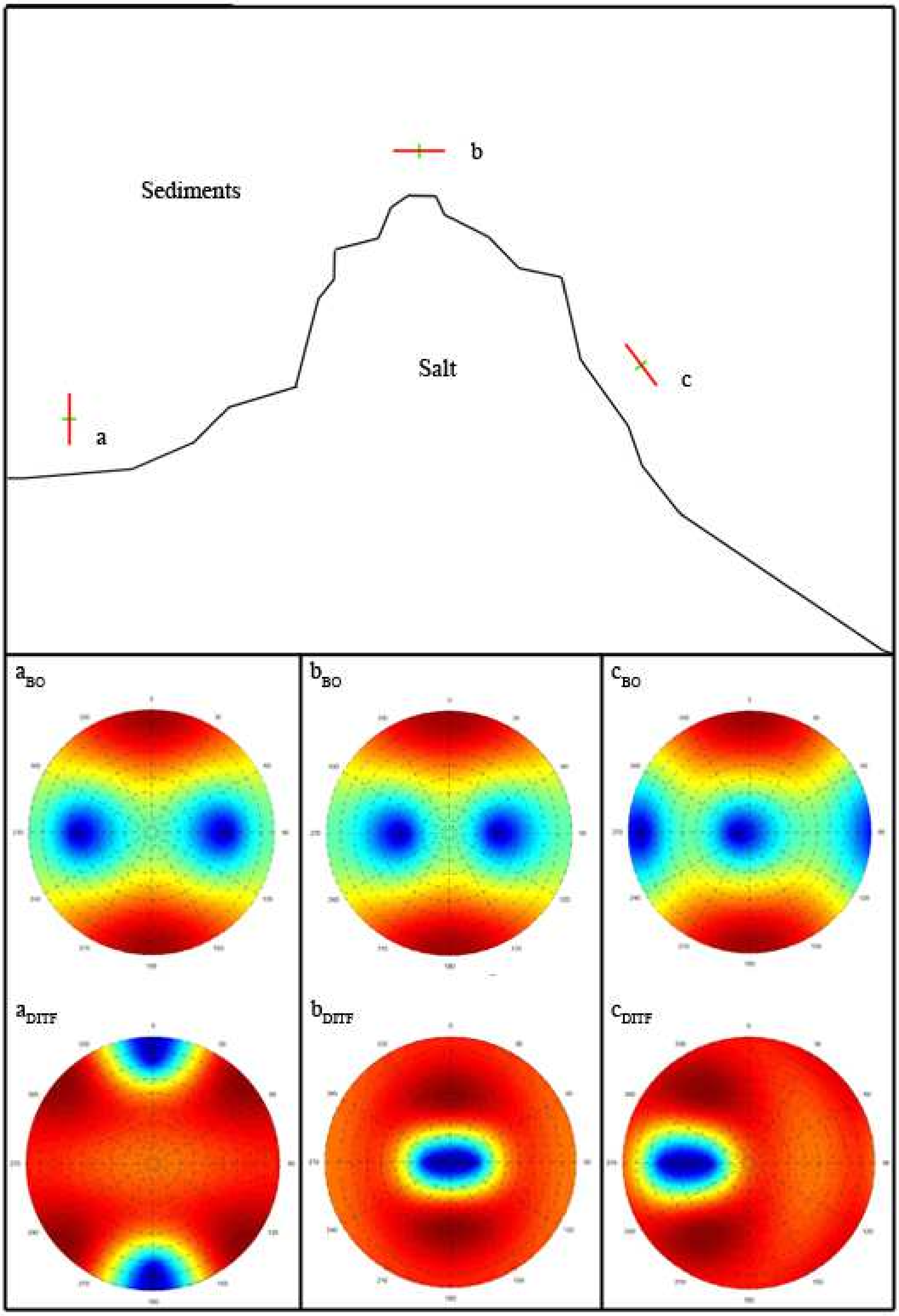

Figure 8.2

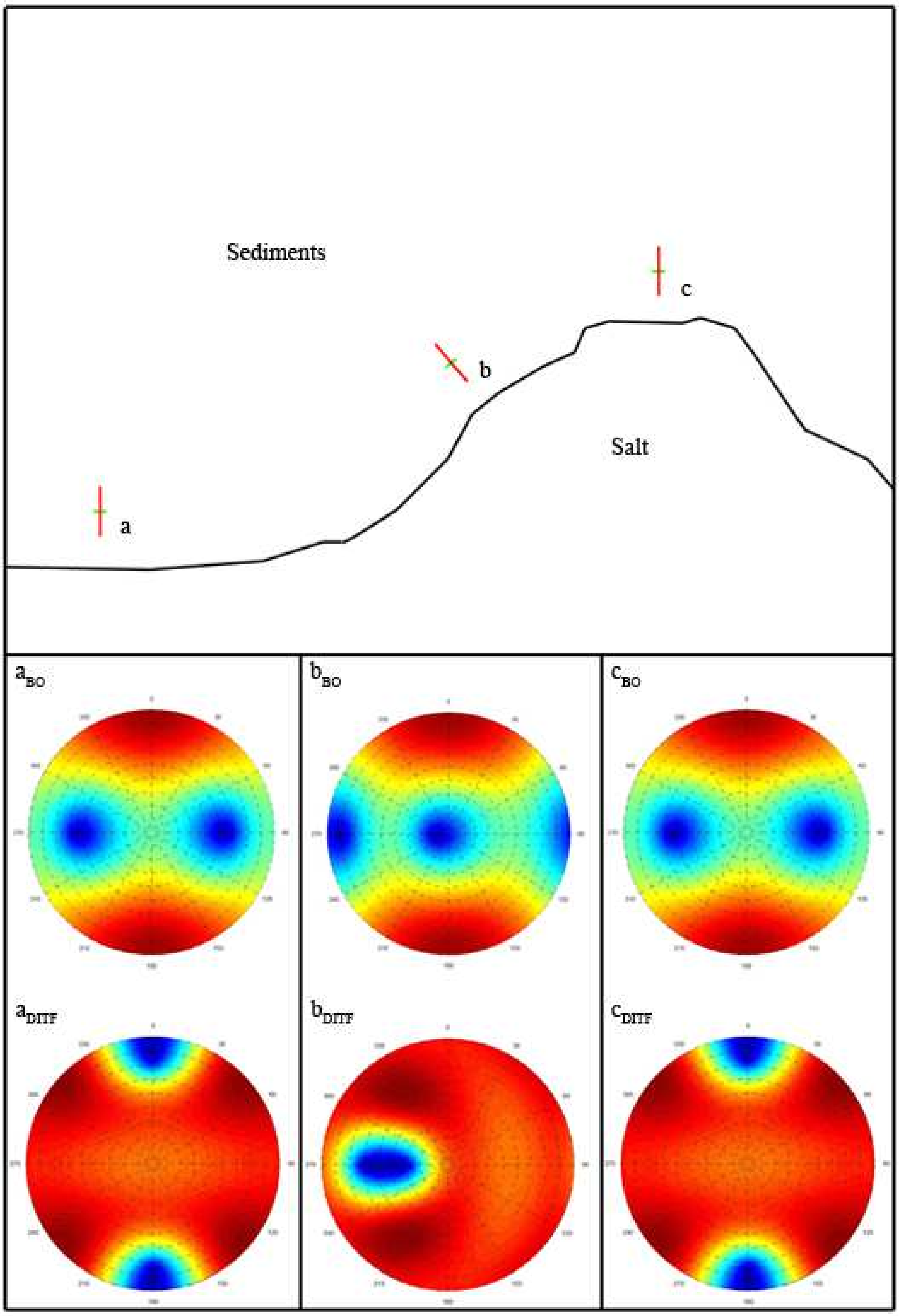

Figure 8.3